

Fabrication of Oriented Polycrystalline MOF Superstructures

Mercedes Linares-Moreau, Lea A. Brandner, Miriam de J. Velásquez-Hernández,
 Javier Fonseca, Youven Benseghir, Jia Min Chin, Daniel Maspoch, Christian Doonan,*
 and Paolo Falcaro*

The field of metal-organic frameworks (MOFs) has progressed beyond the design and exploration of powdery and single-crystalline materials. A current challenge is the fabrication of organized superstructures that can harness the directional properties of the individual constituent MOF crystals. To date, the progress in the fabrication methods of polycrystalline MOF superstructures has led to close-packed structures with defined crystalline orientation. By controlling the crystalline orientation, the MOF pore channels of the constituent crystals can be aligned along specific directions: these systems possess anisotropic properties including enhanced diffusion along specific directions, preferential orientation of guest species, and protection of functional guests. In this perspective, we discuss the current status of MOF research in the fabrication of oriented polycrystalline superstructures focusing on the specific crystalline directions of orientation. Three methods are examined in detail: the assembly from colloidal MOF solutions, the use of external fields for the alignment of MOF particles, and the heteroepitaxial ceramic-to-MOF growth. This perspective aims at promoting the progress of this field of research and inspiring the development of new protocols for the preparation of MOF systems with oriented pore channels, to enable advanced MOF-based devices with anisotropic properties.

ligands to inorganic metal nodes.^[1,2] According to the IUPAC definition of MOFs, the coordination network can be organized as a crystalline structure and can possess voids.^[3] This implies that MOFs can be amorphous and/or non-porous.^[4,5] However, the majority of MOFs reported in the literature are comprised of spatially ordered building blocks: this order underscores their crystalline structure.^[1,2,6,7] Such an ordered arrangement of building blocks in a crystalline lattice results in a geometrically organized network of pores (Figure 1).^[8,9] When the network of pores is connected and accessible, it allows for efficient diffusion of gas molecules. This property contributes to high surface area and pore volumes.^[10–12] Furthermore, the building block approach to their synthesis allows for MOFs to be prepared with tuneable pore metrics (e.g., accessible porosity, narrow pore distributions, and selected pore windows).^[1,6] The means to fine-tune the geometry, connectivity, pore volume, and chemistry of MOF pores has led to unprecedented performance for

gas storage, catalysis, and separation.^[13,14] The solvothermal method was preferentially chosen as a modular approach for the design of crystalline frameworks with customized functional properties, demonstrating their potential applications in

1. Introduction

Metal-organic frameworks (MOFs) are a subclass of coordination network materials prepared by connecting multtopic organic

M. Linares-Moreau, L. A. Brandner, M. de J. Velásquez-Hernández,
 P. Falcaro
 Institute of Physical and Theoretical Chemistry
 Graz University of Technology
 Graz 8010, Austria
 E-mail: paolo.falcaro@tugraz.at

J. Fonseca, D. Maspoch
 Catalan Institute of Nanoscience and Nanotechnology (ICN2)
 CSIC and The Barcelona Institute of Science and Technology
 Campus UAB, Bellaterra
 Barcelona 08193, Spain

 The ORCID identification number(s) for the author(s) of this article can be found under <https://doi.org/10.1002/adma.202309645>

© 2023 The Authors. Advanced Materials published by Wiley-VCH GmbH. This is an open access article under the terms of the Creative Commons Attribution License, which permits use, distribution and reproduction in any medium, provided the original work is properly cited.

DOI: 10.1002/adma.202309645

Y. Benseghir, J. M. Chin
 Faculty of Chemistry
 Institute of Functional Materials and Catalysis
 University of Vienna
 Währingerstr. 42, Vienna A-1090, Austria

D. Maspoch
 Departament de Química
 Facultat de Ciències
 Universitat Autònoma de Barcelona (UAB)
 Cerdanyola del Vallès, Barcelona 08193, Spain

D. Maspoch
 ICREA
 Pg. Lluís Companys 23, Barcelona 08010, Spain
 C. Doonan
 Department of Chemistry
 The University of Adelaide
 Adelaide, South Australia 5005, Australia
 E-mail: christian.doonan@adelaide.edu.au

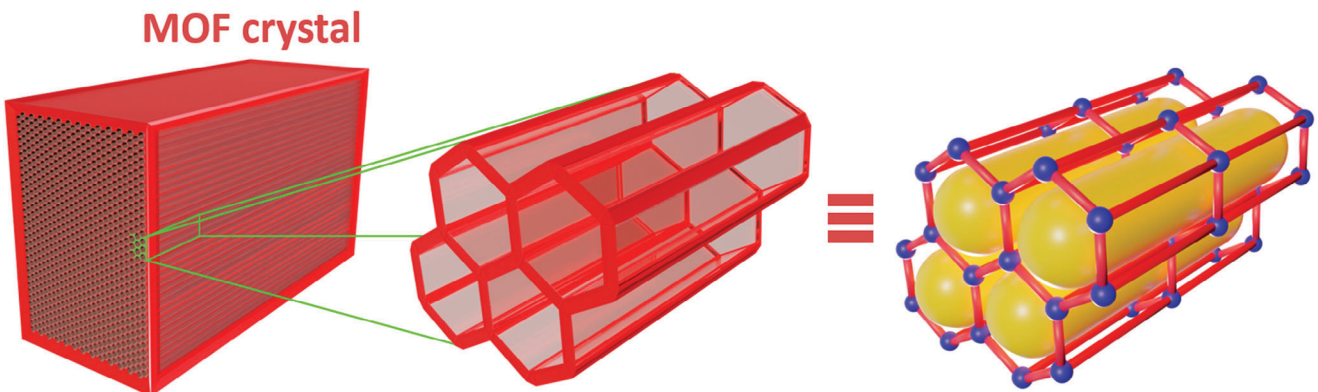


Figure 1. MOF Crystalline structure versus porosity. The pores are represented by yellow capsules.

sensing, microelectronics, optics, biomedicine, and biocatalysis.^[15,16] While solvothermal methods have led to the development of novel crystalline materials,^[6,7,17] this synthetic approach yields MOFs in a powdery form that is incompatible with the fabrication of many devices and can require a thick polymeric film to immobilize a limited amount of MOF material.^[15,18,19]

1.1. From Powders to the Spatial Positioning of Oriented Crystals

In general, breakthroughs in material technologies combine the design of materials with enhanced properties and the integration of their functionalities into spatially controlled architectures.^[20] The latter is relevant as spatial positioning protocols are essential for device fabrication.^[21–24] For crystalline functional materials, an additional control that has attracted long-term research interest is the alignment of the crystalline lattice over large domains to afford anisotropic properties;^[25] such an engineering of directional functional properties resulted in materials of interest for optics,^[26] sensing,^[27–29] microelectronics and charge transport,^[30–32] fluid and heat transport,^[33] energy production/storage,^[34–37] visualization technology, aerospace, soft robotics, and tissue engineering applications.^[25] We note that growing single crystalline structures, either as bulk materials or as films with controlled geometry (e.g., substrate attachment, patterning, controlled thickness) requires sophisticated equipment and processes.^[38–42] This limitation offers the opportunity to develop technologies for the alignment of polycrystalline materials.

These general considerations are also applicable to MOF materials^[43] and we envisage major technological progress of MOFs in real-world applications when the following two key aspects will be sufficiently advanced:

- 1) the precise positioning of MOF crystals in selected spatial locations (films and patterns). The development of such fabrication protocols is essential for their integration into multi-functional devices;
- 2) the control over the orientation of MOF crystals, and consequently pore alignment, in both MOF films and patterns (**Figure 2**). Such fabrication methods will enable the production of a new generation of MOF-based devices with anisotropic properties (Figure 2).

Of these two key aspects, the positioning of MOF crystals in selected locations is the most explored one. Indeed, a number of fabrication protocols have been studied in depth and, for a few of them, the developed know-how enabled the subsequent deposition of patterns of oriented MOF crystals. For example, the fabrication of patterns via conversion from Cu-based ceramics, later enabled the fabrication of highly oriented Cu-based MOF films and patterns.^[44,45] Cu(OH)₂, employed as the precursor crystalline material, possesses an inorganic lattice that matches the crystal lattice of selected MOFs. This matching and the dissolution of the inorganic precursors guide the oriented growth of the MOF crystals. This process, where different materials with matching crystal lattices are sequentially grown, is referred to as heteroepitaxial growth.^[46]

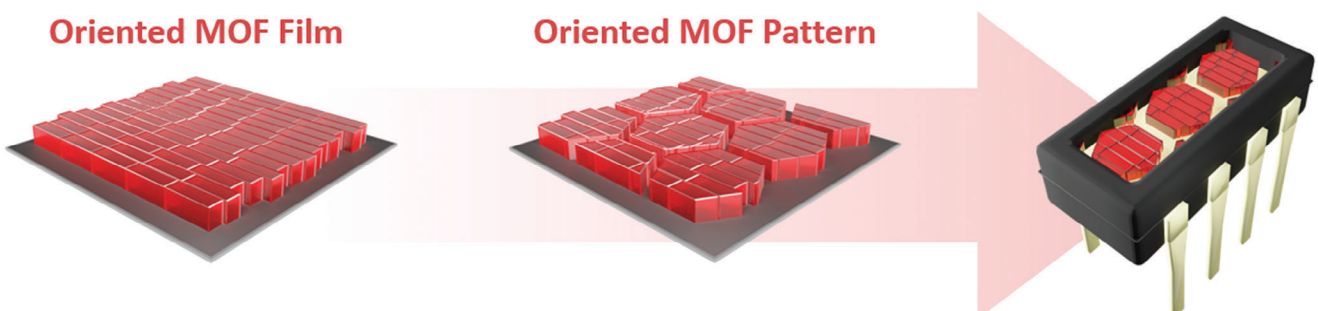


Figure 2. Oriented MOF films and patterns enabling the fabrication of MOF-based devices with anisotropic functional properties.

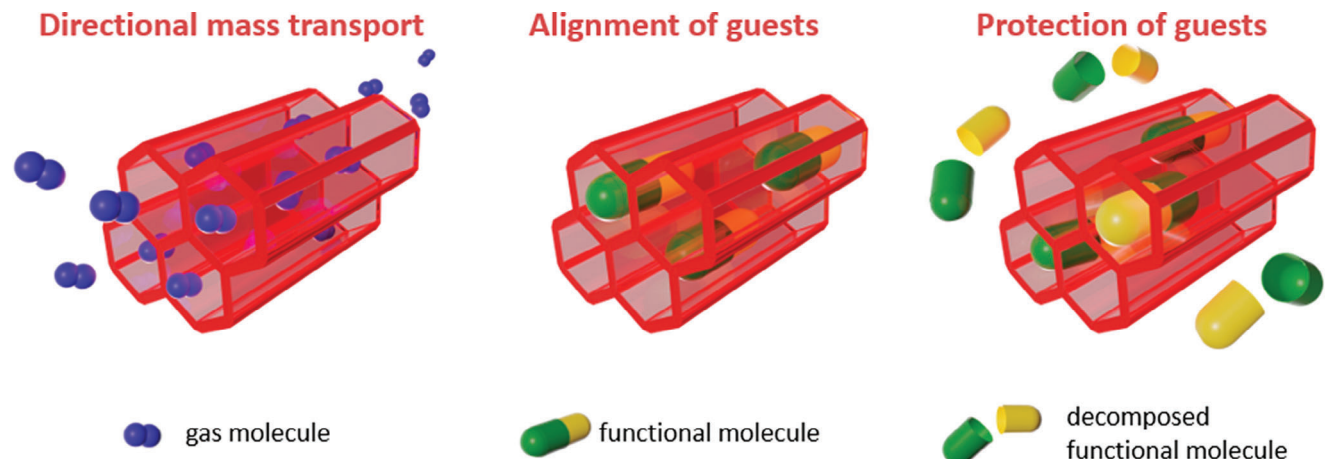


Figure 3. MOF crystal schematics displaying examples of functional properties at the nanoscale.

The focus of this perspective paper is to examine the current status of MOF research in the fabrication of superstructures with pores oriented along the plane of the substrate such as in-plane oriented (here termed IP-1D) and pores oriented simultaneously in-plane and out-of-plane (here termed as 3D-oriented MOF superstructures). The aim is to promote the progress of this field of research and to inspire the development of new protocols/tools for the preparation of MOF systems with oriented pore channels. MOF-based devices with precisely oriented pore channels will capitalize on anisotropic properties including enhanced diffusion along specific directions,^[47–52] preferential position/orientation of guest species (e.g., molecules),^[44,53–56] and protection of functional guests (e.g., dyes)^[54,57,58] (Figure 3).

These new directional properties in films and patterns could be harnessed for applications including microelectronics,^[59,60] separations, sensing, optics^[25,61–65] and thus expand the scope and applications of MOFs for advanced devices. To this end, this perspective will focus on the few approaches currently available for the fabrication of IP-1D and 3D-oriented MOF superstructures and will target specifically the crystalline orientation of these MOF systems. We note several reviews categorize polycrystalline MOF systems and describe the spatial arrangement of these MOF crystals into clusters by examining their configurations and morphologies.^[66–68] Here, we will examine those MOF superstructures with preferential crystalline orientation analyzing the key parameters that enable control over the orientation, and we will provide a personal view of the current limitations and potential of 3D-oriented MOF systems.

1.2. Types of Orientation in MOF Crystalline Superstructures

In this perspective we define the term *polycrystalline superstructures* as systems based on a collection of individual crystals. In “mesocrystals”, an abbreviation for mesoscopically structured crystals, which are ordered superstructures of crystals with mesoscopic size, the individual constituent crystalline units are typically named *primary particles* or *primary crystals*.^[69–72] The large majority of the reported MOF superstructures are formed by primary nanocrystals that lack preferential orientations: the ran-

dom orientations (0D-orientation, see Figure 4a) result in a system with isotropic macroscopic properties. Examples of 0D oriented MOF systems are typically produced by imprinting of powdery MOF particles on substrates (Figure 4b),^[18] ceramic-to-MOF conversion methods (Figure 4c),^[73] electrochemical synthesis (Figure 4d),^[74] and classical solvothermal crystallization of MOFs on substrates.^[75–77] If in a MOF superstructure, crystals are aligned along only one axis, the dominant orientational direction (1D-orientation, see Figure 4e) can enhance functional properties along this direction (uniaxial anisotropy). Examples in the literature report the fabrication of 1D-oriented MOF systems using different approaches including external shear forces on MOF crystals with anisotropic shapes (Figure 4f)^[64], the seeding MOF method on substrates (Figure 4g),^[78] and liquid-phase epitaxy depositions (e.g., Layer-by-Layer, see Figure 4h).^[79,80] It is worth noting that this 1D-orientation is typically perpendicular to the substrate used to support the MOF crystals^[81]; this *out-of-plane* (OOP) orientation can be examined with out-of-plane X-ray diffraction setups (vide infra). However, when the 1D-orientation occurs along the plane of the substrate, the MOF polycrystalline system possesses an in-plane (IP) orientation: this type of orientation is less common for the current MOF deposition protocols.

A higher degree of crystalline orientation of MOF superstructures requires two dominant crystalline directions of the primary anisotropic MOF crystals (2D-orientation); however, when two crystalline orientations are shared by the MOF particles of the same superstructure, the result is the iso-orientation of the third crystallographic direction (3D-oriented MOF systems). Under these conditions, a 2D-oriented MOF superstructure is equivalent to a 3D-oriented MOF system (3D-orientation). In this perspective, we will refer to 3D-oriented MOF superstructures to describe systems with primary crystals preferentially oriented along the x, y, and z axes (Figure 4i). Examples of 3D-oriented MOF superstructures are those prepared by the use of external forces (Figure 4j),^[82] colloidal assembly (Figure 4k),^[83] and heteroepitaxial growth from oriented ceramic precursor films and patterns (Figure 4l).^[44] For systems with 3D-oriented domains, both OOP and IP alignments should be observed by using dedicated X-ray diffraction setups. However, to assess the quality of the

Types of order in MOF superstructures

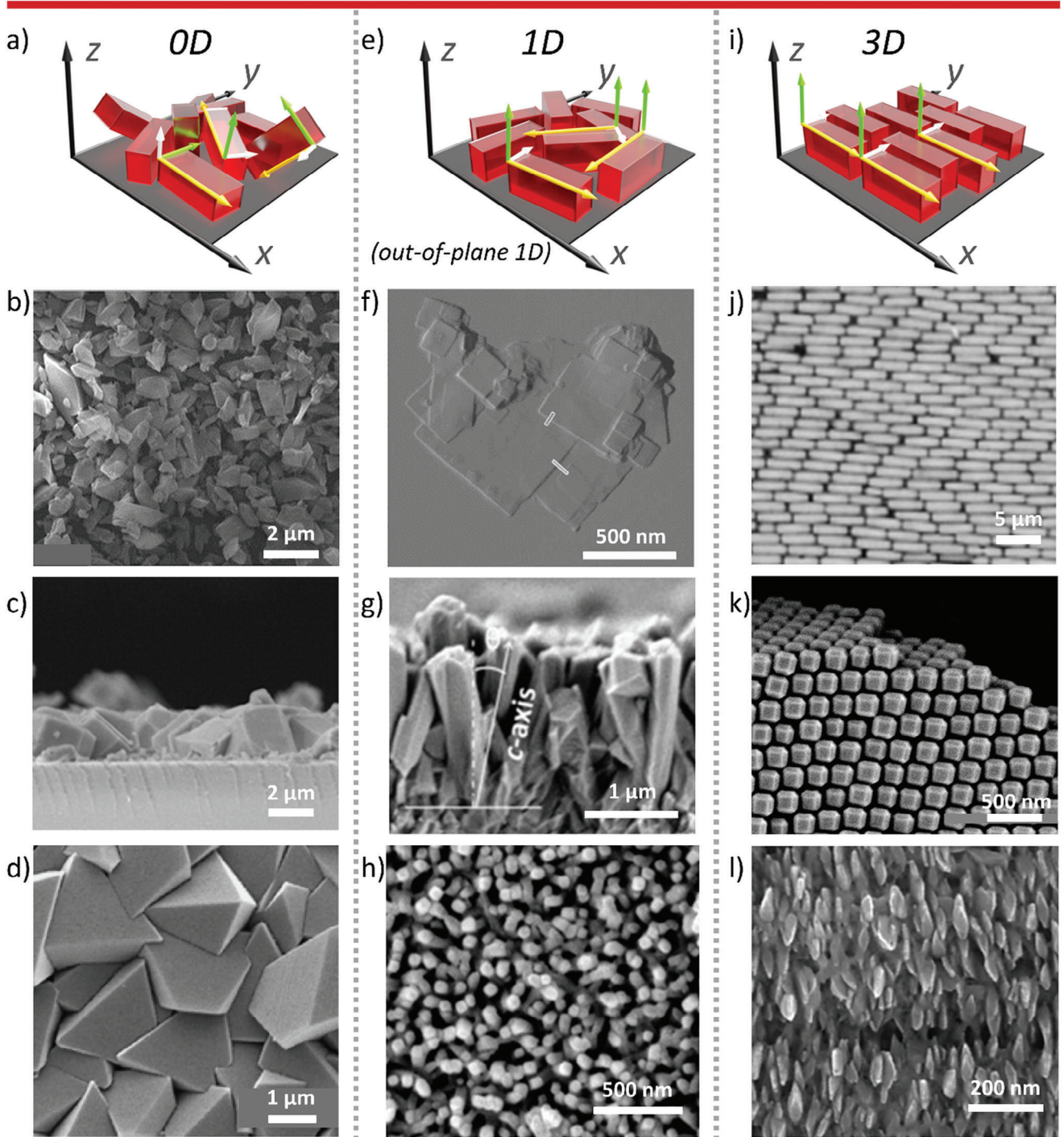


Figure 4. Types of order ((a) random, 0D; (e) out-of-plane, OOP-1D; and (i) out-of-plane and in-plane, 3D) in MOF polycrystalline systems with exemplary micrographs by Scanning Electron Microscopy (b-d), (g-h), and (k,l), Atomic Force Microscopy (f) and Confocal Laser Scanning Microscopy (CLSM) (j). An alternative 1D-ordered configuration to OOP-1D order is IP-1D order. Video S1 (Supporting Information) illustrates all these configurations. Image (b) adapted with permission.^[18] Copyright 2013, John Wiley and Sons. Image (c) adapted with permission.^[73] Copyright 2013, Elsevier B.V. Image (d) adapted with permission.^[74] Copyright 2009, American Chemical Society. Image (f) adapted with permission.^[64] Copyright 2014, Springer Nature. Image (g) adapted with permission.^[78] Copyright 2010, John Wiley and Sons. Image (h) reproduced under terms of the CC-BY 4.0 license.^[79] Copyright 2020, The Authors, published by John Wiley and Sons. Image (j) reproduced under terms of the CC-BY 4.0 license.^[82] Copyright 2022, The Authors, published by Elsevier B.V. Image (k) adapted with permission.^[83] Copyright 2018, Springer Nature. Image (l) adapted with permission.^[44] Copyright 2017, Springer Nature.

iso-orientation of the primary crystalline particles, texture analyses are required.

1.3. Analysis Techniques Used for the Identification of the Crystalline Orientation

To examine the ordered polycrystalline superstructures, two main analyses are widely used: microscopy and X-ray analysis.

Micrographs, typically collected by scanning electron microscopy (SEM) or atomic force microscopy (AFM), allow the morphology of the polycrystalline MOF to be identified. SEM imaging typically relies on the secondary electrons (SE) emitted by the atoms of a material after inelastic interactions with a primary electron beam. These SEs originate at the surface or subsurface regions of the sample and are used to reconstruct the morphology of the surface of the sample. In the case of AFM, tapping mode is the most frequently used. In this mode, a sub-micron sized silicon probe oscillates near the surface of the sample. Changes in the amplitude and phase of the oscillation which arise from tip-sample interactions (e.g., van der Waals, electromagnetic forces or others) can be used to reconstruct the topography of the sample surface.^[84] In the case of fluorescent MOFs or guest@MOF particles, Confocal Laser Scanning Microscopy (CLSM) is also widely used for the visualization of micrometric crystals.^[85,86] Typically, all these measurements provide local information on the morphology of the polycrystalline systems. The maximum size of the investigated areas can be limited by the resolution of the individual particles. For the typical particle sizes involved (ranging from hundreds of nanometers to microns), a single micrograph could show a few hundred square microns. If it is possible to distinguish the morphology of the principal crystalline particles, then a visual inspection of the micrographs helps with the identification of domains in which crystals are oriented in a 0D-, 1D- or 3D- fashion (Figure 4) from the collected images. Different image analysis tools are also available to assess the local degree of orientation of the crystalline particles from this local morphological information (e.g., Fourier component analysis using digital image processing software).^[82]

Transmission electron microscopy (TEM) is another widely used microscopy technique that relies on the interactions of an electron beam transmitted through the sample, typically prepared as ultrathin sections.^[84] TEM is a cornerstone method for textural analyses of inorganic materials (e.g., metals and ceramics).^[87–90] However, in 3D-oriented MOF systems, the limited utilization of TEM for textural analyses can be attributed to the intrinsic sensitivity of MOFs to radiation-induced damage^[91] and the cumbersome sample preparation demanding thin sections.^[92] Nonetheless, with the ongoing advancements in microscopy techniques (e.g., the development of low-dose analyses or the use of cryostatic methods),^[93] we anticipate a growing significance of TEM in this field. Currently, TEM provides localized insights, highlighting features such as local phase transitions,^[94,95] crystal boundaries, defect sites (e.g., dislocations), pore orientation, and host-guest interactions.^[91,93,96,97]

X-ray investigations are based on the collection of X-rays diffracted by the sample. The investigated area depends on the cross-section of the X-ray beam with the sample and can vary from tens of square microns (e.g., synchrotron facilities)^[98] to

square centimeters (e.g., laboratory diffractometer).^[99] The latter is the most common setting and, under these conditions, it is possible to analyze a larger population of crystals. The out-of-plane X-ray setup provides information on crystalline planes either parallel, or with a parallel component, to the substrate. Typical configurations are those where the X-ray detector moves along the plane in which the incident and reflected X-ray beams lie (Figure 5a). Different measurement geometries are available; however, most diffractometers use Bragg-Brentano geometry for out-of-plane measurements. In this configuration, the incident angle (θ) between the X-ray source and the sample is maintained at 1/2 of the detector angle 2θ . Either the detector angle or both incident X-ray and detector angles are varied such that constructive interference is obtained when the path difference is an integer multiple of the X-ray wavelength (Bragg's law).^[100,101] In this way, the diffraction produced by crystallographic planes parallel to the substrate, or with a parallel component, results in a diffraction pattern. This means that this setup is sensitive to the OOP orientation of the crystals. When comparing this plot with the one collected on a random powdery system, the differences (positions of the peaks and relative intensities) indicate a preferential orientation of the system with one crystallographic direction perpendicular to the substrate (Figure 5a).

The evaluation of IP orientation requires an in-plane X-ray diffraction measurement setup (Figure 5b). This diffraction configuration provides information on crystalline planes perpendicular, or with a perpendicular component, to the substrate. In a typical configuration, the X-ray detector moves parallel to the substrate. The Bragg-Brentano geometry can also be applied in this case, with both the detector and source (incident beam) moving within the plane parallel to the substrate. In MOF polycrystalline systems, the detection of an IP orientation indicates the presence of some crystals with one or more crystallographic directions aligned parallel to the substrate.

A comparison between the relative intensities of the reflections observed in OOP and IP measurements can provide a qualitative assessment of the preferred orientation of a polycrystalline sample. However, for a full and quantitative characterization of the orientational distribution of the crystal population with respect to a specific direction, texture analysis is required.^[101] This analysis is obtained by mapping the intensity of a specific reflection, or more than one, as the sample is rotated. In this configuration, the source and detector are typically kept at fixed θ – 2θ angles for a specific crystallographic reflection within a plane parallel to the substrate. The sample is rotated about the axis perpendicular to the substrate (azimuthal scan, see Figure 5b) and the intensity is recorded. For a highly textured polycrystalline system (i.e., 3D-oriented polycrystalline MOF superstructures behaving similarly to a monocrystalline-like system), for a given reflection, high-intensity maxima can be found at specific rotation angles. The number and position of the maxima depend on the unit cell symmetry. The narrower the full width at half maximum (FWHM) and the more intense the maximum is, the more aligned the crystals are. For a disordered polycrystalline system (0D-oriented), the intensity of the X-ray will be constant for all the scanned angles. Typical texture analyses are conducted by collecting pole figures and azimuthal scans. For additional information on the mentioned X-ray setups and measurements, we invite the

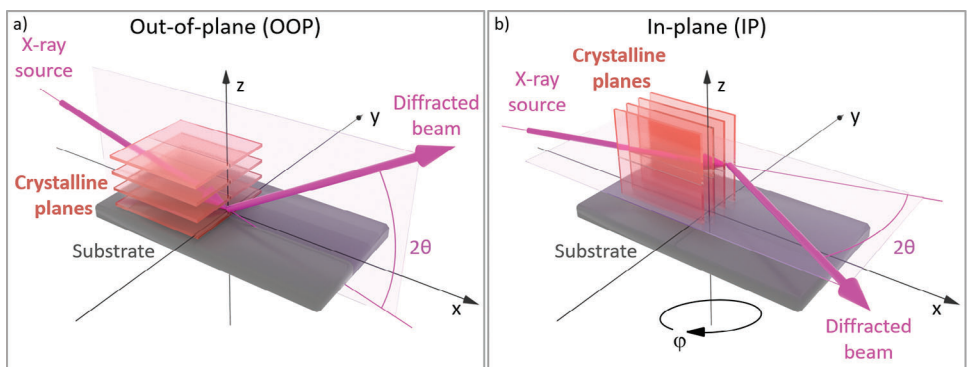


Figure 5. Schematic showing the measurement configuration for out-of-plane (OOP) (a), in-plane (IP), and azimuthal investigations (φ -rotation) (b).

reader to consult articles and books dedicated to X-ray diffraction of thin films.^[101,99,102,103]

1.4. From Random to In-Plane Orientation

Pioneering methods in MOF positioning employed solvothermal growth, heterogeneous nucleation, interfacial syntheses, and ceramic-to-MOF conversion for the preparation of 0D-oriented MOF films and patterns.^[18,68,73,104,105] Subsequently, more sophisticated approaches have been developed for controlled growth and to improve the overall order in MOF superstructures. Predominantly, these methods afford a crystalline orientation perpendicular to the surface of the substrate (z-direction) used to support the polycrystalline system (Figure 3e). The structure-property relationship can be confirmed by observing specific directional properties along the z-directions (OOP orientation). For example, by matching the orientation of squared-like Cu₂(BDC)₂ crystals with the direction of the pore channel, MOF-based membranes with enhanced mass transfer along the z-direction have been prepared by Gascon and co-workers.^[64] Such a 1D-oriented MOF superstructure was used to enhance the mass transfer of CO₂ while acting as an effective molecular separator for a CO₂/CH₄ mixture.^[64] For the fabrication of this Cu₂(BDC)₂-based membrane, shearing forces applied to a colloidal polymeric solution of MOF crystals with an anisotropic shape (i.e. nanosheet with cuboid morphology) resulted in a preferential orientation of the nanosheet within the polymeric matrix. This methodology is known to align different nanostructured materials with anisotropic shapes (nanotubes,^[106] nanowires,^[107] nanosheets,^[108] etc.).

Occasionally, 1D-oriented MOFs have been prepared with gel-layer growth,^[109,110] electrochemical^[111] and vapor phase deposition methods.^[112,113] These methods usually afford OOP orientation in MOF films. Furthermore, MOF patterns prepared via evaporation often result in the crystallization of MOF particles with OOP orientation.^[114] As the focus of this perspective is the development of 3D-oriented MOFs, we will mainly describe the most used fabrication methods that have a high potential to maximize anisotropic functions in polycrystalline MOF superstructures. Specifically, the seeding and layer-by-layer (LbL) methods are dominant approaches for the fabrication of high-quality MOF membranes with preferential OOP orientation. Below we briefly

summarize some of the results achieved in the orientation of MOF crystals; however, for an in-depth discussion about these methods, we point the readers to other comprehensive and authoritative reviews on the topic.^[115–117]

The seeding method is a two-step approach: the deposition of pre-synthesized particles as crystalline seeds and the secondary crystal growth that will result in a preferential crystalline orientation.^[78,118] This deposition method has been used for decades in zeolite technology to prepare oriented porous membranes.^[115] A typical deposition results in a homogeneous spatial distribution of crystalline seeds on a substrate (e.g., glass, alumina); the seeds could be deposited with a dominant crystallographic orientation perpendicular to the support^[119] or could be randomly oriented.^[78,118] The deposition of these crystalline seeds is followed by exposure to a crystal precursor mixture: this process promotes crystal growth (secondary growth) preferentially on the seeds. When examining the secondary growth step, an “evolutionary selection” mechanism relates the crystalline orientation to the probability of survival of the growing particles given by the direction of fastest growth.^[118,120] In this process, crystals are overgrown by other adjacent crystals, limiting the growth in the direction parallel to the substrate. In the case of a film, only those crystals with their fastest growth direction perpendicular to the substrate surface will survive, growing on top of neighbour particles with different orientations (i.e., slower-growth speed).^[118] Upon film thickening, only a few favoured crystalline orientations survive. Thus, the growth during the last stage results in a partially oriented structure. This seeding approach was effectively applied to MOFs: crystalline seeds with desired chemical composition, topology and pore properties are pre-synthesized and then deposited on supports by different techniques (e.g., by means of electrostatic interactions, covalent chemical anchoring, or capillary forces during dip- or spin-coating).^[78,119,121,122] This method can produce continuous, well-intergrown MOF membranes with OOP orientation of the pore channels. When compared with a membrane of randomly oriented MOF crystals, OOP 1D-oriented membranes show superior selectivity, a crucial property for separation applications.^[123] For example, Caro and co-workers produced OOP-1D oriented ZIF-7 membranes on alumina supports.^[78] The same approach has been extended to the preparation of several MOF membranes based on ZIF-8,^[121] ZIF-67,^[124] ZIF-69,^[125] ZIF-L,^[126] NH₂-MIL-125(Ti),^[127] Ni(HBTC)(bipy),^[128] and UiO66.^[129]

The Layer-by-Layer (LbL) approach, first reported in 2007, afforded the deposition of pinhole-free MOF films with comparatively low roughness, low defect density, and with preferential OOP orientation.^[81,116,130] In a typical LbL deposition, a substrate is chemically functionalized with a self-assembled monolayer (SAM) that exposes specific functional group termination (e.g., -COOH, -OH or pyridyl groups) to the solution. The SAM is used to improve the chemical compatibility of the support and promote the anchoring of the inorganic MOF building units. Then the substrate is sequentially exposed to the different MOF building blocks: during these repetitive cycles, the reaction occurs predominantly at the interface of the SAM and then at the surface of the MOF polycrystalline film crystals, which is grown one layer at a time.^[81] By selecting the number of cycles, this deposition method affords exquisite control over the film thickness, from a few nm up to micrometers.^[80,116] LbL deposition is typically performed at moderate or room temperatures.^[116] For example, in 2007, Wöll, Fischer and co-workers demonstrated for the first time the step-by-step synthesis of HKUST-1 films by the LbL method on SAM-functionalized Au substrates.^[81] Homogeneous HKUST-1 thin films with high crystallinity and OOP orientation were obtained. The same method was later used to grow MOF-508 ($\text{Zn}(\text{BDC})\text{-}(4,4'\text{-bipyridine})_{0.5}$) as a single lattice without interpenetration which is typically found during solvothermal synthesis of this MOF.^[131] Interestingly, the use of an appropriately functionalized substrate breaks the bulk MOF's symmetry, and thus the formation of interpenetrated networks is suppressed.^[131] This method for the fabrication of surface-mounted MOF (SURMOFs) is a powerful tool to control the chemistry of the MOF film and to synthesize MOF structures that are not typically accessible by conventional solvothermal methods.^[132]

When referring to a possible 3D crystal orientation of MOF films, this was defined as hypothetically possible with the Langmuir-Blodgett deposition method (air-liquid interface self-assembly).^[133,134] Indeed, IP orientation has been observed first by using synchrotron facilities and then by using laboratory X-ray diffractometers.^[60,134,135] The simultaneous IP and OOP orientations have become progressively more common in LbL deposition obtained on functionalized substrates through different fabrication methods (e.g., LbL-Liquid Phase Epitaxy (LPE),^[136] combinations of Langmuir-Blodgett and LbL,^[133] continuous flow dynamic LbL,^[137] spray and spin-coating depositions).^[80,138] Textural analyses have confirmed, in a few cases, the existence of oriented polycrystalline systems.^[134,139] However, with the exception of rare cases, the general lack of textural analyses or morphological evidence of extended 3D domains does not allow a detailed discussion about the 3D-order in these systems. Another important aspect is the mechanism of formation that has been disclosed for the OOP order^[140]; however, for the IP orientation, a mechanism is yet to be revealed. Overall, these studies on 1D-towards 3D-oriented SURMOF systems demonstrate that the progress in MOF film fabrication is crucial to advance the control over crystalline orientation. Further progress is expected to demonstrate the full potential of LbL deposition methods. For a more detailed comprehension of the literature on MOF films with OOP and IP orientation, we suggest consulting review papers of renowned groups for their substantial contribution to the field.^[116,117,135,141–143]

1.5. Recent Methods to Prepare 3D-Oriented Superstructures

In recent years, a few different methods have afforded the fabrication of extended domains of MOF crystals with 3D-orientation (Figure 6). The first strategy we will discuss is based on the control over the assembly of pre-formed particles (see Figure 6a and Video S2, Supporting Information). This wet method can efficiently stack pre-synthesized MOF crystals into ordered superstructures by controlling their attractive and repulsive interactions.^[66,144] The second method we will examine uses external forces (e.g., external electromagnetic field) to align pre-formed anisotropic MOF crystals suspended in a solvent (see Figure 6b and Video S3, Supporting Information).^[82,86,145] The third and last approach we will describe is a specific ceramic-to-MOF conversion; via heteroepitaxial growth, this wet approach enables the fabrication of 3D-oriented MOF crystals in the centimeter range (see Figure 6c and Video S4, Supporting Information). At the moment, these methods are in their infancy and we posit that further progress is needed to unlock their full potential. Other emerging methods will be discussed in the final section.

2. Oriented polycrystalline MOF superstructures by assembly processes

2.1. Introduction

The assembly of colloidal MOF particles enables the fabrication of extensive domains of MOF superstructures with 1D or 3D orientation.^[83,146] This method is based on the spontaneous organization of colloidal MOF particles into ordered superstructures, mirroring the natural phenomenon of atoms forming molecules. To explore assembled MOF superstructures, it is essential to first understand the fundamental requirements that underlie the assembly of MOF particles.^[66] Firstly, the preparation of monodisperse colloidal MOF particles stands as a pivotal prerequisite for their subsequent assembly in an ordered fashion. Achieving such control over MOF size and shape monodispersity requires a delicate balance of synthetic parameters, including precursors, modulators, reaction time and temperature, among others.^[147] The colloidal stability of MOF particles is another aspect that significantly affects their assembly into ordered superstructures. Colloidal stability is often compromised by attractive forces such as van der Waals interactions, leading to particle flocculation.^[148,149] Steric and electrostatic stabilization strategies have been reported to enhance the colloidal stability of MOF particles. These strategies involve tethering molecular chains to the MOF surface to establish a steric barrier or manipulating the charge of the MOF surface through electrostatic interactions.^[150–152] Finally, it should be noted that the interaction of various forces ultimately governs the final arrangement of MOF particles during their assembly. In brief, assembly is a thermodynamic process,^[153] in which colloidal MOF particles aggregate in equilibrium states (minima of Gibbs or Helmholtz free energies). The equilibrium states are obtained by the balance of attractive (e.g., van der Waals, depletion, hydrogen bond, $\pi-\pi$ stacking, etc.) and repulsive (e.g., electric double-layer, electrostatic repulsion, etc.) forces. In this section, we explore the diverse approaches (solvent evaporation-based assembly, depletion-assisted assembly, air-liquid interface assembly, DNA-assisted assembly, anisotropic pattern-assisted

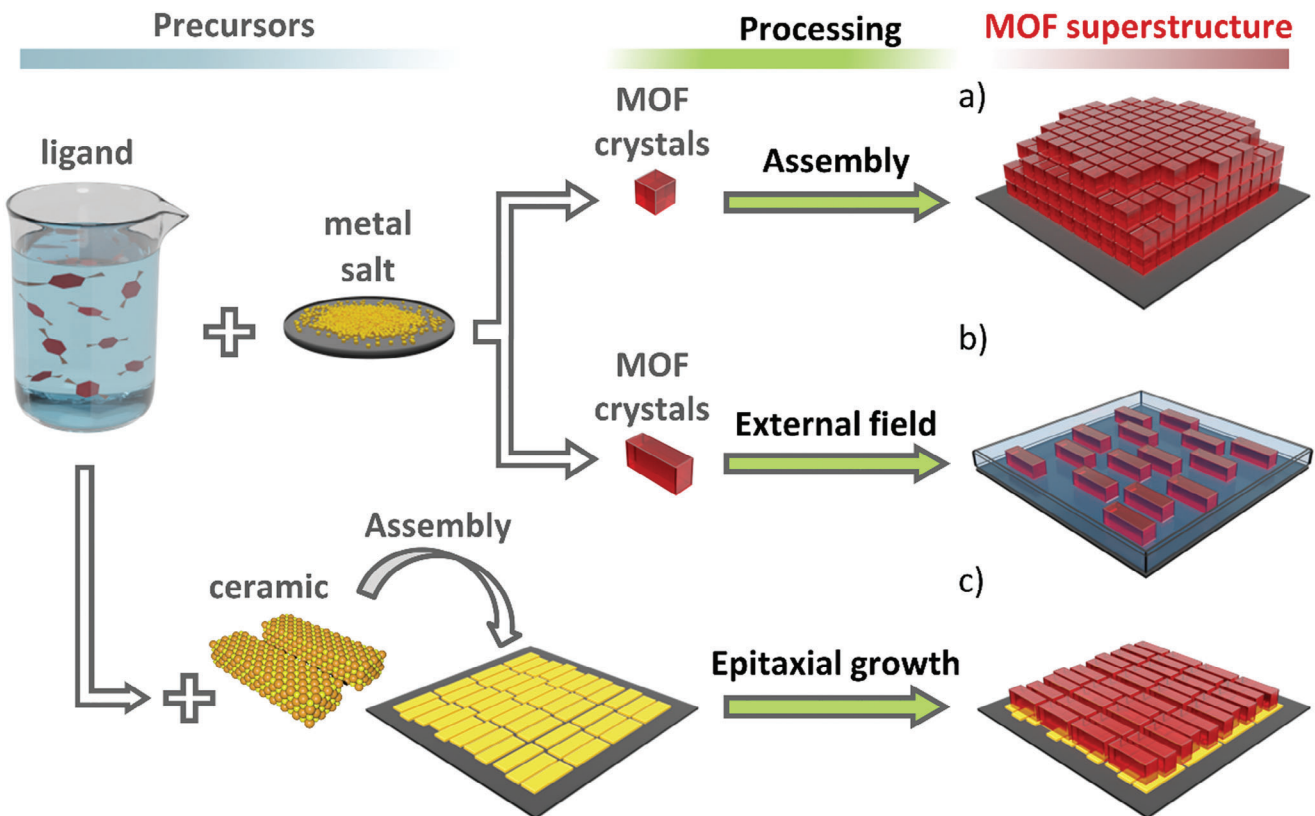


Figure 6. Main different approaches used to obtain aligned MOF polycrystalline superstructures with 3D-orientation.

assembly, and ice-templated assembly) that have been developed to date for the assembly of MOF particles into 1D- and 3D-oriented MOF superstructures.^[154,155] The orientation of the MOF particles in the superstructures with respect to the OOP direction is elucidated; however, we note that – to date – the limited size of the aligned domains did not allow for textural analyses with laboratory X-ray diffractometers. In the protocols summarized below, we focus on the assembly of the MOF particles into oriented superstructures while the synthesis of the specific MOF particles can be found in the original papers.

2.2. Solvent Evaporation-Based Assembly

In the early stages, the assembly of MOF particles into superstructures focused on regulating the evaporation of their colloidal solutions (Figure 7a). As the solvent evaporation process works against entropy, MOF particles tend to adopt an ordered phase to optimize entropy and consequently minimize free energy. Through this method, both the Eddaoudi group and the Granick group were pioneers in the assembly of MOF particles with a 3D orientation, forming two-dimensional layers.^[156,157] Specifically, through the solvent evaporation approach, Eddaoudi and co-workers accomplished the assembly of cubic, edge- and corner-rounded cubic, and (110)-truncated cubic *In-soc*-MOF particles, as well as cubic *Ga-soc*-MOF particles, resulting in 3D-oriented two-dimensional films. Cubic and corner-rounded cubic particles assembled in simple cubic lattices, while (110)-truncated cu-

bic particles could arrange in both hexagonal close-packed (*hcp*) and square close-packed (*scp*) assemblies (Figure 7b-d).^[156] Similarly, Granick and co-workers reported the assembly of rhombic dodecahedral ZIF-8 (RD-ZIF-8) particles into two-dimensional hexagonal lattices. This assembly was achieved by the gradual evaporation of the colloidal solvent N,N-dimethylformamide (DMF) over a silicon wafer. Drying 1 wt% dispersions resulted in 3D-oriented two-dimensional hexagonal lattices, where the crystals were aligned in the ⟨111⟩ direction. However, drying 0.05 wt% dispersions led to 1D-oriented two-dimensional loose hexagonal lattices with the RD-ZIF-8 particles aligned in the ⟨110⟩ direction.^[157] Remarkably, the first three-dimensional MOF-based superstructures were also realized through the process of solvent evaporation.^[146] In particular, PVP-modified octahedral UiO-66 (O-Uio-66) particles dispersed in water slowly settled due to gravity within a glass capillary, and the subsequent drying of the solvent led to the arrangement of MOF particles, forming ⟨111⟩-oriented hexagonal layers that stacked to create three-dimensional superstructures with 3D orientation.^[146]

2.3. Depletion-Assisted Assembly

The assembly process through solvent evaporation can be further controlled by introducing depletants (such as small nanoparticles, micelles, polymers, salts, etc.) along with the colloidal particles, resulting in a method referred to as depletion-assisted assembly (Figure 7e).^[158] This approach harnesses the short-range

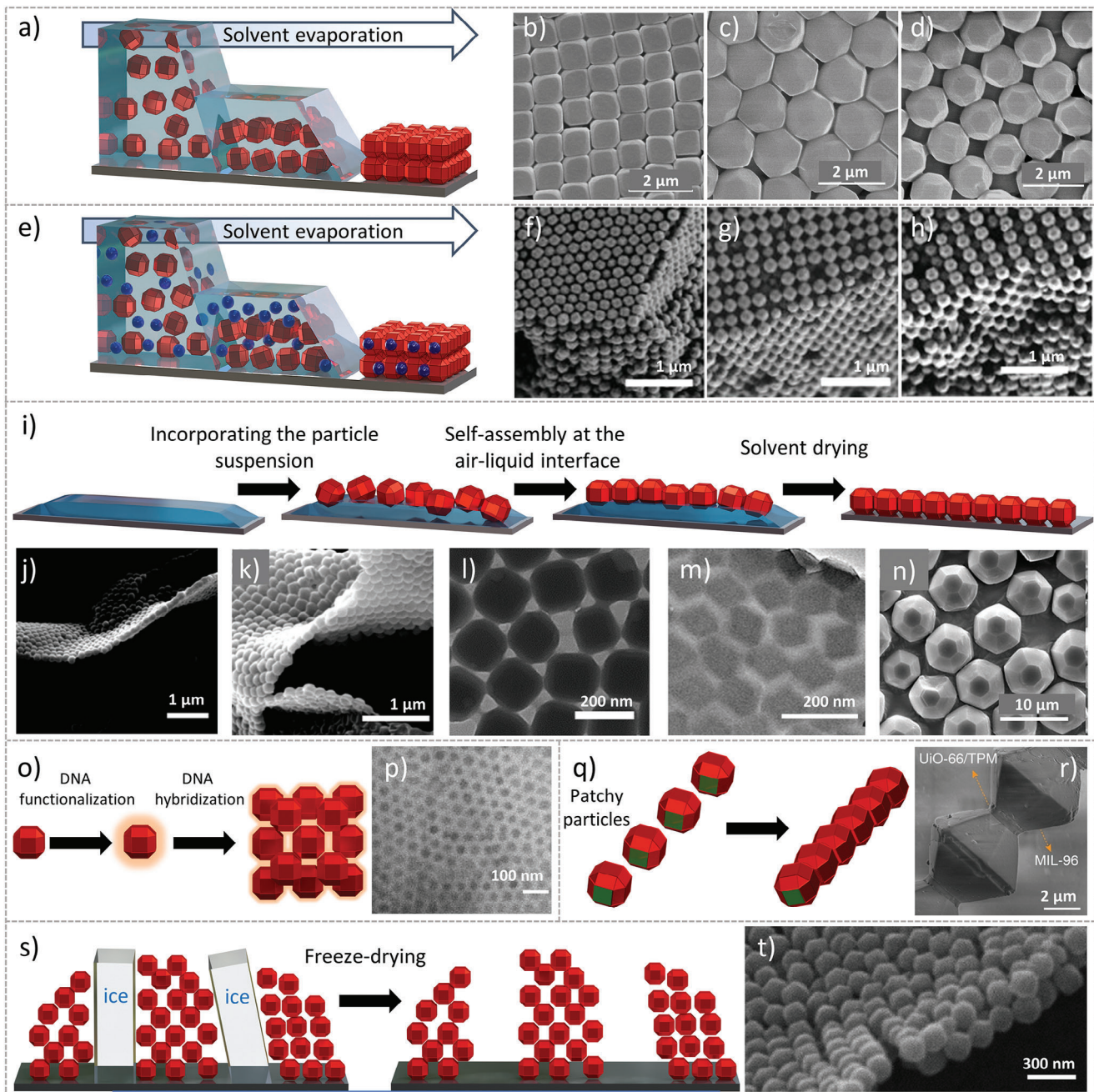


Figure 7. (a) Schematic of the solvent evaporation-based assembly. SEM images of (b) edge- and corner-rounded cubic and (c,d) (110)-truncated cubic In-soc-MOF particles. Adapted with permission.^[156] Copyright 2012, American Chemical Society. (e) Schematic of the depletion-assisted assembly. SEM images of (f) (111)-, (g) (100)-, and (h) (110)-oriented fcc supercrystals of TRD ZIF-8 particles. Adapted with permission.^[161] Copyright 2019, John Wiley and Sons. (i) Schematic of the air-liquid interface assembly. (j,k) SEM images and (l) TEM image of TRD-ZIF-8 particles assembled into monolayers. Adapted with permission.^[162] Copyright 2019, American Chemical Society. (m) TEM image of ZIF-8 monolayer membranes obtained by interfacial assembly. Adapted with permission.^[171] Copyright 2023, American Chemical Society. (n) SEM image of the bottom surface of an aligned MIL-96-PDMS thin film assembly. Adapted with permission.^[163] Copyright 2021, American Chemical Society. (o) Schematic of the DNA-assisted assembly. (p) Cryo-STEM BF image of PCN-222 nanorods with complementary DNA linkers forming 1D-oriented two-dimensional close-packed hexagonal lattices. Reproduced under terms of the CC-BY 4.0 license.^[172] Copyright 2020, The Authors, published by Springer Nature. (q) Schematic of the anisotropic pattern-assisted assembly. (r) SEM image of a chain made of assembled MOF-based patchy particles. Adapted with permission.^[177] Copyright 2021, John Wiley and Sons. (s) Schematic of the ice-templated assembly. (t) SEM image of a TRD-ZIF-8-based bilayer 2D quasi-ordered two-dimensional superstructures. Adapted with permission.^[179] Copyright, 2022 American Chemical Society.

attractive force among colloids, facilitated by the depletion interaction.^[159,160] In a pioneering demonstration from Maspoch and co-workers,^[83] 3D-oriented superstructures composed of truncated rhombic dodecahedral ZIF-8 (TRD-ZIF-8) or O-Uio-66 particles were assembled by evaporation of water in the presence of cetyltrimethylammonium bromide (CTAB), which acted as a depletant. Different 3D-oriented superstructures were obtained depending on the shape of the MOF particles: TRD-ZIF-8 particles with a truncation below 0.66 arranged into an *fcc* crystal, those with a higher truncation formed the densest rhombohedral packing, and O-Uio-66 particles adopted a hexagonal lattice.^[83] In addition, TRD-ZIF-8 particles with a truncation value of 0.63 could form different (111)-, (100)-, and (110)-oriented *fcc* superstructures by adjusting the amount of surfactant in the colloidal solution. To be more specific, (111)-oriented *fcc* superstructures were observed at low CTAB concentrations (1.00 mg mL^{-1}). Upon increasing the CTAB concentration to 2.00 mg mL^{-1} , (100)-oriented domains began to form alongside the existing (111)-oriented domains. As the CTAB concentration was further increased to 3.00 mg mL^{-1} , these (100)-oriented domains continued to grow, eventually resulting in the formation of homogeneous (100)-oriented *fcc* superstructures. (110)-oriented domains began to appear when increasing the CTAB concentration up to 3.25 mg mL^{-1} . However, purely (110)-oriented superstructures could not be obtained, even at a CTAB concentration of 4.00 mg mL^{-1} (Figure 7f-h).^[161]

In a recent study, Wang and co-workers have further investigated the role of surfactants in the assembly process of MOF particles.^[158] Ordered superstructures with different dimensionalities were created by inducing instability in aqueous colloidal solutions using the depletion interaction within a capillary. In their research, $0.9\text{-}\mu\text{m}$ RD-ZIF-8 particles assembled into a mixture of 3D (111)-, (100)-, and (110)-oriented quasi-three-dimensional *fcc* superstructures with the assistance of cetyltrimethylammonium chloride (CTAC) micelles as depletants. Conversely, by adding CTAC, $2.6\text{ }\mu\text{m}$ -RD-ZIF-8 and $1.2\text{ }\mu\text{m}$ -TRD-ZIF-8 particles rearranged into 3D-oriented chains with particles aligned in the $\langle 110 \rangle$ direction. Therefore, while preserving order, the dimensions of the final superstructures are influenced by the size and shape of the MOF particles. Likewise, when CTAC was present, hexagonal bipyramidal MIL-96 particles exhibited distinct arrangements depending on their truncation values. Particles with a truncation of 0.24 formed a 3D-oriented two-dimensional square lattice, while those with a truncation of 0.52 organized into 3D-oriented centered rectangular lattices with an axial angle of 108° . The interplay between the MOF particles and the substrate was also observed to exert an influence on the final superstructure. Thus, aided by cetyltrimethylammonium chloride (CTAC) micelles as depletants, O-Uio-66 particles were found to organize into 3D (111)-oriented two-dimensional hexagonal lattices or quasi-one-dimensional stripe-like superstructures, depending on the smoothness or roughness of the substrate, respectively. Similarly, by using sodium dodecyl sulfate (SDS) as a depletant, the assembly of MIL-88A hexagonal rods varied based on the substrate. On smooth substrates, MIL-88A hexagonal rods formed one-dimensional chains with 3D orientation, while on rough substrates, these particles rearranged into two-dimensional snowflake-like superstructures with 1D-orientation.^[158]

2.4. Air-liquid Interface Assembly

An alternative approach to assemble colloidal MOF particles into superstructures employs the air-liquid interface (Figure 7i). This method begins by spreading an insoluble monolayer of MOF particles over an interface between air and liquid. Following this strategy, the interface is manipulated to facilitate particle assembly and organization. Among the different modifications of the interface, the increase in the surface tension of the liquid can favour the contact and assembly of the MOF particles.^[146,162] Cohen and co-workers illustrated the formation of 1D (111)-oriented two-dimensional superstructures by assembling monodisperse TRD-ZIF-8 particles at an air-liquid interface (Figure 7j-k).^[162] First, core-shell ZIF-8 particles were created by coating ZIF-8 particles with a poly(methyl methacrylate) (PMMA) layer (PMMA@ZIF-8). PMMA@ZIF-8 particles dispersed in toluene were spread on water. Subsequently, as toluene evaporated, the particles assembled into 1D-oriented two-dimensional films at the air-liquid interface, forming free-standing films through the fusion of their PMMA@ZIF-8 shells.^[162] The same research group has also explored how different casting solvents (*n*-butanol, tetrahydrofuran, ethyl acetate, CH_2Cl_2 , CH_3Cl , toluene, hexane, and cyclohexane) modify the surface tension of the interface and, consequently, the assembly of MOF particles (hexagonal bifrustum MIL-96, O-Uio-66 and O-Uio-66-NH₂ particles).^[163] Heat-curable polydimethylsiloxane (PDMS) was also added to the casting solvents to immobilize the oriented MOF particles in large-area polymeric films. Briefly, the casting dispersion, which contained MOF particles, casting solvent, and PDMS, spread rapidly over the water interface. As the casting solvent spread, the suspended MOF particles aligned, while the dissolved PDMS diffused freely throughout the casting solvent layer. Evaporation of the casting solvent concentrated the PDMS, increasing its viscosity and retaining the MOF alignment. Finally, MOF-PDMS films were heated to cure the PDMS. The use of solvents that result in low interfacial tension (*n*-butanol, THF, or ethyl acetate) led to films with the trapezoidal facets of MIL-96 facing upward (alignment along the $\langle 102 \rangle$ direction). Conversely, as the interfacial tension increased (CH_2Cl_2 and CH_3Cl), the alignment of the MIL-96 particles with the hexagonal facets upward became dominant (alignment along the $\langle 002 \rangle$ direction). An interfacial tension higher than 36.1 mN m^{-1} caused an uneven spreading of the solvent on the water surface and an aggregation of MOF-PDMS. Similar behaviours were found for the O-Uio-66 particles.^[163]

Monodispersed O-Uio-66 particles were also observed to form 1D (111)-oriented two-dimensional superstructures at an air-liquid interface. Specifically, octahedral Uio-66 particles were initially dispersed over water, and then the introduction of SDS altered the surface tension, resulting in the consolidation of Uio-66 particles into a disordered two-dimensional hexagonal monolayer. The disorder was attributed to the rapid packing of octahedral Uio-66 particles following the addition of SDS.^[146] Recent research has explored the influence of attached molecular chains on O-Uio-66 particles during their assembly into Uio-66 monolayers at the air-water interface.^[164] Initially, O-Uio-66 particles of varying sizes (80 nm, 120 nm, and 250 nm) were modified with different polymers (poly-[methyl acrylate] [PMA], PMMA, and poly-[benzyl methacrylate] [PBnMA]), followed by their

assembly at the air-water interface. While consistently maintaining the 1D orientation, the degree of order in these monolayers was influenced by various factors, including the length and hydrophilicity of the graft, and the size of the O-Uio-66 particles. For example, extending the graft length or intensifying hydrophilicity led to a loss of order. Furthermore, in terms of particle dimensions, larger particles facilitated the development of ordered, two-dimensional hexagonal lattices.^[164]

A different modification of the air-liquid interface is to compress the MOF particles floating on the liquid subphase, a process known as Langmuir-Blodgett (LB).^[133,165] This approach is exemplified in the study by Kitagawa, Furukawa, and coworkers, where they reported the assembly of HKUST-1, Al₁₂O(OH)₁₈(H₂O)₃(Al₂(OH)₄)(BTC)₆, and Cu₂(BDC)₂(bipy) particles into two-dimensional superstructures using the LB process.^[133] First, MOF particles suspended in dry methanol were spread over water, forming a temporary bilayer of alcohol and water. MOF particles were then compressed along the air-liquid interface to assemble into two-dimensional superstructures.^[133] The assembly of MOF particles on the water sub-phase was proposed to be driven by interparticle attractive forces and capillary forces.^[166-169] Two-dimensional superstructures with 1D orientation were also formed through the assembly of rhombic dodecahedral (RD), slightly truncated cubic (TC) and TRD ZIF-8 particles using the LB process. While the RD and TC ZIF-8 particles were aligned along the [110] and [100] directions, respectively, the TRD-ZIF-8 particles did not show a specific orientation within the monolayers.^[170] An extension of the interfacial synthesis concept to liquid/liquid interfaces was recently demonstrated by Qiu et al., who obtained OOP-oriented monolayer membranes composed of RD ZIF-8 particles, by assembly at the interface between two immiscible liquids (hexadecane and MeOH-H₂O mixtures) aided by a superlyophilic substrate.^[171] The authors obtained ZIF-8 membranes oriented in two different directions, <110> and <111>, which were controlled by the solvent composition of the MeOH-H₂O mixtures.

2.5. DNA-Assisted Assembly

An alternative approach to prepare 3D-oriented superstructures involves the assembly of oligonucleotide-patterned MOF particles, harnessing their complementary interactions (Figure 7m).^[172,173] Examples of this method include the assembly of DNA-functionalized O-Uio-66 particles and PCN-222 nanorods, as reported by Mirkin and co-workers.^[172] In their study, before DNA functionalization, the MOF surface was protected from unmodified DNA using a set of heterobifunctional polyethylene glycol (phosphate/phosphonate-PEG_n-N₃) ligands with three different PEG chain lengths (ethylene, PEG₄, and PEG_{5k}). The PEG_{5k}-based ligand proved to be most effective in stabilizing the MOF colloid and making the particles susceptible to subsequent DNA functionalization. Following that, the MOF particles terminated with azide groups underwent a reaction with terminal diarylcyclooctyne-modified DNA (5' DBCO-TEG modifier) through the strain-promoted azide-alkyne cycloaddition reaction.^[174] Specifically, Uio-66 particles, functionalized with complementary DNA sticky ends (5'-GCGC), were found to assemble into 3D-oriented *fcc* lattices. In contrast, when

two sets of Uio-66 particles possessed complementary DNA sticky ends (5'-AAGGAA and 5'-TTCCTT), they arranged into 3D-oriented *bcc* lattices. Likewise, DNA-functionalized PCN-222 nanorods formed 1D-oriented two-dimensional close-packed hexagonal lattices when the particles featured complementary DNA linkers (Figure 7n), and they assembled into tetragonal lattices when particles with complementary DNA sticky ends were involved.^[172]

2.6. Anisotropic Pattern-Assisted Assembly

Another strategy to govern the assembly of MOF particles is through their anisotropic patterning, which facilitates both their orientation and arrangement (Figure 7o). Anisotropically patterned MOF particles, also known as MOF-based patchy particles, must incorporate crucial bonding information, including the quantity and directionality of bonds per particle, for precise assembly guidance.^[175,176] Indeed, the interactions among these MOF-based patchy particles must be both strong and short-ranged, while still allowing particles to adjust their positions and orientations as needed. This method has been exemplified by the assembly of Uio-66-on-MIL-96 particles into 3D-oriented one-dimensional chains.^[177] Initially, uniform micrometer-sized truncated hexagonal dipyramidal MIL-96 particles were solvothermally synthesized. Subsequently, Uio-66 was selectively grown on the (0002) facets of truncated hexagonal bipyramidal MIL-96 particles. The alignment between the (0002) planes of MIL-96 and the (111) planes of Uio-66 supported this heteroepitaxial growth. The Uio-66 patches exhibited a hexagonal appearance, resembling the shape of the MIL-96 facets. Following that, in the presence of a dimethylformamide (DMF)/H₂O co-solvent, nucleation of 3-(trimethoxysilyl)propyl methacrylate oligomers (o-TPM) occurred on the Uio-66 patches, whereas o-TPM nucleation on the MIL-96 surface was completely inhibited. This inhibition was proposed to occur because MIL-96 electrostatically repels o-TPM. It should be noted that, while o-TPM nucleated on both MIL-96 and Uio-66 surfaces in pure water solvent, nucleation on the MIL-96 surface was completely suppressed in the presence of 50 v/v% DMF/H₂O co-solvent. Finally, Uio-66 patches, which had a thin layer of o-TPM, bonded to each other when subjected to stirring. The patches adhered to each other, producing a strong, reconfigurable capillary force that aimed to improve contact between them. Therefore, the o-TPM merged from the patches of two particles, maximizing their contact and thereby forming the 3D-oriented one-dimensional chains (Figure 7p).^[177]

2.7. Ice-Templated Assembly

Recently, ice-templated assembly, also known as freeze casting,^[178] which relies on assembly within confined spaces formed between ice crystals (Figure 7q), has been employed to assemble MOF particles into superstructures with 1D order.^[179] Aqueous suspensions of MOF particles (TRD-ZIF-8, C-ZIF-8, O-Uio-66 or MIL-88B(Fe)-NH₂ hexagonal nanorods) were first frozen in liquid nitrogen, resulting in polycrystalline ice that forced the MOF particles into gaps between neighbouring ice crystals. Following that, MOF particles underwent

assembly through the freeze-drying process. Van der Waals forces played a crucial role in preserving the cohesion of the MOF particles once the ice templates sublimated. This innovative approach resulted in the formation of MOF-based mono- and bilayer 2D quasi-ordered two-dimensional superstructures, with the specific configuration dependent on the initial concentration of the MOF colloids (Figure 7r).^[179] Notably, unlike other methods, the ice-templating approach does not require MOF particle size and shape monodispersity. However, it is important to recognize that the degree of control over monolayered superstructures depends on the degree of control over the ice formation. Thus, fluctuations in controlling the ice formation can result in subsequent misalignments of crystalline domains.

2.8. Conclusions and Perspectives

The assembly of colloidal MOF particles facilitates the formation of MOF-based superstructures, offering control over their spatial geometries and, consequently, their anisotropic properties. Advances in synthesizing stable, monodisperse colloidal MOF particles have positioned them as a distinguished class of polyhedral particles for assembly into oriented superstructures. This progress is expected to expand the range of attainable superstructures, which could lead to intricate and unconventional-oriented assemblies. Nonetheless, it is essential to acknowledge that the assembly of MOF particles remains a complex and challenging task. There exists a demand for continued advances in synthetic methodologies aimed at precisely regulating MOF particle interactions and their interactions within their environment. Another important aspect to consider regarding oriented MOF-based superstructures prepared using reported assembly methods is their weak cohesion, which limits their practical applicability. The stability of the superstructures can be improved by using a polymer to bind the oriented MOF particles together. However, this methodology faces the combined challenges of simultaneously enhancing the mechanical stability of the superstructures while preserving the order and intrinsic porosity of the MOF particles in larger domains. Despite the challenges, we are confident in the ongoing advancement of oriented MOF superstructures through assembly. The anticipated developments and growth in this field suggest exciting progress on the horizon.

3. Oriented polycrystalline MOF superstructures by external forces

3.1. Introduction

Besides spontaneous colloidal assembly, the orientation of MOFs and generation of their superstructures can be achieved via the imposition of external forces through magnetic, electric and/or gravitational fields. Magnetic or electric field alignment to generate oriented MOF superstructures is attractive as it represents a robust, yet easily tuneable method to control MOF orientation, circumventing some of the challenges associated with spontaneous particle assembly such as the prerequisite of monodisperse MOF particles and the delicate balance of particle and environmental interactions.^[180] In contrast, external field alignment

relies upon the introduction of dipoles along a specific crystallographic direction of the selected MOF particles, and their subsequent alignment along the imposed field direction due to potential energy minimization.^[181,182] However, to ensure selective particle orientation, the dipole alignment energy of the particles for the desired orientation must be sufficiently high compared to that of the undesired orientations along the imposed field. Additionally, it should be robust enough to overcome thermal randomization and counteract rotational inertia arising from matrix viscosity.^[183,184] Therefore, the generation of oriented MOF arrangements via external fields is typically limited to anisometric particles^[185] where the length exceeds (L) the width (D), see Figure 8a; for these systems, the ratio between the aforementioned dimensions is referred to as the aspect ratio (AR). When the AR of the MOF crystals is greater than 1, a sufficient energetic differentiation can be induced with an external field. When employing a uniaxial external field, the achieved orientation is predominantly 1D-oriented, whether it is in the OOP or IP direction. As demonstrated in Section 2, achieving 3D-orientation necessitates particles with high monodispersity in size and shape to establish robust interparticle facet-to-facet interactions or another compelling force that enforces crystal orientation in more than one direction. In the following section, we examine the main examples of these approaches and include considerations to expand the degree of orientational control via the external force approach to obtain 3D-oriented MOF superstructures.

3.2. Magnetic-field Assisted Alignment

Typically, the usage of magnetic fields for material manipulation is limited to materials that possess ferromagnetic or paramagnetic properties, which excludes most classes of MOFs. To bypass this limitation, Cheng et al.^[145] focused on a general method to magnetize rod or needle-shaped MOF crystals by exploiting electrostatic attractions between the MOFs and oppositely charged Fe_3O_4 nanoparticles to attach the Fe_3O_4 onto the external crystal surfaces of the MOFs. The zeta potentials of colloidal particles in aqueous media depend upon the pH of the dispersion – two types of particles in a colloidal dispersion can thereby be rendered oppositely charged by selecting a pH in between their isoelectric points. $\text{NH}_2\text{-MIL-53(Al)}$ was selected as a representative MOF crystalline system; these particles with AR = 21 were coated with poly(acrylate)-stabilized iron oxide nanoparticles. The utilized Fe_3O_4 nanoparticles bear a negative electrostatic charge above pH 2.8 whereas the $\text{NH}_2\text{-MIL-53(Al)}$ microneedles are positively charged below pH 10.5 due to the protonation of the amine group. Briefly, a buffered solution of 10 wt% of Fe_3O_4 nanoparticles at pH 3.5 was added to a buffered suspension of MOF at the same pH, leading to magnetized $\text{NH}_2\text{-MIL-53(Al)}$ microneedles. The resulting materials were characterized by XRD showing that the $\text{NH}_2\text{-MIL-53(Al)}$ microneedles retain their XRD patterns after treatment with iron oxide particles. The presence of Fe_3O_4 nanoparticles was confirmed by ICP-MS and thermogravimetric analysis. When exposed to a magnetic field, magnetized particles experience a torque to align their magnetic dipoles along the field (Figure 8a).^[181] Optical microscopy showed that when aqueous suspensions of the magnetized $\text{NH}_2\text{-MIL-53(Al)}$

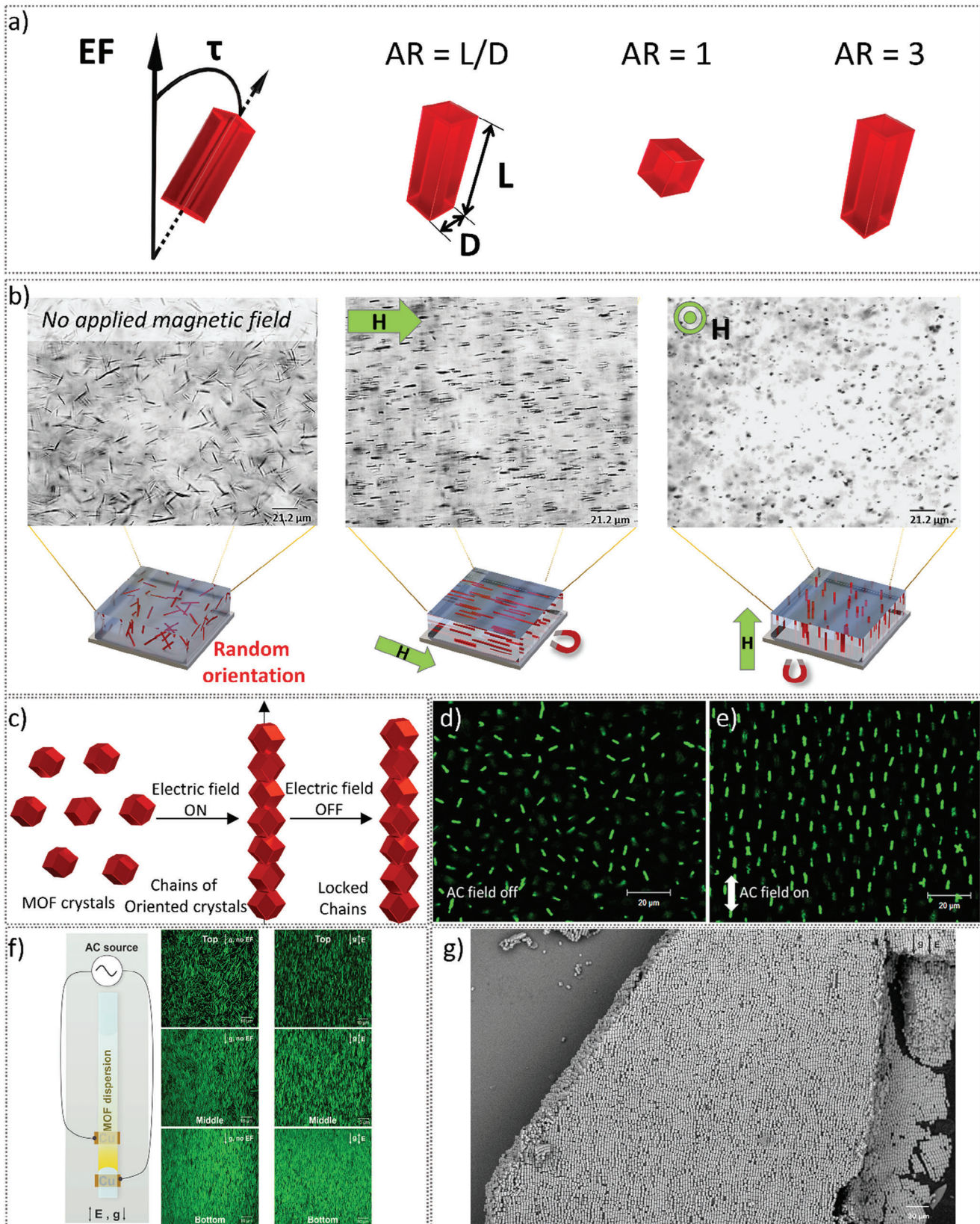


Figure 8. (a) Schematic showing an anisotropic particle, the torque (τ) related to an external field (EF) and the definition of aspect ratio (AR) with examples. (b) Random orientation (left); alignment along the direction of the applied magnetic field (middle); alignment perpendicular to the major

crystals were placed in a magnetic field, the randomly oriented MOF crystals rapidly aligned in the [001] direction along the field, dynamically responding to changes in the field direction (Figure 8b). We note that the dynamic response of this class of composites (aka magnetic framework composites)^[186] was previously used for dynamic positioning but not for the alignment of MOF crystals.^[187] In the case of Fe₃O₄-coated NH₂-MIL-53(Al) crystals, to fix them in their aligned state, the magnetized MOFs were dispersed in a methacrylate-based, photocurable resin. Magnetic alignment of NH₂-MIL-53(Al) crystals readily took place even in the viscous resin (dynamic viscosity of 900 cP at 25°C; that of deionized water is 0.89 cP at 25°C). The versatility of this approach was demonstrated by aligning Fe₃O₄-coated NU-1000 with AR = 5.9.^[145] NU-1000 exhibits unique optical properties along the *c*-crystallographic axis. Thus, its fluorescence response to 405 nm linearly polarized radiation when magnetically aligned was investigated showing different behaviors with respect to the unaligned NU-1000. The highest fluorescence response occurred when the incident light polarization was in alignment with the [001] direction of the NU-1000 crystals. In both MOF examples, 1D-oriented three-dimensional systems were obtained, and the orientation distributions of MOF particles were assessed via optical microscopy coupled with ImageJ directionality analysis. A detailed XRD analysis of particle orientation was not carried out, as the low MOF loading and high polymer content prevented accurate quantification. More recently, van Essen et al.^[188] used a similar procedure to magnetize and align ZIF-8 in a polyimide (Matrimid) membrane for CO₂ separation from N₂, magnetizing the ZIF-8 particles with PEG-coated Fe₃O₄ nanoparticles. Magnetically aligned films were then prepared by adding the desired quantity (wt%) m-ZIF-8 to a Matrimid/DMF suspension. The suspension was then dried under a magnetic field resulting in the solidification of the film. SEM cross-sectional analysis of the films showed that instead of a homogeneous ZIF-8 distribution throughout the Matrimid matrix, the magnetic field induced the m-ZIF-8 to arrange into bands of higher particle density, which in turn were generally oriented perpendicular to the membrane plane. However, it should be noted that the crystallographic orientation of the m-ZIF-8 particles themselves was not demonstrated. Nevertheless, the aligned m-ZIF-8 doped Matrimid membranes showed an improved permeability without compromising the CO₂ selectivity up to 15 bar, due to the increased ZIF-8 interparticle connectivity in the aligned versus the unaligned composites. The CO₂ selectivity is caused by the different kinetic diameters of CO₂ (3.30 Å) and N₂ (3.64 Å), the former being smaller than the pore aperture of ZIF-8 (3.4 Å), while the latter is bigger. Arrangement of ZIF-8 into banded regions with higher particles density therefore promotes CO₂ over N₂ diffusivity in the aligned membranes.

plane of the sample, along the direction of the magnetic field (the microneedles appear as dark spots) (right). Adapted with permission.^[145] Copyright 2017, John Wiley and Sons. (c) Schematic illustration of the electric-field-assisted (E-field assisted) assembly of rhombic dodecahedra-shaped ZIF-8 crystals (sodalite ZIF-8). Adapted with permission.^[192] Copyright 2012, American Chemical Society. Confocal microscope images of NU-1000_{Si} crystals in bromobenzene (d), (e) without and with the presence of an electric field, respectively. Adapted with permission.^[86] Copyright 2019 American Chemical Society. (f) Illustration of sedimentation experiment in a glass capillary with alternating E-field parallel to gravity (left); Top to bottom: CLSM images of NH₂-MIL-53(Al) assembly at the top, middle and bottom of the sedimentation layer, in the absence of E-field (middle); Top to bottom: CLSM images of NH₂-MIL-53(Al) assembly at the top, middle and bottom of the sedimentation layer in presence of E-field parallel to gravity (right). (g) SEM image of opened capillary sample containing MIL-68(ln) sedimented in a vertical E-field showing the long-range order of the particles. Reproduced under terms of the CC-BY 4.0 license.^[82] Copyright 2022, The Authors, published by Elsevier B.V.

It is increasingly recognized that major technological breakthroughs of MOFs in device fabrication are tied to the control over MOF crystalline orientation, and consequently pore alignment, in both MOF films and patterns.^[15] Magnetic functionalization and alignment of MOF prior to their fixation in polymers offer a practical way to address this challenge. Most studies on magnetic orientation of particles relies upon uniaxial static fields; however, there are examples of biaxial nematic particle assemblies achieved via rotating magnetic fields, where the primary particles are oriented along two axes (2D-oriented system).^[189–191] We note that, for these 2D-oriented systems, the primary particles require a biaxial rather than a uniaxial symmetry in addition to more complex experimental designs. Nevertheless, such approaches could conceivably be extended to certain biaxial MOF materials, thereby imposing a greater degree of control and potentially leading to 3D-oriented MOF assemblies.

3.3. Electric-Field Assisted Alignment

In 2013, Yanai et al.^[192] reported the use of an electric field (E-field) to align MOF particles. Monodispersed, rhombic dodecahedra-shaped ZIF-8 crystals have been oriented to form facet-to-facet contacts by applying an E-field. Particles attach to one another within seconds showing, via optical microscopy, elongated hexagons indicating the {110} crystal orientation, parallel to the direction of the E-field. Within a few minutes, successive growth led to the formation of 1D-oriented one-dimensional superstructures (i.e., chains) aligned in the direction of the imposed field (Figure 8c). This configuration minimizes the center-to-center separation between particles, likely serving to maximize the dipole–dipole interaction as well as van der Waals interactions between the {110} facets of adjoining crystals. Two frequencies were investigated, 1 kHz and 1 MHz, both leading to the formation of 1D-oriented MOF chains. Interestingly, chained alignment collapsed after switching off the E-field for chains constructed at a frequency of 1 MHz whereas it remained stable when constructed under a 1 kHz field. At high frequency, the dominant mechanism of attraction is the dielectric polarization of the crystal particle while at low frequency, the polarization of the double layer dominates, favoring direct surface-to-surface contact between particles and overcoming electrostatic repulsion.^[193] The latter mechanism allows particles sufficiently close to each other to adhere through van der Waals attraction. However, when moving to truncated rhombic dodecahedral ZIF-8 crystals possessing both {110} and {100} facets, it was found that although 1D-oriented chains of the ZIF-8 crystals could form, the crystals showed a mixture of {110} and {100} orientation due to non-selective facet-to-facet adhesion, indicating that

particle orientation within the chains largely derives from van der Waals interactions.

Chin and co-workers^[86] recently reported the E-field-assisted alignment of NU-1000 microrod crystals with AR = 6.1. NU-1000 was functionalized with trimethoxy(octadecyl)silane (TMODS) to form NU-1000_{Si} by sonicating a suspension of NU-1000 in a mixture of TMODS, butylamine, and dried toluene (1/1/10, v/v/v) for 4 h, thereby improving its dispersibility in organic solvents. XRD indicates that the NU-1000_{Si} retains its crystalline framework structure after silanization, whereas the presence of Si was confirmed by ICP-MS. When no E-field was applied, the MOF crystals were randomly oriented in the solvent and underwent Brownian motion and rotation (Figure 8d). Upon application of the E-field, the NU-1000_{Si} rapidly aligned along the [001] direction parallel to the imposed E-field (Figure 8e). Unlike in the earlier example with ZIF-8, the alignment of the NU-1000_{Si} microrods was suggested to happen through Maxwell-Wagner-Sillars and O'Konski interfacial polarization.^[194–196] It was hypothesized that the E-field-assisted alignment of the microrods resulted from the electromigration of ions that were present within the MOF channels and in the electrical double layers.^[196] This electromigration induced dipoles in the MOF crystals, thereby facilitating their alignment. The ions found within the MOF channels originated from the adsorbed water and polar groups, as well as from the sample preparation process. It is important to note that the repulsion between particles prevented the chaining of NU-1000_{Si} particles. The birefringent MOF particles allowed for light transmission through crossed polarizers, whereby the light transmission through aligned MOFs was minimized in the utilized set-up. Therefore, the NU-1000_{Si} alignment could be assessed via polarized optical microscopy coupled with a photodetector, showing an alignment response time of 0.1 seconds. As previously mentioned, one significant characteristic of NU-1000 is its enhanced photoabsorption (and consequently its fluorescence response) in the [001] crystallographic direction, along the major axis of the microrod crystals. To investigate the fluorescence response, studies were conducted on NU-1000_{Si} suspensions. Similarly, as observed with NU-1000 under magnetic field alignment, the fluorescence properties are highly dependent on the particle orientation. The highest fluorescence intensity was observed when the angle was 0°, while the lowest fluorescence occurred at an angle of 90°.

In a subsequent study, Chin and co-workers extended the E-field-assisted alignment to NH₂-MIL-53(Al) and MIL-68(In) crystals, and incorporated gravitational sedimentation to pack and generate 1D-oriented three-dimensional MOF superstructures.^[82] As described by Onsager,^[197] for rod-shaped particles, their aligned packing into a nematic phase is thermodynamically favored when their particle volume fraction is sufficiently high, for particles with AR \geq 4.7.^[198] Nevertheless, by applying an E-field during MOF sedimentation, highly 1D aligned three-dimensional MOF assemblies were achieved, even for MOF crystals with low AR of 1.2. 8wt% NH₂-MIL-53(Al) (AR ranging from 5 to 15 due to particle size polydispersity), 10 wt% photopolymerizable trimethylolpropane triacrylate (TMPTA) and 1 wt% diphenyl (2,4,6-trimethylbenzoyl) phosphine oxide (TPO) photoinitiator were dispersed in DMF, selected as a solvent for its high dielectric constant, then loaded in a glass capillary by diffusion. Upright positioning of the glass capillary allowed the

particles to sediment. Subsequently, the sample was photopolymerized to fix the assemblies for confocal microscopy and SEM. In the absence of an applied E-field, when observing the sample from the top of the capillary toward the bottom, the increasing particle packing density led to an enhanced alignment of the MOFs along the capillary, forming an oriented nematic phase at the bottom of the sediment layer. However, in the case of particle sedimentation in the presence of an external alternating E-field approximately parallel to gravity (1 MHz, 400 V_{p-p}, E-field \sim 14 V·mm⁻¹_{p-p}), NH₂-MIL-53(Al) microneedles showed vertical alignment along the [001] direction throughout the sedimentation layer, forming a nematic phase. In this instance, as the E-field imposes a supplementary driving force for alignment, MOF alignment was observed even at lower packing density towards the top of the sedimentation layer (Figure 8f) where entropic interactions would otherwise be insufficient to form a classic nematic assembly. Similar conditions were applied to MIL-68(In) displaying a slightly lower AR of 6.8. Unlike NH₂-MIL-53(Al), MIL-68(In) particles show a low degree of directional order when in the absence of an E-field due to their lower AR. Nonetheless, when the particles were aligned under an alternating potential applied to the electrodes (1 MHz, 400 V_{p-p}, E-field \sim 14 V·mm⁻¹_{p-p}), the resulting assemblies again show [001] alignment of the MOF microrods into a nematic phase throughout the sediment layer (Figure 8g). The relatively small dimensions of the ordered MOF domains, as well as their encasement within a polymer matrix and glass hindered their precise orientational assessment via conventional XRD analysis. Therefore, particle orientation was assessed via optical microscopy or SEM coupled with ImageJ software directionality analysis instead. The authors then investigated NU-1000 displaying an AR of 3.4, which is below the expected AR of 4.7 to undergo nematic phase formation via purely entropically driven assembly.^[198] Due to the tendency of NU-1000 to adhere to the capillary glass walls, arising from the presence of unsaturated Zr₆ nodes able to bind to Si-OH groups of the glass surface, the experimental conditions were modified. Difluorobenzene (DFB) instead of DMF was used, but as DFB polarity is lower than DMF, increased interparticle electrostatic repulsion is expected. To mitigate this effect, 0.01 wt% tetrabutylammonium bromide (TBABr) was added to screen the interparticle electrostatic repulsion and allow dense particle packing. When the mixture was loaded in a glass capillary and allowed to sediment in the absence of an E-field, the microrods were largely disordered across the sedimentation layer. However, the application of an E-field markedly improved alignment in the [001] direction from the top to the bottom of the sedimentation layer. A similar observation was made when moving to MIL-68(In) crystals of yet lower AR of 1.2, demonstrating the utility of E-field imposition to control the alignment even of particles with ARs closer to unity. In the aforementioned instances, the uniaxial external field induces a pronounced [001] alignment in all particle systems (1P-1D-oriented system). However, in the case of NU-1000, the uniformity of the MOF particles enhances their packing interactions, whilst the robust crystal facet-to-capillary glass and interparticle facet-to-facet interactions contribute to achieving a heightened degree of orientation. In fluorescence microscopy, when employing polarized excitation methods like in CLSM, the orientation of MOF particles can be qualitatively evaluated based on their emission characteristics, provided that the MOFs bear oriented

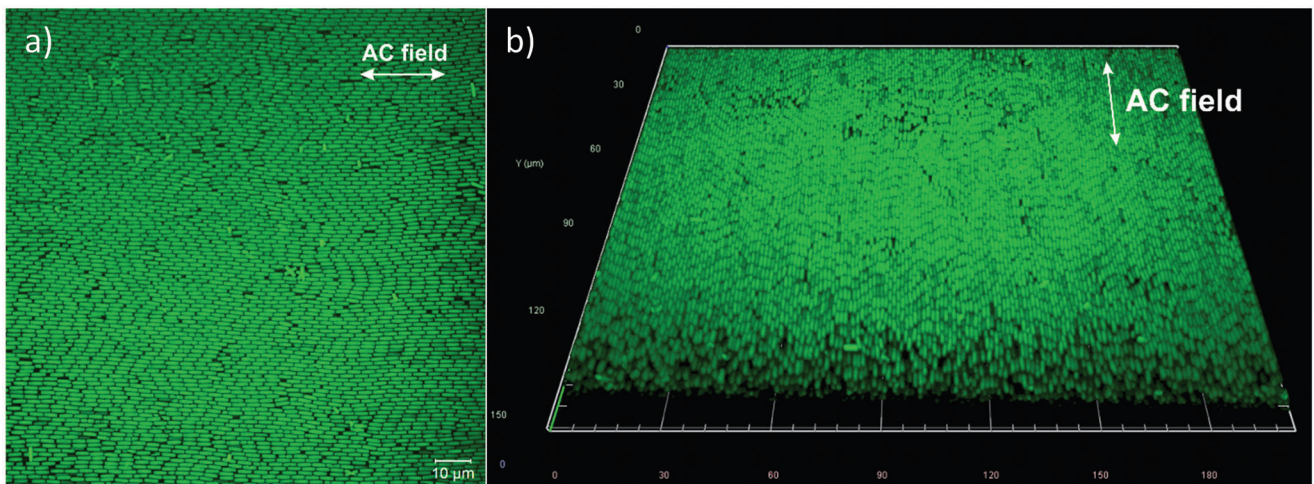


Figure 9. (a) CLSM image of NU-1000 assembly showing the well-packed particle; (b) CLSM tilted Z-stacked image of the NU-1000 assembly edge and the aligned layers below the top layer. Reproduced under terms of the CC-BY 4.0 license.^[82] Copyright 2022, The Authors, published by Elsevier B.V.

fluorophores either within their pores^[158] or integrated as part of the MOF lattice, such as in the case of NU-1000. Examination of NU-1000 assemblies via confocal microscopy reveals that the particles predominantly appear as uniformly bright rectangular structures. This observation suggests the formation of extended 3D-oriented superstructures, with the rectangular {100} facets of NU-1000 crystals facing the boundary glass wall towards the viewing direction (**Figure 9**). However, it should be noted that quantitative assessment via XRD analysis is missing. To effectively generate 3D-oriented MOF assemblies by integrating field-assisted MOF orientation with interparticle interactions, maximizing facet-to-facet interactions is crucial. The success with this objective depends on the particle uniformity and particle morphology. For instance, the contact areas between individual facets are expected to be enhanced in board or lath-shaped particles compared to the hexagonal rods of NU-1000.

More recently, Chin, Wuttke and co-workers have focused their efforts on maximizing the solvent-responsive anisotropic breathing properties of MIL-88A:^[199] Mellot-Draznieks et al. demonstrated the decrease of the crystalline unit cell parameter *c* from 15.31 to 12.66 Å coupled with the increase of the *a* parameter from 9.26 to 12.66 Å when going from the dry as-synthesized MIL-88A to its hydrated form.^[200] The Maspoch group first showed the applicability of MIL-88A breathing properties in the conception of MIL-88A/PVDF actuating composite films,^[201,202] which was subsequently expanded upon by Jia and co-workers to generate films with responsive structural color.^[203] However, to fully exploit the anisotropic breathing of MIL-88A for actuation, a highly ordered MOF@polymer film is necessary. Indeed, when randomly oriented, the swelling/shrinkage of different particles in multiple directions cancels out to some extent. To address this problem, monodispersed MIL-88A microparticles (AR of 10.5) were aligned via an external E-field and then fixed in PEGDA. The MOF particles (18 wt%) were dispersed in a mixture of 9:9:1 (v/v/v) PEGDA₂₅₀, PEGDA₇₀₀, TMPTA with a 0.5wt% TPO photoinitiator. The MOF containing mixture was then dispersed in *N,N*-dimethylacetamide solvent (dielectric constant,

$\epsilon = 37.8$) and placed under an E-field (500 kHz, 100 V/mm). Cross-sectional analysis of the resulting film by SEM showed the successful 1D-alignment of the MOF particles along the [001] direction, forming an IP-1D-oriented three-dimensional system. The actuation properties of both aligned and unaligned MIL-88A@PEGDA films were investigated, whereby the film bearing aligned particles showed a significantly stronger response to humidity, with a strong curling behaviour as humidity increased and vice versa, while the unaligned-gradient large film showed inconsistent curling behaviour.

3.4. Conclusions and Perspectives

The use of external magnetic or electric fields opens up additional avenues for the manipulation of MOF particle assembly, allowing precise and tunable control over IP-1D-oriented MOFs and packing whilst relieving some of the general constraints associated with self-assembly of colloidal MOF particles such as particle homogeneity and the delicacy of procedures involved. However, magnetic field usage suffers from the limited types of inherently magnetic MOFs, thereby requiring additional synthetic steps to render the MOF magnetic (e.g., the preparation of magnetic framework composites). Nevertheless, magnetic fields can be easily applied across macroscopic areas to form centimeter scale structures with oriented MOFs.^[145] In contrast, E-fields can be directly applied to as-synthesized MOF crystals, without the need for post-synthetic modification. However, the generation of sufficiently strong E-fields across large areas requires cumbersome set-ups and entails safety concerns due to the high voltages required. In cases where field-assisted alignment of MOFs relies upon the orientation of magnetic or electric dipoles along the imposed field, sufficient energetic differences between aligned and unaligned particles must be present to promote reliable MOF alignment over thermal randomization. Typically, these approaches are therefore limited to anisotropically shaped particles and control of MOF orientation in one direction (1D-oriented

MOF superstructures). Preliminary results have shown potential for the fabrication of 3D-oriented superstructures. We believe that the 3D-oriented domain size could be enlarged via the judicious design of the MOF particle morphology and by combining the effect of external fields with pre-patterned substrates.

4. Oriented polycrystalline MOF superstructures by heteroepitaxial ceramic-to-MOF conversion

4.1. Introduction

Ceramic materials are useful precursors for the fabrication of MOF polycrystalline superstructures. In 2010, ceramics were used for their MOF seeding properties that allowed the preferential growth of randomly oriented MOF crystals on ceramic particles.^[104,204] However, more recently, ceramics have been explored as they can function as feedstock material (source of the metal precursors) and for their architecture-directing properties.^[44] This approach is appealing because ceramics offer straightforward means of controlling the structuralization of MOFs, which encompasses factors such as the superstructure's morphology, and, in certain instances, the alignment of the constituent crystals. Kitagawa, Furukawa, and co-workers first described this concept by employing alumina structures as a template to form the MOF $[\text{Al}(\text{OH})(\text{NDC})]_n$.^[205] Following this report, other ceramic substrates, such as $\text{Ni}(\text{OH})_2$,^[206] $\text{Cu}_2\text{CO}_3(\text{OH})_2$,^[207] and $\text{Co}(\text{OH})_2$,^[208] were used as sacrificial metal sources. Furthermore, ZnO is a well-studied precursor for the formation of zeolitic imidazolate frameworks (ZIFs).^[112,209] For example, fractal ZnO nanoparticle networks were shown to produce ZIF-8 crystal structures preserving the initial fractal arrangement.^[210] Although many of these examples result in MOF crystals with random crystalline orientation, the progress in the ceramic-to-MOF conversion has been successfully applied to the fabrication of oriented MOF films. In the following sections, we discuss the progress of this research field focusing on significant demonstrations of the growth of OOP 1D-oriented MOF films from ZnO substrates up to the most recent advances in fabrication protocols of 3D-oriented MOF coatings from $\text{Cu}(\text{OH})_2$ nanostructures. In the following section, films and coatings are used to describe extended two-dimensional MOF superstructures supported by substrates (e.g., silicon, glass, polymers).

4.2. Ceramic-to-MOF conversion from ZnO substrates

Oriented ZIF-8 thin films were prepared using one-dimensional ZnO as a sacrificial template by Zhou et al.^[211] Titanium sheets were selected as a substrate for the electrodeposition of ZnO nanorods perpendicular to the support surface. In a one-pot procedure, the ZnO substrate was then immersed in a methanolic solution of ZIF-8 precursors ($\text{ZnCl}_2 = 0.08 \text{ M}$; $\text{HmIM} = 0.16 \text{ M}$) and sodium formate (0.08 M) and held at 100°C for 10 h. XRD analysis of the obtained ZIF-8 films identified the (002) reflection as the dominant peak of the sodalite phase, indicating a preferred orientation of the $\{001\}$ ZIF-8 crystal planes parallel to the substrate surface. SEM images showed ZIF-8 crystals consistent with rhombic dodecahedral particles aligned along the $\langle 001 \rangle$ crys-

tal direction, confirming the OOP orientation suggested by X-ray diffraction. The authors hypothesized that the rapid coordination of Zn^{2+} released from ZnO by the HmIM ligand results in ZIF-8 crystals growing in an oriented fashion; thus, aligned ZnO nanorod-like structures could act as directing agents for the fabrication of 1D-ordered ZIF-8 films. The same method was applied to the fabrication of oriented ZIF-67 by exposing the ZnO nanorods to a methanolic solution of CoCl_2 (0.08 M), HmIM (0.16 M) and sodium formate (0.08 M) for 12 h. Next, the authors attempted to prepare oriented ZIF-8 membranes using a porous stainless steel net (SSN) as substrate. However, due to the radial distribution of ZnO nanorods on the cylindrical shape of the SSN fibers, a ZIF-8 film with preferential orientation could not be obtained. The authors used a similar method for the one-pot conversion of ZnO nanorod-modified SSN substrates to ZIF-67, by exposing the sacrificial substrates to a solution containing Co^{2+} and HmIM (vide supra) at 100°C for 12 h. When attempting this strategy, they observed a different behavior with respect to ZIF-8: ZIF-67 exhibited OOP alignment. The orientation was explained by an "in situ seeding" process. In this process, the aligned ZnO nanorods gradually dissolve and release Zn^{2+} during solvothermal growth, which are coordinated by mIM⁻ forming primitive ZIF-8 particles anchored on the SSNs. These particles act as nucleation sites for ZIF-67 crystal growth. A time-resolved study including XRD, SEM and EDS measurements, showed the appearance of an initial ZIF-8 phase, which gradually decreases while ZIF-67 increases until the pure phase is reached, supporting this hypothesis. Furthermore, the intensity of the (002) reflection was observed to increase compared to the typical dominant (011) peak in bulk ZIF-8 until a preferred orientation was reached after 12 h. The authors explained the MOF growth process by using the Van der Drift model:^[120] laterally neighboring ZIF-67 crystals overgrow each other along the fastest growth direction of $\langle 001 \rangle$ forming a top layer of OOP-1D-oriented crystals.

A direct growth technique of oriented Zn_2bIm_4 membranes ($\text{HbIm} = \text{benzimidazole}$) using ZnO coated $\alpha\text{-Al}_2\text{O}_3$ porous tubes as substrate and ammonium hydroxide as a crystal growth modulator was presented by Zhang and co-workers.^[212] Initially, the ceramic substrate was placed in a solution of HbIm (1.0 M), NH_4OH (1.0 M), methanol (45 M) and toluene (45 M). After 30 min at 60°C , nucleation sites were generated on the ZnO nanoparticle layer. An intermediate washing step with methanol was found to be critical after this activation to remove MOF deposits with differently oriented crystallographic planes and prevent multidirectional growth. In the second growth step, a temperature of 100°C was then applied between 1 and 5 h to form continuous ZIF membranes with a thickness of 50 to 450 nm, respectively. In this step, the authors show that an ammonia concentration above 0.5 M is required to form 1D-oriented films. At lower concentration, tetrahedral ZIF crystals form deposited on the ZnO -modified substrate; the related X-ray diffraction pattern can be ascribed to randomly oriented crystals. However, at ammonia concentrations between 0.5 to 1.0 M , multilamellar nanosheets were observed to form on the substrate resulting in a homogenous MOF film. XRD measurements show that the MOF nanosheet film has a preferential OOP orientation along the $\langle 002 \rangle$ direction. This fabrication technique allows the deposition of 1D-oriented MOF films on porous substrates of any size.

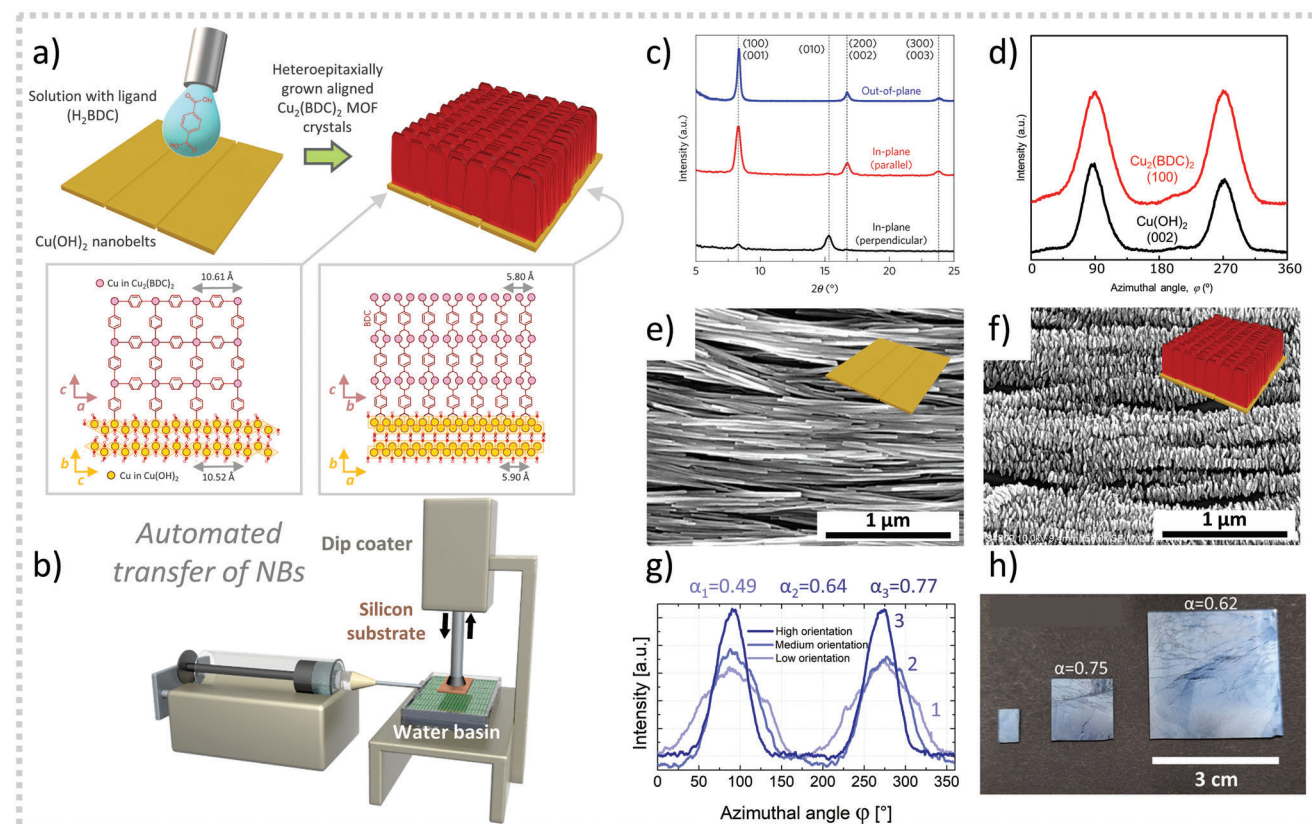


Figure 10. Ceramic-to-MOF conversion from $\text{Cu}(\text{OH})_2$ substrates to oriented Cu-MOF films. (a) Schematics of $\text{Cu}(\text{OH})_2$ nanobelt substrate transformation to $\text{Cu}_2\text{(BDC)}_2$ MOF after exposure to a solution containing the ligand (H_2BDC), insets show the epitaxial matching between the lattice of $\text{Cu}(\text{OH})_2$ and the MOF. (b) Schematic of the automated transfer setup for the fabrication of oriented $\text{Cu}(\text{OH})_2$ nanobelt substrates. (c) XRD measurements performed in OOP and IP configurations for the $\text{Cu}_2\text{(BDC)}_2$ MOF, (d) Azimuthal profile of the intensity of the (100) MOF and (002) $\text{Cu}(\text{OH})_2$ NB reflections, showing the successful heteroepitaxy and 3D-orientation. (e),(f) SEM images of the NB substrate before and after conversion to the MOF. (g) Azimuthal profile for the (100) $\text{Cu}_2\text{(BDC)}_2$ peak of three films obtained from NBs with different orientation degrees, corresponding to $\alpha = 0.49$, $\alpha = 0.64$ and $\alpha = 0.77$. (g) Scaling up of substrate size allowed by the automatic method shown in (b). Images (a),(c)-(f) adapted with permission.^[44] Copyright 2017, Springer Nature. Images (b), (g), (h) reproduced under terms of the CC-BY-NC 4.0 license.^[220] Copyright 2021, The Authors, published by John Wiley and Sons.

In 2016, Ameloot and co-workers^[112] reported the successful application of the chemical vapor deposition (CVD) technique to convert ZnO into uniform ZIF-8 films with controlled thickness. Atomic layer deposition (ALD) was used to deposit precursor ZnO films with thickness in the range 3–15 nm, which were then transformed to ZIF-8 by exposing them to HmIM vapour at 100°C for 30 min. The method allowed the deposition of homogeneous ZIF-8 films (thicknesses between 52 nm and 124 nm and low average roughness ca. 25 nm) on flat silicon substrates; however, the same approach can be used to coat high-aspect ratio silicon and PDMS pillars. This solvent-free method is compatible with existing microfabrication infrastructure and manufacturing protocols.^[213,112,214] More recently, the authors showed that the randomly oriented ZIF-8 films prepared via gas phase could be oriented.^[215] In this work, the authors deposited ZnO precursor layers by ALD with different thicknesses (ca. 1–10 nm) and densities (4.6 g cm⁻³ and 5.2 g cm⁻³). From these starting materials, they used the MOF-CVD method to convert them to ZIF-8 films with varying conversion times, and studied the samples by grazing incidence X-ray diffraction (GIXRD). The authors found that by converting thinner and lower density ZnO films,

they could obtain a preferential (100) 1D-orientation OOP, while thicker and denser ZnO films resulted in a broad preferential (111) 1D-orientation OOP.^[215] Thus, by controlling the properties of the sacrificial ZnO layer, the authors were able to obtain 1D-oriented ZIF-8 films by MOF-CVD. We note that such MOF-CVD conversion techniques have also been successfully applied for the growth of 1D-oriented Cu-MOF polycrystalline films, by conversion of Cu and CuO layers.^[216]

4.3. Ceramic-to-MOF conversion from $\text{Cu}(\text{OH})_2$ substrates

In 2016, Falcaro, Takahashi and co-workers explored the use of $\text{Cu}(\text{OH})_2$ as feedstock material for the growth of MOFs.^[44] $\text{Cu}(\text{OH})_2$ nanostructures (nanotubes and nanobelts) were exposed to an ethanolic solution of H_2BDC (Figure 10a). The authors found that $\text{Cu}(\text{OH})_2$ crystals were acting as a templating agent for the oriented growth of $\text{Cu}_2\text{(BDC)}_2$ MOFs. The oriented growth was attributed to the matching between the crystal lattice of the $\text{Cu}(\text{OH})_2$ and $\text{Cu}_2\text{(BDC)}_2$ (heteroepitaxial conditions), considering that the a and c parameters of the $\text{Cu}(\text{OH})_2$ nanobelts

($a = 2.95 \text{ \AA}$, $b = 10.59 \text{ \AA}$, $c = 5.26 \text{ \AA}$)^[217] match within 99.1% the a and b parameters of the copper paddle-wheel MOF Cu_2BDC_2 ($a = 10.61 \text{ \AA}$, $b = 5.8 \text{ \AA}$, $c = 10.61 \text{ \AA}$)^[44] (Figure 10a). Initially, a film of aligned $\text{Cu}(\text{OH})_2$ nanobelts was deposited onto a silicon substrate. In this configuration, the (020) plane of $\text{Cu}(\text{OH})_2$ nanobelts aligns parallel to the substrate (i.e., preferred IP alignment), as confirmed by the XRD azimuthal profiles (Figure 10d). Next, the films of aligned $\text{Cu}(\text{OH})_2$ nanobelts were immersed in a solution of H_2BDC (4.65 mM) prepared in a mixture of EtOH (9.34 mL) and H_2O (3.6 mL) to yield Cu_2BDC_2 MOF coatings. Within 5 min at room temperature, $\text{Cu}_2(\text{BDC})_2$ crystals were observed to grow perpendicular to the nanobelts on the substrate (Figure 10d-f). OOP-XRD measurements of the resulting films showed preferential orientation of the (00l) MOF planes parallel to the substrate (Figure 10c). Azimuthal angle dependence measurements in an IP-XRD geometry revealed 1) that (h00) and (0k0) MOF crystal faces are aligned perpendicularly to each other and normal to the film surface, and 2) that the azimuthal angle intensity profile of the (100) MOF plane coincides with that of the (002) plane of the $\text{Cu}(\text{OH})_2$ substrate, indicating that the latter directs the MOF growth (Figure 10d). Thus, this study demonstrated that extended 3D-oriented Cu-based MOF films can be prepared starting from a film of aligned ceramic Cu-based nanostructures via heteroepitaxial growth in a rapid one-step fabrication process.

To expand the understanding on this process, Doonan, Huang and co-workers developed a high-throughput screening algorithm to identify MOF candidates that can undergo heteroepitaxial growth on metal-hydroxide substrates.^[218] The authors limited the search to MOFs containing copper nodes and carboxylate functional groups, where each oxygen is bound to a copper atom. The procedure was based on a three-step screening process, consisting of (1) selection of candidate MOFs based on chemistry (MOF with copper-bound carboxylate functionalities); (2) refinement of the data set based on lattice matching; and (3) ranking of MOFs by interfacial bonding. For this purpose, the authors screened MOF structures from three different databases (CORE MOF, TOBACCO and hMOF), comprising over 20 000 different tested MOF structures. For the lattice matching, a high mismatch tolerance was considered (10% supercell vectors, 2% angle mismatch, 15% maximum area mismatch), due to the flexible nature of MOFs.^[219] When considering surface chemical compatibility, substrate-MOF lattice matching and interfacial bonding, the screening of the multiple MOF databases revealed that the best candidates for the heteroepitaxial growth on aligned copper hydroxide substrates are composed mostly of MOFs with rectangular lattice symmetry in the plane of the substrate. It was found that the rectangular symmetry of the $\text{Cu}(\text{OH})_2$ (010) plane preferentially selects MOFs with at least one Miller plane with rectangular symmetry, which is also consistent with experimental data. This finding highlights a substrate-directing effect, wherein the substrate surface's symmetry dictates the symmetry of the MOF binding sites, consequently influencing the orientation of the MOF binding plane.

The degree of orientation and the size of the resulting MOF films thereby depend almost exclusively on the orientation of the $\text{Cu}(\text{OH})_2$ substrate. In order to overcome the limitations of the originally reported manual deposition procedure of $\text{Cu}(\text{OH})_2$ nanobelts, Linares et al. recently implemented a semi-automatic

deposition procedure.^[220] By using a dip-coater setup, deposition conditions are described for the consistent fabrication of high-quality oriented $\text{Cu}(\text{OH})_2$ films (Figure 10b). For this, different deposition parameters were studied: the film homogeneity and orientation of the resulting samples were optimized. The film homogeneity was described as the percentage of the substrate fully coated by the films (coverage%). The order of the nanobelt film was described by the orientation parameter defined as $\alpha = 1 - \text{FWHM } \pi^{-1}$, where FWHM is the full width at half-maximum (radians) of the azimuthal profile corresponding to the (002) plane of $\text{Cu}(\text{OH})_2$. A value of $\alpha = 1$ represents a full, uniaxial orientation of the sample, while $\alpha = 0$ already describes a randomly oriented system (Figure 10g). Using a leveled setup, an immersion depth of 1.5 mm, an immersion speed of 10 mm s⁻¹, and 69 μL of ethanolic nanobelt dispersion injected onto a 63 × 34 mm water surface, 100% yield of $\text{Cu}(\text{OH})_2$ nanobelt films with a coverage > 99% and an orientation of $\alpha = 0.75 \pm 0.01$ was achieved. Furthermore, the substrate size could be upscaled to 10 cm² increasing the original substrate dimensions (i.e., 1 cm²).^[44] by a 10-fold (Figure 10h). This upgraded method allowed for the deposition of oriented homogeneous multilayers (up to 5 consecutive layers).

The heteroepitaxial growth approach using $\text{Cu}(\text{OH})_2$ nanobelt films as sacrificial substrates could be extended from $\text{Cu}_2(\text{BDC})_2$ to other 3D-oriented Cu-MOFs, such as $\text{Cu}_2(\text{BPDC})_2$ and $\text{Cu}_2(\text{NDC})_2$. The formation of pillar-layered MOF thin films of the type $\text{Cu}_2\text{linker}_2\text{DABCO}$ (linker = H_2BDC , H_2BPDC , H_2NDC ; DABCO = 1,4-diazabicyclo[2.2.2]octane) grown from $\text{Cu}(\text{OH})_2$ nanobelt substrates was investigated by Okada, Takahashi and coworkers.^[53] The authors found that the direction of the unidimensional nanopore channels created by the square-shaped arrangement of the linkers in the pillared MOFs can be controlled through the linker:DABCO molar ratio (Figure 11a). Under linker-rich conditions (e.g., linker:DABCO = 4:1; linker = 16 mM, DABCO = 4 mM), the carboxylic acid functional groups of the linker lowered the pH to acidic (pH 4) resulting in the gradual dissolution of $\text{Cu}(\text{OH})_2$. The released Cu^{2+} ions yield two-dimensional MOF sheets of the type $\text{Cu}_2\text{linker}_2$, which grow perpendicular to the substrate surface (OOP) via the pillar DABCO ligand (Figure 11d). MOF films prepared following this "dissolution and precipitation" mechanism, show intense diffraction peaks associated to the (00l) planes in OOP XRD measurements (1D-orientation OOP, see Figure 11b,d), but lack azimuthal angle dependence in the (h00) and (0k0) intensity profiles, measured by IP-XRD. The rapid dissolution of the $\text{Cu}(\text{OH})_2$ causes a loss of the epitaxial relationship between the $\text{Cu}(\text{OH})_2$ nanobelt film and the nascent MOF layer, resulting in OOP monodirectional pore channels that are formed, perpendicular to the substrate surface. On the other hand, at low linker:DABCO molar ratios (e.g., linker:DABCO = 1:64; linker = 16 mM, DABCO = 1024 mM; pH 9), $\text{Cu}(\text{OH})_2$ is stable and the surface-located "Cu-OH" moieties afford epitaxial growth of the MOF (Figure 11c,e). Films grown under these conditions show a clear 3D-orientation, demonstrated by an intense (0k0) diffraction signal in OOP-XRD measurements and distinct IP-angular dependence for the (h00) and (00l) faces of the MOF crystals confirming the epitaxial growth mechanism (Figure 11c). Due to the growth parallel to the substrate via the pillar ligand, DABCO, the nanochannels are also IP-oriented, parallel to the substrate surface. The authors showed that these findings were independent of the carboxylate

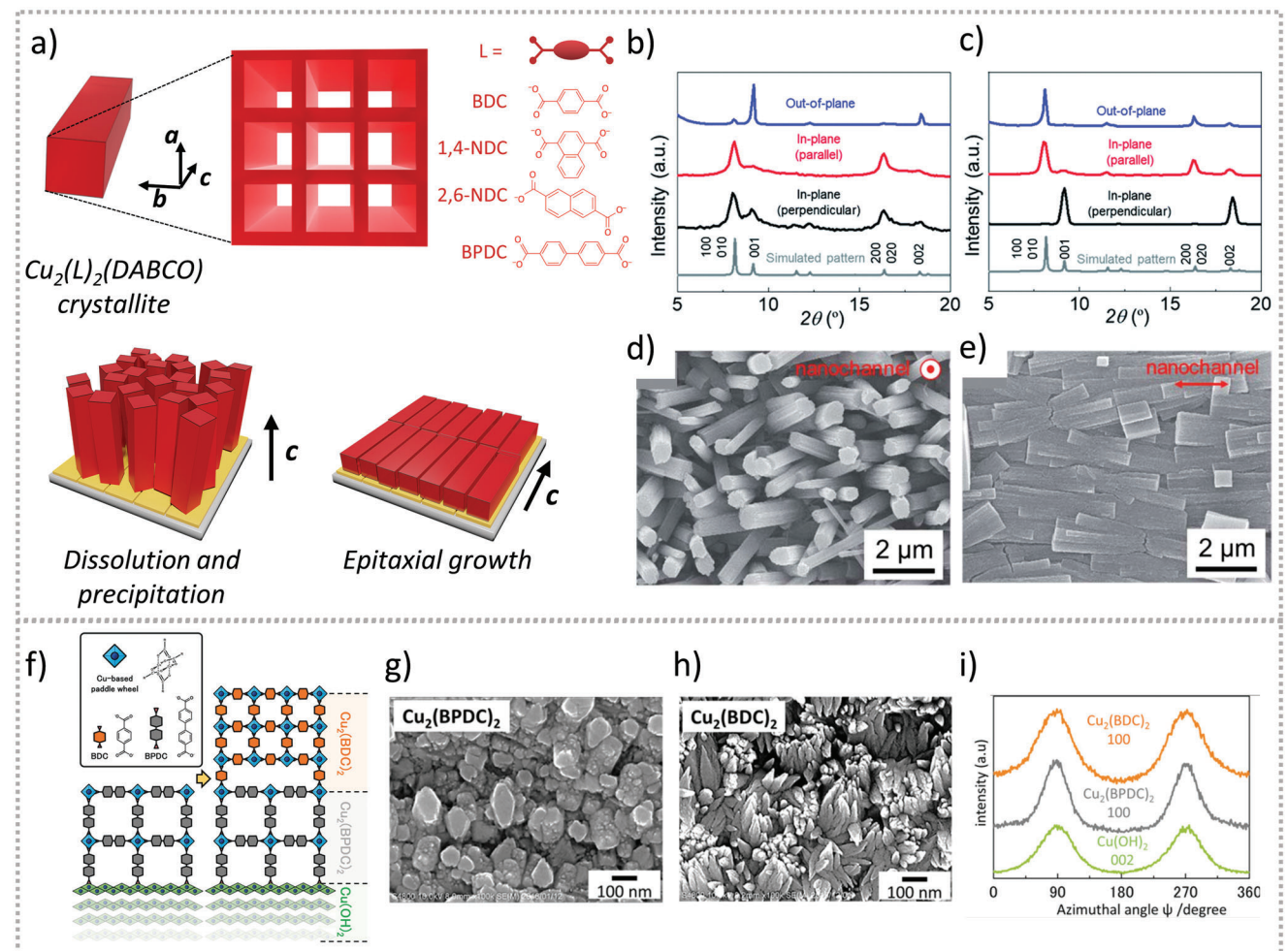


Figure 11. Ceramic-to-MOF conversion from $\text{Cu}(\text{OH})_2$ substrates to oriented Cu-MOF films. (a) Schematic of the growth of $\text{Cu}_2(\text{L})_2\text{DABCO}$ pillar-layered MOFs in two different conditions: dissolution and precipitation, and epitaxial growth. XRD characterization by out-of-plane and in-plane measurements for samples obtained with the dissolution and precipitation method (b) and with the epitaxial growth (c). (d) Top view SEM image corresponding to (b). (e) Top view SEM image corresponding to (c). Images reproduced under terms of the CC-BY-NC 4.0 license.^[53] Copyright 2020, The Authors, published by Royal Society of Chemistry. (f) Lattice matching between two different Cu-MOFs, $\text{Cu}_2(\text{BDC})_2$ and $\text{Cu}_2(\text{BPDC})_2$, grown on $\text{Cu}(\text{OH})_2$ nanobelts using a MOF-on-MOF strategy. (g) Top view SEM of the first MOF grown on the NBs, $\text{Cu}_2(\text{BPDC})_2$. (h) Top view SEM of the second layer MOF $\text{Cu}_2(\text{BDC})_2$, grown on (g). (i) Corresponding azimuthal profile of the MOF-on-MOF structure following the (100) of $\text{Cu}_2(\text{BDC})_2$ and $\text{Cu}_2(\text{BPDC})_2$, and (002) of $\text{Cu}(\text{OH})_2$ showing the heteroepitaxial growth. Images adapted with permission.^[222] Copyright 2019 John Wiley and Sons.

linker and therefore present a general concept for the orientation of monodirectional nanochannels in $\text{Cu}_2\text{linker}_2\text{DABCO}$ MOF films. These results provide insight into the ceramic-to-MOF mechanism in the case of pillar-layered MOFs and the role of the pH during the conversion reaction. Okada, Takahashi and co-workers have observed that polarized IR can also provide angle-dependent absorption spectra.^[221] Thus, vibrational modes have been directly correlated to the crystallographic orientation of the 3D-oriented MOFs, suggesting that vibrational spectroscopy could be used to probe the alignment of MOF crystals.

The potential of oriented MOF films grown from $\text{Cu}(\text{OH})_2$ nanobelt substrates was expanded to multi-layered MOF systems, typically referred as MOF-on-MOF films.^[222] In this case, the first MOF layer is prepared using the one-pot approach discussed above. Additional MOF layers are then deposited on top using the liquid phase epitaxy concept.^[81,219] Doonan, Taka-

hashi and co-workers showed the successful synthesis of 3D-oriented MOF films with up to three different MOF layers (Figure 11f). The $\text{Cu}_2(\text{NDC})_2$ -on- $\text{Cu}_2(\text{BDC})_2$ -on- $\text{Cu}_2(\text{BPDC})_2$ -on- $\text{Cu}(\text{OH})_2$ films were prepared by subsequent LbL treatments of the $\text{Cu}_2(\text{BPDC})_2$ -on- $\text{Cu}(\text{OH})_2$ MOF film alternating Cu^{2+} (1 mM) and linker (H_2BDC = 1 mM, H_2NDC = 1 mM) solutions prepared in ethanol (Figure 11g,h). The thickness of the individual layers was controlled by the number of LbL cycles, but was shown to plateau after ca. 50 cycles. The crystallinity and structural alignment of all layers was confirmed by OOP, IP, and azimuthal XRD measurements, showing that the (h00) and (0k0) faces of the three MOF layers ($\text{Cu}_2(\text{NDC})_2$, $\text{Cu}_2(\text{BPDC})_2$ and $\text{Cu}_2(\text{BDC})_2$) are aligned orthogonally to each other and perpendicularly to the $\text{Cu}(\text{OH})_2$ substrate (Figure 11i). These measurements indicate a 3D-orientation of the multilayered MOF superstructures. By applying the LbL approach, the authors also grew

3D-oriented MOFs that cannot be grown directly from Cu(OH)₂ substrates. This includes MOFs with non-copper metal nodes, such as Zn₂(BDC)₂ or Co₂(BDC)₂, which could crystallize on oriented Cu₂(BDC)₂-on-Cu(OH)₂ films. Additionally, it was demonstrated that H₂BPYDC (bipyridyl dicarboxylic acid), which does not react with Cu(OH)₂ in the one-pot approach presumably due to the metal binding interference of the bipyridine moiety, could be used to deposit a 3D-oriented Cu₂(BPYDC)₂ MOF layer on a Cu₂(BPDCl)₂-on-Cu(OH)₂ film. This study on the heteroepitaxial growth of MOFs from aligned Cu(OH)₂ nanobelts substrates followed by LbL deposition affords 3D-oriented MOF films with building blocks that would not spontaneously grow on Cu(OH)₂ nanobelts. Thus, it was possible to expand the scope of linkers and metal nodes for the synthesis of multifunctional MOF films with anisotropic properties. The MOF-on-MOF approach was combined with the immobilization of a photo-responsive guest molecule (azobenzene) into the pores of 3D-oriented MOF superstructures (Zn₂(BDC)₂DABCO/Cu₂(BDC)₂) to obtain stimuli-responsive 3D-oriented MOF films.^[223] This development highlights the potential of photo-switchable 3D-oriented MOF films for sensing, energy storage and cargo uptake and release applications.^[224,225]

4.4. From MOF positioning to microfabrication of 3D-oriented MOF patterns

The simultaneous control over particle orientation and positioning would enable the fabrication of integrated systems with enhanced electric,^[226] optical,^[63] or magnetic functional properties,^[227] to name a few. For example, in polymers, patterns of oriented crystalline semiconductors permitted the fabrication of organic field-effect transistors (OFET) with unprecedented charge-carrier mobility.^[228,229] Similarly, patterned polymers with oriented lamellar microstructures can be used in photonic crystals featuring solvatochromic response.^[230] The precise control over the location and dynamic positioning (alignment) of liquid crystalline elastomers has been used to fabricate microstructural actuators with amplified stimuli-induced mechanical response.^[231,232] Additionally, in ceramics, there are several examples of aligned patterned systems.^[233–235] These include oriented perovskite patterns that enable mechano-optical sensors and optical display fabrication.^[236] We anticipate that directional properties observed in those organic and inorganic materials can be judiciously hybridized into oriented organic-inorganic micro- and nano-patterns by using MOFs. Furthermore, the combination of micropatterning with porous materials can even enhance their functional properties.^[237–239] However, to take full advantage of the directional-dependent properties of different MOF materials, it is crucial to develop micropatterning protocols that allow the positioning of oriented MOF crystals without compromising the MOF crystals' chemical structure, orientation, and porosity.^[43,240]

In general, some MOF micropatterning protocols report the use of photolithography to control the spatial location of crystals.^[241–243] This micropatterning method is technologically appealing as it is compatible with the processes currently implemented for the fabrication of modern devices (e.g., microelectronics).^[244–247] Typical photolithography processes re-

quire a light-sensitive material (e.g., polymer resins) that undergoes a solubility change after the exposure of selected areas to radiation with specific wavelengths. When the proper radiation dose is used and an optimized etching protocol is designed (i.e., choice of the etching solution, time, and temperature), the contrast between the insoluble and the soluble areas affords the fabrication of well-defined patterns.^[15,43,248] The implementation of resist-based photolithography with MOFs has been conducted by using mainly two distinct approaches^[43]: the deposition of a MOF film first and a photoresist layer after (here the patterned resist is used to expose selectively MOF areas to MOF etching solution)^[242] and the deposition of a photoresist first as a primer to immobilize MOF crystals (here the photoresist is dissolved to release the MOF crystals from selected areas).^[19] However, the use of resist-based lithography for the micropatterning of porous materials, such as MOFs, could lead to structural decomposition of the porous material during the resist removal and/or pore blockage caused by resist contamination.^[249–252]

To overcome these issues, Ameloot and co-workers reported a resist-free photolithography strategy for micropatterning films of zeolitic imidazolate frameworks comprised of halogenated organic linkers based on the use of deep X-ray lithography and e-beam lithography.^[252] Using X-ray photoelectron spectroscopy (XPS), the authors observed that the photoelectrons generated upon X-ray exposure induce the homolytic cleavage of the C–X bond (X = Cl or Br). The radical species generated trigger the chemical decomposition and solubility switch of the exposed areas, which can be easily removed via dimethylsulfoxide (DMSO) dissolution. Thus, the authors demonstrated that the halogen substituent of the organic linker imparts sensitivity to the MOF film towards X-rays. The radiation-induced solubility switch allows for using the MOF film as a positive tone resist for the direct lithography of MOF films with halogen functionalization (e.g., ZIF-71). This resist-free lithography technique was used to pattern films of ZIF-71 with excellent sub-50-nm resolution. The authors explored the application of these porous ZIF-71 micropatterns as a responsive diffraction grating for methanol vapour sensing. When a 650 nm laser illuminates these samples, diffraction patterns with red spots can be observed. Then, the exposure of the MOF pattern to organic vapours causes a change in the refractive index: this results in changes in the red diffraction pattern, which can be easily monitored with a camera.^[252] This contribution represents an important step towards integrating MOFs into miniaturized devices.

The implementation of patterning techniques into oriented MOF films represents a significant milestone for the fabrication of next-generation devices. The spatial localization of aligned pore channels in selected areas engenders the possibility of controlling the collective anisotropic properties that emerge from the preferential crystalline orientation at micro- or nano-meter scales (i.e., spatially defined two-dimensional MOF superstructures).^[43] In this context, it is worth noting that the ceramic-to-MOF strategy has been applied to the fabrication of MOF patterns of mostly disordered MOF superstructures.^[104,112,213,241,253,254] Considering that well-established technologies are already available for thin film deposition and lithography of ceramics, the transformation of pre-patterned ceramic substrates to MOFs provides a simple bottom-up approach for the fabrication of MOF micropatterns.

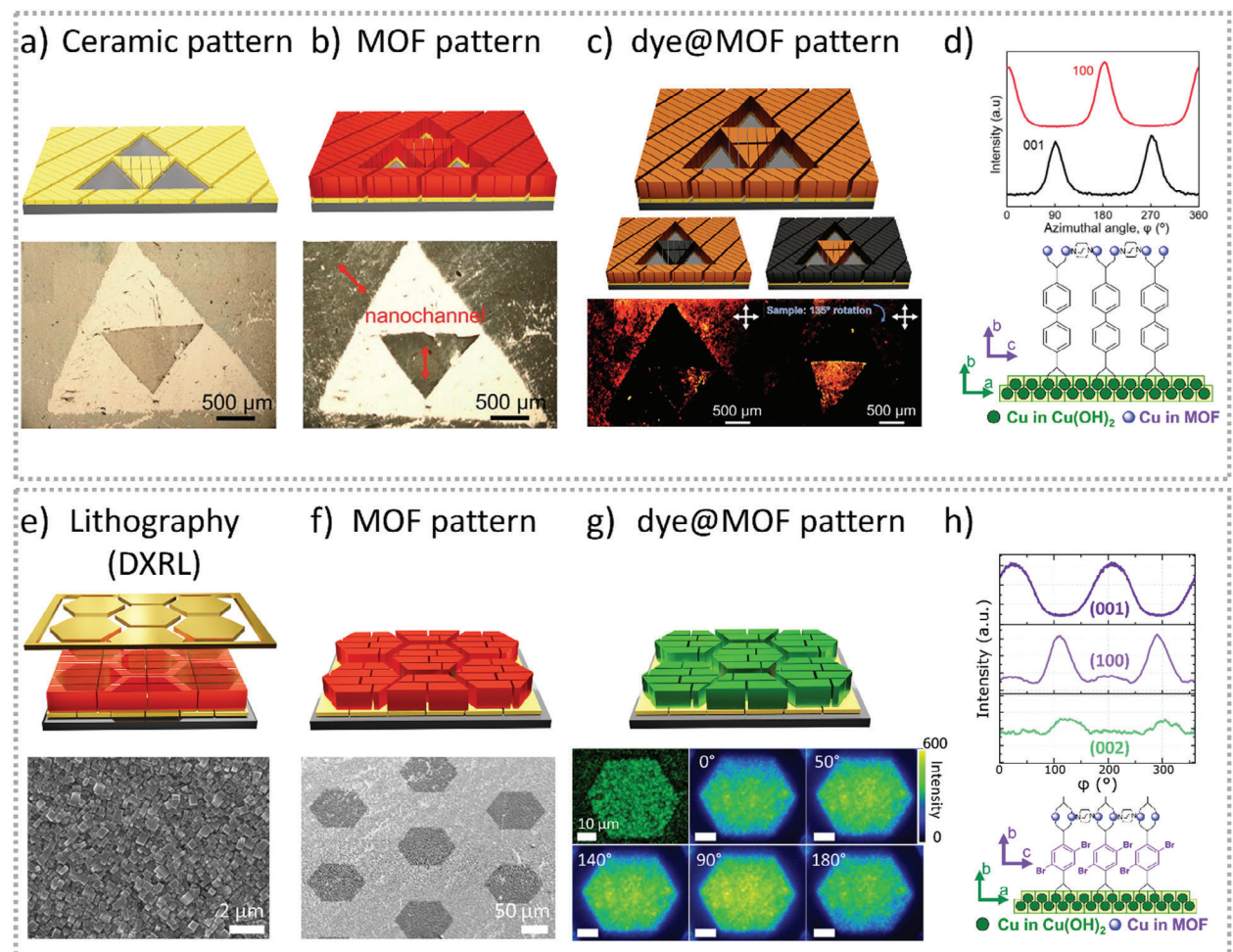


Figure 12. Bottom-up and top-down patterning approaches for the fabrication of oriented MOF patterns. (a) Schematic representation and optical image of an oriented $\text{Cu}(\text{OH})_2$ nanobelt pattern. (b) Schematic representation and optical image of the oriented MOF pattern obtained from the ceramic to MOF transformation into $\text{Cu}_2(\text{BPDC})_2\text{DABCO}$. (c) Schematic representation and polarization optical microscope image of the oriented AZB@MOF pattern collected at the same position as that of the optical microscope image (left panel) and after rotating the sample 135° clockwise (right panel). (d) Azimuthal angle dependence of intensity profiles of (100) and (001) crystallographic planes corresponding to a $\text{Cu}_2(\text{BPDC})_2\text{DABCO}$ MOF with 3D-orientation obtained from aligned $\text{Cu}(\text{OH})_2$ NBs. Images (a)-(d) reproduced under terms of the CC-BY-NC 4.0 license.^[53] Copyright 2020, The Authors, published by Royal Society of Chemistry. (e) Scheme illustrating the resist-free patterning of oriented MOF films, where the MOF film is exposed to deep X-rays through a lithography mask (upper panel). SEM image of the oriented MOF film B94 (lower panel). (f) MOF patterns obtained after the selective dissolution of the exposed areas; SEM of the hexagonal micrometric patterns obtained by DXRL. (g) Schematic illustration and CLSM image of the fluorescent patterns of BPY@B94 (upper panel). Fluorescence microscopy images were obtained by rotating the polarization of the excitation laser (lower panel). (h) Azimuthal angle dependence of intensity profiles of the (100) and (001) reflections of the oriented MOF film B94, and the reflection (002) of the aligned $\text{Cu}(\text{OH})_2$ NBs used as sacrificial template. Images (e)-(h) reproduced under terms of the CC-BY 4.0 license.^[45] Copyright 2023, The Authors, published by John Wiley and Sons.

For example, Okada et al. have used $\text{Cu}(\text{OH})_2$ nanotubes grown from pre-patterned Cu substrates (e.g., printed electronic circuit board) for the subsequent conversion into HKUST-1 micropatterns.^[241] Another example is the use of pre-patterned ZnO substrates to obtain ZIF-8 patterns with a resolution of tens of microns by a solvent-free conversion, reported by Ameloot and co-workers.^[213] These methods typically afford 0D- or, in some cases, 1D-oriented MOF micropatterns. Thus, the combination of the ceramic-to-MOF transformation with heteroepitaxial growth from oriented anisotropic ceramic substrates (see Section 4.3), would be an ideal next step towards 3D-oriented MOF micropatterns.

Currently, methods for fabricating 3D-oriented MOF patterns are still in their infancy.^[240] In this direction, Okada et al. recently reported the fabrication of millimetre-scale patterns of 3D-oriented Cu-based MOF crystals (Figure 12).^[53] The spatial control over the MOF growth was achieved following a bottom-up approach, i.e., using a pre-patterned ceramic as metal feedstock for confining the MOF crystal growth in predefined locations (vide supra). Specifically, the authors used a patterned coating of $\text{Cu}(\text{OH})_2$ NBs as a sacrificial template for the heteroepitaxial growth of $\text{Cu}_2(\text{BPDC})_2\text{DABCO}$ crystals (Figure 12a). The $\text{Cu}(\text{OH})_2$ pattern was obtained by using the scotch tape technique,^[255] where the deposition of $\text{Cu}(\text{OH})_2$ was

accomplished in two steps: 1) Deposition of the smaller triangle where the outside region of the triangle was covered with scotch tape; 2) deposition on the outside of the larger triangle where the inside was covered with scotch tape. The alignment direction of the pre-deposited $\text{Cu}(\text{OH})_2$ NBs in both substrate regions, i.e., outside of the large triangle and inside of the smaller triangle differs by 45° (Figure 12a). That is, the longitudinal direction of the $\text{Cu}(\text{OH})_2$ NBs deposited in the outside region of the large triangle aligns in a diagonal line from upper left to lower right, whereas for the $\text{Cu}(\text{OH})_2$ NB deposited inside of the small triangle aligns in a vertical line. The pre-patterned $\text{Cu}(\text{OH})_2$ NB substrate was immersed in a methanolic solution of H_2BPDC (4 mM), DABCO (256 mM), and acetic acid (35 mM) at 60° for 3 h. The latter results in the heteroepitaxial growth of $\text{Cu}_2(\text{BPDC})_2$ -DABCO crystals, with 3D-orientation, exclusively in the regions where the $\text{Cu}(\text{OH})_2$ NBs were pre-deposited (Figure 12b). The orientation of the aligned $\text{Cu}(\text{OH})_2$ NBs dictates the orientation of the $\text{Cu}_2(\text{BPDC})_2$ -DABCO crystals and, consequently, the direction of the nanochannels of the MOF network. The macroscopically aligned monodirectional nanochannel arrays can be used to accommodate guest molecules in an oriented manner granting access to the anisotropic properties of the MOF crystals. To prove this concept, the authors infiltrated a dye molecule, trans azo-benzene (AZB), within the channels of the oriented MOF crystals (Figure 12c). The integration of guest molecules within the pore network was achieved by exposing the oriented MOF patterns to AZB vapors.^[256] Then, the researchers ascertained the alignment of AZB molecules by monitoring the polarization-dependent UV-Vis absorption. In this test, the polarization of the incident light was rotated every 15° , and strong absorption at 360 nm was observed when the light polarization was parallel to the direction of the nanochannels in the oriented MOF crystals. This polarization-dependent absorption was not observed in poorly oriented films. This study shows that by combining the ceramic-to-MOF conversion with the bottom-up patterning method, it is possible to control the direction of macroscopically aligned nanochannel arrays at specific locations on the same substrate (Figure 12c). This proof-of-concept enabled the confinement of the ON-OFF response of the AZB@MOF crystals, with 3D-orientation (Figure 12d), within millimeter scale areas of the substrate.

The integration of MOFs into miniaturized devices demands an improved resolution of the 3D-oriented patterns (micro- or nano-patterns). To improve the resolution of 3D-oriented MOF patterns, Velásquez, Linares, et al. implemented a resist-free deep X-ray lithography method for the top-down micropatterning of 3D-oriented MOF films (Figure 12e).^[45] In this study, the authors combined the heteroepitaxial ceramic-to-MOF conversion approach^[44] with a mixed-linker strategy^[257] to design a resist-free patternable 3D-oriented MOF film (Figure 12f). Specifically, $\text{Cu}(\text{OH})_2$ nanobelts were exposed to a mixture of H_2BDC and its halogenated counterpart (i.e., $\text{H}_2\text{Br}_2\text{BDC}$) and DABCO yielding the heteroepitaxial growth of an oriented Cu-based MOF film with nominal formula $\text{Cu}_2[(\text{Br}_2\text{BDC})_x(\text{BDC})_{100-x}]_2$ -DABCO. Inspired by the previous report from Ameloot and co-workers^[252], the authors envisioned that integrating the brominated dicarboxylic ligand ($\text{H}_2\text{Br}_2\text{BDC}$) in the reticular network would provide sensitivity to the MOF coating towards the X-ray radiation while keeping the preferential 3D crystalline orientation.^[44] The

authors found that the non-brominated MOF ($x = 0$) possessed low sensitivity to the X-rays, while a fully brominated Cu-MOF ($x = 100$) did not afford homogeneous coatings. In contrast, samples prepared with 94% $\text{H}_2\text{Br}_2\text{BDC}$ ($x = 94$, **B94**) afforded homogeneous and 3D-oriented polycrystalline films. Thus, the use of a mixed-linker strategy previously used for SURMOFs^[257] enabled the synthesis of radiation-sensitive homogeneous oriented coatings. The ceramic-to-MOF conversion for **B94** was carried out by immersing a film of aligned $\text{Cu}(\text{OH})_2$ NBs into a methanolic mixture of DABCO (26.74 mM), $\text{H}_2\text{Br}_2\text{BDC}$ (6.22 mM), and H_2BDC (0.42 mM) at 70°C for 1 h. The preferential orientation of the MOF crystals was evaluated by the OOP-XRD and IP-XRD azimuthal profile analysis of the MOF films. The OOP-XRD pattern of sample **B94** exhibits an intense diffraction peak at $2\theta = 8.2^\circ$ ascribed to the (010) planes, while the peak associated with the (001) planes is essentially absent. This result suggested that the MOF crystals exhibit preferential IP orientation, and thus 3D-orientation. To confirm the epitaxial relationship between the $\text{Cu}(\text{OH})_2$ substrate and the MOF crystals, the authors investigated the azimuthal angle dependence in the intensity profiles of the (002) reflection from $\text{Cu}(\text{OH})_2$ and the (100) and (001) reflections of the MOF film. The azimuthal scan profiles evidenced that the two maxima of the MOF planes (100) match the maxima of the (002) reflection of the $\text{Cu}(\text{OH})_2$ NBs (Figure 12h). This observation confirms the heteroepitaxial growth of the mixed-linker 3D-oriented MOF crystals, where the pore nanochannels are oriented parallel to the substrate surface.^[53] The X-ray sensitivity of the 3D-oriented MOF film **B94** was examined by exposing samples to different X-ray doses, and monitoring the chemical and structural changes by FT-IR spectroscopy and XRD (dose matrix analysis). This analysis was used to determine the surface radiation dose (1748 J cm^{-2}) required to induce a sufficient MOF decomposition and the solubility switch of the exposed regions. Thus, upon exposing the **B94** film to deep X-rays under a photomask, the MOF undergoes chemical and structural changes that allow for the selective dissolution of the exposed areas in a mixture of $\text{MeOH}/\text{H}_2\text{O}/\text{AcOH}$. This top-down approach enables the patterning of large areas of MOF films with micron-level resolution (Figure 12f). Remarkably, the quality of the micropatterns is evidenced by their ability to produce clear optical diffraction patterns upon illumination with a 650 nm laser, both in transmission and reflection configuration.^[45] Finally, the authors integrated a fluorescent dye (BODIPY) within the oriented pore channels of the MOF crystals to investigate the anisotropic photonic response of the aligned dye molecules in the 3D-oriented MOF patterns (Figure 12g). The analysis demonstrated that the alignment of the dye molecules within the pores engenders a spatially controlled anisotropic fluorescent response when rotating the polarization angle of the excitation laser (Figure 12g). This approach highlights how implementing micropatterning techniques to oriented MOF films with anisotropic physical properties could progress the integration of MOFs into miniaturized switchable photonic devices.

4.5. Conclusions and Perspectives

Compared to other methods, the heteroepitaxial growth of oriented MOF films from ceramic substrates has several advantages

for scalability: methods to align 1D-nanoobjects, such as nanorods, nanobelts, nanowires and nanofibers are well-established,^[258] thus, the oriented ceramic films can be prepared with different approaches; the fabrication and ceramic-to-MOF conversion occurs rapidly at moderate temperatures; the resulting 3D-oriented crystalline domains are in the centimeter scale. However, the main bottleneck of this method is its lack of versatility that can only be applied to MOFs whose crystalline structure matches that of the ceramic. So far, the heteroepitaxy approach was primarily investigated for the preparation of 3D-ordered MOF films starting from Cu(OH)₂ substrates that are converted to Cu-based MOFs. To expand the 3D-oriented MOF scope, a MOF-on-MOF approach was successfully applied.^[222,259,260] However, we note that, Cu-based MOFs could be used as a template only for other MOFs that can be prepared under mild synthetic conditions. Advances in expanding the direct heteroepitaxial transformation of ceramic-to-MOFs to chemically robust MOFs will be beneficial for the progress of 3D-oriented MOF films. We note that, at the moment, there is a limited understanding of the variables involved in the conversion process.^[53,261] In situ investigations of the ceramic-to-MOF conversion kinetics could possibly provide a know-how that could be translated to ceramic and MOF systems with different chemical compositions and properties. An additional key tool that could expedite the progress of heteroepitaxial MOFs is the computational screening of ceramic structural databases and compatible MOFs.^[218,262] We envision the expansion of this study towards other ceramics could expand the scope of 3D-oriented MOFs that can be grown with this approach.

The fabrication of oriented MOF micropatterns provides direct control over the spatial localization of the anisotropic properties of the MOF crystals at the micrometre scale. However, to date, only a few examples of success have been reported, leaving substantial room to explore new protocols: at the moment, the fabrication of high-resolution 3D-oriented patterns requires a synchrotron facility. For example, developing photochemically degradable oriented MOFs in the UV spectral region or micro-contact printing protocols for the deposition of oriented Cu(OH)₂ nanobelts will enable the preparation of oriented patterned MOF systems by different research laboratories. Additionally, by testing the integration of 3D-oriented patterns with other MOFs would help in understanding the versatility of the system towards the fabrication of multi MOF-based devices.

5. New methods

In this section, we will discuss emerging promising methods for the fabrication of 3D-oriented MOF superstructures. These methods showcase new synthetic approaches and could pave new ways for the preparation of 3D-oriented superstructures.

Medina, Bein and co-workers demonstrated that MOF films with both OOP and IP preferential orientation can be prepared by using a vapor-assisted synthesis (Figure 13a).^[263,264] The vapor-assisted conversion (VAC) method relies on the deposition of a precursor solution layer on a substrate and the subsequent exposure to a vapor source in a closed vessel at a controlled temperature.^[264] By using this method, the authors demonstrated the growth of 1D-oriented Zr-MOF films of the UiO and PIZOF families (UiO-66, UiO-66(NH₂), UiO-67, UiO-68 (NH₂)

and PPPP-PIZOF).^[264] This method was further explored for the deposition of MOF-74(M) films (M = Zn²⁺, Mg²⁺, Ni²⁺, Co²⁺) with controlled orientation. A precursor solution was prepared by dissolving the ligand 2,5-dihydroxyterephthalic acid, the metal salt and benzoic acid as modulator (in some cases) in different DMF/EtOH/H₂O solvent mixtures; the precursor solution (50–100 µL) was cast on a substrate (gold, glass, quartz or silicon) arranged horizontally near the top of a closed vessel. For the VAC process, at the bottom of the closed vessel, a DMF/EtOH/H₂O solvent mixture was added. The sealed vessel was kept at 100°C for 18 h. Under these conditions, ca. 500 nm thick films of MOF-74 were obtained. The versatility was proven by preparing different MOF-74 with different metal nodes (M = Zn²⁺, Mg²⁺, Ni²⁺, Co²⁺). The authors then used 2D grazing-incidence wide-angle scattering (GIWAXS) to determine the orientation of the resulting films. The authors found that the crystals of MOF-74(Zn), space group R-3^[265,266], were preferentially aligned along the crystallographic axis (c-axis parallel to the substrate). The combination of top-view and cross-sectional SEM images with the data collected by 2D GIWAXS on different regions of the sample suggests that this method is suitable for the fabrication of 3D-oriented MOF polycrystalline films (Figure 13b). However, to examine the macroscopic alignment of the MOF crystals, the films should be studied with a textural analysis (e.g., polar figures or azimuthal scan, *vide supra*).

3D-oriented MOF superstructures can also be obtained via a heteroepitaxial MOF-to-MOF transformation (Figure 13c). The first example of the formation of a 3D-oriented three-dimensional superstructure from a different MOF single crystal was reported by Shao et al.^[267] In this work, the authors prepared [Cu(H₂DOBDC)(H₂O)₂]ⁿ·(DMF)₂ (pristine MOF crystal, PMC) by dripping a DMF/CH₃CN/H₂O solution of Cu(OAc)₂ into a solution of 2,5-Dihydroxyterephthalic acid (H₄DOBDC), which resulted in the formation of ca. 300 µm single crystals. Immersion of the MOF crystals in methanol induced the transformation from the initial PMC to a 3D-oriented superstructure of MOF-74 nano-needles. XRD and FT-IR analysis showed that the transformation occurs via an intermediate phase (PMC-m) via removal of DMF. During a period of 14 days, XRD patterns eventually transitioned from the intermediate phase into the final MOF-74. Selected area electron diffraction (SAED) analysis of the MOF-74 shows that the nano-needles grow along the (300) planes of the PMC. The authors explained this result by suggesting a possible dissolution and heteroepitaxial recrystallization mechanism. Due to the similar crystalline lattices (mismatch < 3%) of PMC-m and MOF-74, the (100) plane of the PMC-m phase could direct the growth of the final MOF crystals as an ordered nano-needle superstructure. The 3D-orientation of the MOF-74 superstructure was then confirmed by optical means, measuring the azimuthal dependence of the intensity upon illumination of the superstructure with a collimated white light source (Figure 13d). This method revealed two intensity maxima, indicating the coherent scattering character of the aligned nano-needles. We note that in this case, the size of the 3D-oriented domains is limited to the size of the original PMC MOF crystal before heteroepitaxial MOF-to-MOF transformation.

Recently, Brandner et al. demonstrated a similar concept for the MOF-to-MOF transformation from 3D-oriented films of Cu₂(BDC)₂DABCO to 3D-oriented Cu₂(BDC)₂ (Figure 13e).^[268]

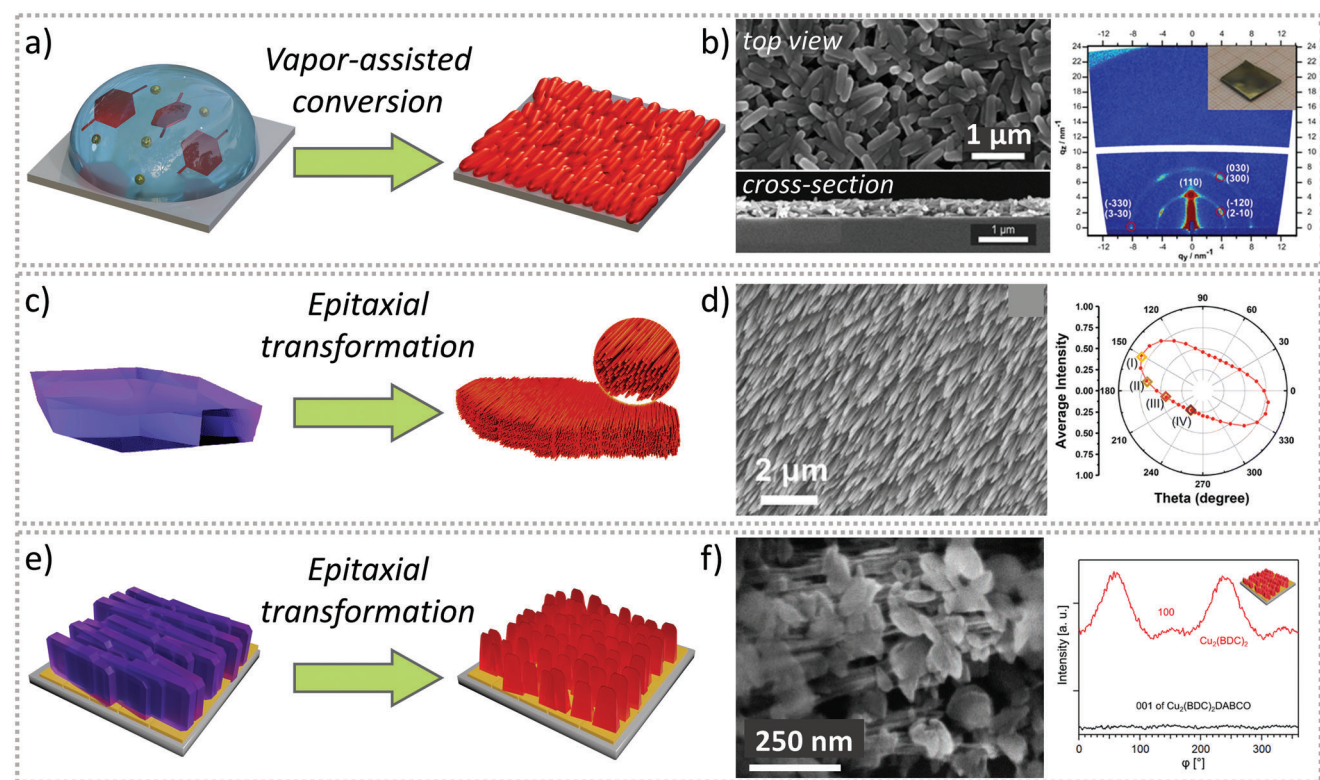


Figure 13. Schematic representation of new methods for the fabrication of 3D-oriented superstructures. (a) Vapor-assisted conversion process, (b) top view and cross-section of the IP-oriented MOF film (left) and GIWAXS measurement showing preferential orientation on the same film (right). SEM image reprinted with permission from ref.[263] Copyright 2021 American Chemical Society. (c) Epitaxial MOF-to-MOF transformation from one MOF crystal into an oriented MOF superstructure, (d) SEM micrograph of the obtained oriented MOF superstructure (left) and polar figure of refracted optical intensity showing anisotropy (right). Images adapted with permission.[267] Copyright 2023, Royal Society of Chemistry. (e) Epitaxial MOF-to-MOF transformation from a 3D-oriented superstructure into a different 3D-oriented superstructure, (f) SEM image of the transformed MOF superstructure (left), azimuthal angle dependence of IP-XRD intensity profiles of (100) and (001) reflections of the transformed MOF. Reproduced under terms of the CC-BY-NC 4.0 license.[268] Copyright 2023, The Authors, published by Royal Society of Chemistry.

The Cu₂(BDC)₂DABCO films were prepared via the heteroepitaxial growth from sacrificial Cu(OH)₂ nanostructures and exposed to different water loadings. Specifically, when films were exposed to 80% relative humidity (RH) and liquid water, SEM images displayed a change in morphology from cuboid crystals (Cu₂(BDC)₂DABCO) to smaller plate-like crystals of Cu₂(BDC)₂ (Figure 13f). After exposure to the humid environment, IR-spectroscopy revealed the absence of the DABCO pillar ligand and COO⁻ bands matched with the Cu₂(BDC)₂ phase. The authors monitored the MOF-to-MOF transformation via OOP and IP XRD. The reported IP azimuthal intensity profiles showed that the maxima of the (100) reflection of pristine Cu₂(BDC)₂DABCO coincided in position with the maxima of the (100) reflection of newly formed Cu₂(BDC)₂. Using in-situ GI-WAXS, it was noted that the MOF-to-MOF transformation occurs within a few minutes at 80% RH. The authors performed in-situ AFM measurements at 80% RH, which revealed that the morphological changes start at Cu₂(BDC)₂DABCO crystal corners, showing first terrace-like steps and subsequently ordered growth of the plate-like Cu₂(BDC)₂ crystals. The MOF-to-MOF transformation was attributed to a dissolution-recrystallization mechanism due to the high lattice matching of the two frameworks showing that the heteroepitaxial recrystallization mech-

anism can occur in both, single-crystal^[267] and polycrystalline systems.^[268]

5.1. Conclusions and Perspectives

While the previously mentioned emerging methods have demonstrated promising results in preparing oriented MOF systems, it is worth drawing inspiration from established fabrication processes that are already employed for creating in-plane oriented systems. Here, we selected three methods that could be tested in the lab without the need for specialized equipment.

5.1.1. Shearing coating method

Shearing coating method via capillary assembly^[269] typically involves the controlled movement of two flat substrates at a specified speed. In this approach, a solution containing either particles or molecular precursors is sandwiched between the substrates, and by regulating the speed, the deposition rate can be precisely adjusted. The presence of pillared structures with specific morphologies can enhance the IP alignment of crystals. This

method has been successfully used to orient particles with high aspect ratios (AR)^[269–271] or to induce the IP orientation of crystals (e.g., polythiophenes and silver nanowires) from molecular precursors.^[228,272] Recently, solution shearing has also been applied for the fabrication of MOF thin films with promising results,^[273] even showing hints of OOP-1D-orientation of the MOF crystals.^[274,275] Thus, it seems plausible that this method could be applied to solutions with pre-formed MOF crystals and/or with MOF building blocks, and optimized for the fabrication of 3D-oriented MOF superstructures, or even be combined with an additional orienting force along a secondary crystallographic direction.

5.1.2. Templatated substrates

Another unexplored method with MOFs is the assembly by templatated substrates. These substrates are typically templatated by patterns (e.g., embossed channels or wrinkles) that are used to selectively constrain the deposition of particles with high AR to specific orientations in selected areas.^[276] The substrates are exposed to suspensions of the particles that will accommodate within the patterns while those outside the channels will be removed by subsequent washing. By matching the size of the channel with those of the high aspect ratio particles, IP aligned Au and CdSe nanowires were obtained.^[277,278] When considering MOF crystals, typically in the micrometer range, the fabrication of microchannels that could fit the MOF particle size distribution seems an affordable and versatile strategy.

We note that excellent results in both positioning and aligned nanocrystals have been obtained by combining shearing methods with templatated substrates as nanocrystals can be preferentially deposited on patterns with customized shapes.^[269]

5.1.3. Strain deformation

Another method that has been widely explored with polymers and their composites, as well as other inorganic materials, is the application of strain to induce IP alignment.^[279] The concept has been successfully applied for the alignment of particles with high AR. Silver, Silicon, ZnO, and PbZr_{0.2}Ti_{0.8}O₃ nanowires have been deposited on an elastomeric substrate; by temporarily stretching the polymer along a specific direction, the angular distribution of the nanowires changes: the nanowires align along the direction of deformation of the polymer.^[280–283] Subsequently, the aligned anisometric superstructure can be transferred to a different substrate via contact printing.^[279]

While contact printing has been used to prepare patterns of randomly oriented MOF crystals, to date, the transfer of mechanically stable, oriented MOF superstructures has yet to be reported.

Other methods to orient nanostructures have been shown for different materials that have not been included in this perspective:^[284–286] we encourage the readers to be inspired by these developments to bring progress to the field of oriented MOF superstructures.

6. Conclusions and outlook

When comparing the emerging methods suitable for the fabrication of 3D-oriented MOF superstructures, we can identify com-

mon major challenges. The first is the need for precise control over the morphology and size of the MOF crystals. Both the assembly and the external-field methods (**Section 2** and **3** respectively) are based on the assembly of pre-synthesized MOF particles into oriented MOF superstructures. For the assembly method, the monodispersity of the MOF particle size is an important parameter to afford large 3D-oriented domains, indeed dimensional variations in particle size result in highly defective or disordered superstructures. External field-assisted methods necessitate MOF particles with a high degree of anisometry to generate a robust response (i.e., torque) to magnetic or electric fields, resulting in well-oriented domains. In the case of heteroepitaxial growth of MOFs from ceramics (**Section 4**), the resultant MOF film homogeneity and roughness depend on the control over the morphology of the constituent crystals. Thus, progress with the development of knowledge and methods for precise control over the MOF particle size (size and size distribution) and morphology (shape, aspect-ratio)^[287–290] will benefit all methods dealing with the fabrication of oriented MOF superstructures.

Another intrinsic problem of MOF superstructures is their stability; this could be split into two components: 1) the intrinsic chemical and structural stability of the constituent MOF particles (intraparticle stability) and 2) the mechanical stability of the superstructure (interparticle stability), such as cohesion of the superstructure and adhesion to a substrate. The use of surface functionalization strategies, either to improve the stability of the crystals (e.g., hydrophobic coating to prevent environmental degradation)^[291–293] or modifying the substrates to improve the adhesion of the superstructure,^[294] could greatly improve the practical applications of these MOF assemblies. Other chemical methods including cross-linking or surface binding of the crystals could improve the interparticle interactions, and thus the cohesion of the superstructure.^[164] Encasing MOF superstructures in a polymer matrix is also a stabilizing strategy that is worth exploring; however, the challenges of this method are the preservation of the order and porosity of the MOF assembly. In this regard, effective secondary growth methods could explore the use of oriented MOF structures as seeds for the fabrication of larger (or less defective) single-crystalline domains.^[119] Although chemical methods are mostly associated with MOFs, we posit that physical methods, such as plasma surface functionalization, could be valuable approaches to improve adhesion to a given substrate.

To further expand the range of application of the oriented MOF superstructures, the opportunity to implement ordered MOF structures with functional particles (e.g., magnetic NP doping or magnetic functionalities,^[186,295,296] photoluminescent or conductive guests incorporated in the MOF pores^[297–300]) would greatly expand the available anisotropic functionalities.

A final input for the progress of the field is the need for a method that will quantify the degree of order achieved by the different protocols developed. In this regard, we suggest using – when possible – textural analysis to present quantitative data about the ordered domains present in the investigated volume of the sample. Additionally, we believe advancements in microscopy, such as TEM, will benefit this field providing accurate textural maps showcasing both local crystal domain and pore orientation. For example, in the case of heteroepitaxial growth, electron diffraction performed with transmission electron

microscopy (TEM) has been used to assess local heteroepitaxial relationships at the interface of ceramics-to-MOF^[44] or MOF-to-MOF^[268] heterostructures. We note that TEM-based techniques such as orientation and phase mapping^[89,90] have been successfully applied to metals, oxides and semiconductors to analyze nanoscale crystal orientation and construct orientational maps in areas of tens of microns. In comparison to these established materials, MOFs possess a higher sensitivity to electron beam irradiation, which can result in damage of the samples, presenting a bottleneck for the application of advanced TEM techniques in these systems.^[91] However, recent developments of cryo-TEM and low-energy protocols have enabled the application of these techniques for the characterization of short to medium-range order in sensitive polymers.^[301,302] Based on these promising advances, we envisage that the field of oriented MOF superstructures will benefit from these techniques. The detailed local information provided by TEM together with textural analysis performed by using XRD can provide powerful tools to characterize the alignment of oriented polycrystalline systems at different scales.

While we have addressed several pivotal points and explored equivalently valuable results, we firmly assert that the ability to create 3D-oriented MOF superstructures will be a transformative advancement for technology. This integration will unlock their functional properties across diverse systems, encompassing applications in sensing, microelectronics, and optics.

Supporting Information

Supporting Information is available from the Wiley Online Library or from the author.

Acknowledgements

The authors acknowledge support from the European Research Council under the European Union's Horizon 2020 Programme (FP/2014-2020)/ERC Grant Agreement No. 771834—POPCRYSTAL and TU Graz for the Lead Project (LP-03). JC thanks the European Research Council (ERC) for funding part of this work under the European Union's Horizon 2020 research and innovation programme (ERC Consolidator Grant Agreement 101002176) and the Österreichische Forschungsförderungsgesellschaft (FFG project BATMAN FFG-897938) for financial support.

Conflict of Interest

The authors declare no conflict of interest.

Keywords

aligned crystals, anisotropic MOFs, Metal-organic frameworks, MOF film, MOF patterns, MOF superstructure, oriented MOF

Received: September 18, 2023

Revised: October 19, 2023

Published online:

[1] O M. Yaghi, M. O'keeffe, N W. Ockwig, H K. Chae, M. Eddaoudi, J. Kim, *Nature* **2003**, *423*, 705.

- [2] S. Kitagawa, R. Kitaura, S.-I. Noro, *Angew. Chem., Int. Ed.* **2004**, *43*, 2334.
- [3] S R. Batten, N R. Champness, X.-M. Chen, J. Garcia-Martinez, S. Kitagawa, L. Öhrström, M. O'keeffe, M. Paik Suh, J. Reedijk, *Pure Appl. Chem.* **2013**, *85*, 1715.
- [4] T D. Bennett, A K. Cheetham, *Acc. Chem. Res.* **2014**, *47*, 1555.
- [5] J. Fonseca, T. Gong, Li Jiao, H.-L. Jiang, *J. Mater. Chem. A* **2021**, *9*, 10562.
- [6] M. Eddaoudi, J. Kim, N. Rosi, D. Vodak, J. Wachter, M. O'keeffe, O M. Yaghi, *Science* **2002**, *295*, 469.
- [7] P. Horcajada, R. Gref, T. Baati, P K. Allan, G. Maurin, P. Couvreur, G. Férey, R E. Morris, C. Serre, *Chem. Rev.* **2012**, *112*, 1232.
- [8] M. Eddaoudi, D B. Moler, H. Li, B. Chen, T M. Reineke, M. O'keeffe, O M. Yaghi, *Acc. Chem. Res.* **2001**, *34*, 319.
- [9] S T. Meek, J A. Greathouse, M D. Allendorf, *Adv. Mater.* **2011**, *23*, 249.
- [10] H. Furukawa, N. Ko, Y. B. Go, N. Aratani, S. B. Choi, E. Choi, A. Ö Yazaydin, R Q. Snurr, M. O'keeffe, J. Kim, O M. Yaghi, *Science* **2010**, *329*, 424.
- [11] H K. Chae, D Y. Siberio-Pérez, J. Kim, Y. Go, M. Eddaoudi, A J. Matzger, M. O'keeffe, O M. Yaghi, *Nature* **2004**, *427*, 523.
- [12] I M. Hönicke, I. Senkovska, V. Bon, I A. Baburin, N. Bönisch, S. Raschke, J D. Evans, S. Kaskel, *Angew. Chem., Int. Ed.* **2018**, *57*, 13780.
- [13] J.-R. Li, R J. Kuppler, H.-C. Zhou, *Chem. Soc. Rev.* **2009**, *38*, 1477.
- [14] J. Liu, L. Chen, H. Cui, J. Zhang, Li Zhang, C.-Y. Su, *Chem. Soc. Rev.* **2014**, *43*, 6011.
- [15] I. Stassen, N. Burtch, A. Talin, P. Falcaro, M. Allendorf, R. Ameloot, *Chem. Soc. Rev.* **2017**, *46*, 3185.
- [16] M. de J. Velásquez-Hernández, M. Linares-Moreau, E. Astria, F. Carraro, M. Z. Alyami, N. M. Khashab, C. J. Sumby, C. J. Doonan, P. Falcaro, *Coord. Chem. Rev.* **2021**, *429*, 213651.
- [17] A. Schneemann, V. Bon, I. Schwedler, I. Senkovska, S. Kaskel, R. A. Fischer, *Chem. Soc. Rev.* **2014**, *43*, 6062.
- [18] C M. Doherty, G. Grenci, R. Ricco, J I. Mardel, J. Reboul, S. Furukawa, S. Kitagawa, A J. Hill, P. Falcaro, *Adv. Mater.* **2013**, *25*, 4701.
- [19] C. Dimitrakakis, B. Marmiroli, H. Amenitsch, L. Malfatti, P. Innocenzi, G. Grenci, L. Vaccari, A J. Hill, B P. Ladewig, M R. Hill, P. Falcaro, *Chem. Commun.* **2012**, *48*, 7483.
- [20] M. Cavallini, C. Albonetti, F. Biscarini, *Adv. Mater.* **2009**, *21*, 1043.
- [21] D. Chen, Y. Wang, H. Zhou, Z. Huang, Y. Zhang, C. F. Guo, H. Zhou, *Adv. Mater.* **2022**, *34*, 2200903.
- [22] J. Zhang, Y. Li, X. Zhang, B. Yang, *Adv. Mater.* **2010**, *22*, 4249.
- [23] B. Jeong, H. Han, C. Park, *Adv. Mater.* **2020**, *32*, 2000597.
- [24] J. Xu, X. Wang, C. Wang, L. Yuan, W. Chen, J. Bao, Q. Su, Z. Xu, C. Wang, Z. Wang, D. Shan, B. Guo, *Adv. Mater.* **2021**, *33*, 2000893.
- [25] J. Chen, X. Liu, Y. Tian, W. Zhu, C. Yan, Y. Shi, L. B. Kong, H. J. Qi, K. Zhou, *Adv. Mater.* **2022**, *34*, 2102877.
- [26] G. A. Ermolaev, D. V. Grudinin, Y. V. Stebunov, K. V. Voronin, V. G. Kravets, J. Duan, A. B. Mazitov, G. I. Tselikov, A. Bylinkin, D. I. Yakubovsky, S. M. Novikov, D. G. Baranov, A. Y. Nikitin, I. A. Kruglov, T. Shegai, P. Alonso-González, A. N. Grigorenko, A. V. Arsenin, K. S. Novoselov, V. S. Volkov, *Nat. Commun.* **2021**, *12*, 854.
- [27] J. Muller, C. Kumar, A. K. Ghosh, V. Gupta, M. Tschoop, V. Le Houerou, A. Fery, G. Decher, M. Pauly, O. Felix, *ACS Appl. Mater. Interfaces* **2022**, *14*, 54073.
- [28] Y. Liang, H. Lin, S. Lin, J. Wu, W. Li, F. Meng, Y. Yang, X. Huang, B. Jia, Y. Kivshar, *Nano Lett.* **2021**, *21*, 8917.
- [29] Y. Chen, H. Liu, M. Reilly, H. Bae, M. Yu, *Nat. Commun.* **2014**, *5*, 5247.
- [30] Y. Li, C. P. Wong, in *Dielectr. Films Adv. Microelectron.*, John Wiley & Sons, Ltd, Chichester, **2007**, pp. 453–475.
- [31] S. Schott, E. Gann, L. Thomsen, S.-H. Jung, J.-K. Lee, C R. McNeill, H. Sirringhaus, *Adv. Mater.* **2015**, *27*, 7356.

- [32] G. Xu, K. Otsubo, T. Yamada, S. Sakaida, H. Kitagawa, *J. Am. Chem. Soc.* **2013**, *135*, 7438.
- [33] H. J. Cho, Y. Wu, Yu-Q Zhang, B. Feng, M. Mikami, W. Shin, Y. Ikuhara, Yu-M Sheu, K. Saito, H. Ohta, *Adv. Mater. Interfaces* **2021**, *8*, 2001932.
- [34] J. Castillo-Seoane, L. Contreras-Bernal, J. M. Obrero-Perez, X. García-Casas, F. Lorenzo-Lázaro, F. J. Aparicio, C. Lopez-Santos, T. C. Rojas, J. A. Anta, A. Borrás, Á. Barranco, J. R. Sanchez-Valencia, *Adv. Mater.* **2022**, *34*, 2107739.
- [35] Y. Li, K. Luo, R. Tao, Z. Wang, D. Chen, Z. Shao, *Adv. Funct. Mater.* **2020**, *30*, 2002606.
- [36] B. Park, Y Ho Huh, J. C. Shin, *Sol. Energy Mater. Sol. Cells* **2011**, *95*, 3543.
- [37] M. Xiao, B. Kang, S. B. Lee, L M. A. Perdigão, A. Luci, D A. Warr, S P. Senanayak, M. Nikolka, M. Statz, Y. Wu, A. Sadhanala, S. Schott, R. Carey, Q. Wang, M. Lee, C. Kim, A. Onwubiko, C. Jellett, H. Liao, W. Yue, K. Cho, G. Costantini, I. Mcculloch, H. Sirringhaus, *Adv. Mater.* **2020**, *32*, 2000063.
- [38] J. K. Kearns, in *Single Cryst. Electron. Mater.* (Ed.: R. Fornari), Woodhead Publishing, Cambridge, **2019**, pp. 5–56.
- [39] P. Capper, *Springer Handbook of Electronic and Photonic Materials* (Ed.: S. Kasap, P. Capper), Springer Berlin Heidelberg, New York, NY, **2017**, pp. 269–289.
- [40] L-C. Lim, *Handbook of Dielectric, Piezoelectric and Ferroelectric Materials: Synthesis, Properties and Applications* (Ed: Z.-G. Ye), Woodhead Publishing, Cambridge, **2008**, pp. 38–44.
- [41] Y. Zheng, E. Shi, Z. Lu, S. Cui, S. Wang, W. Zhong, *J. Cryst. Growth* **2005**, *275*, e895.
- [42] S. Yang, J. Zhang, M. Chi, Y. Wen, X. Chen, C. Wang, X. Liu, *Materialia* **2019**, *5*, 100200.
- [43] P. Falcaro, R. Ricco, C M. Doherty, K. Liang, A J. Hill, M J. Styles, *Chem. Soc. Rev.* **2014**, *43*, 5513.
- [44] P. Falcaro, K. Okada, T. Hara, K. Ikigaki, Y. Tokudome, A. W. Thornton, A. J. Hill, T. Williams, C. Doonan, M. Takahashi, *Nat. Mater.* **2017**, *16*, 342.
- [45] M De J. Velásquez-Hernández, M. Linares-Moreau, L A. Brandner, B. Marmiroli, M. Barella, G P. Acuna, S. D. Zilio, M F. K. Verstreken, D E. Kravchenko, O M. Linder-Patton, J D. Evans, H. Wiltsche, F. Carraro, H. Wolinski, R. Ameloot, C. Doonan, P. Falcaro, *Adv. Mater.* **2023**, *35*, 2211478.
- [46] M. A. Herman, W. Richter, H. Sitter, in *Epitaxy Phys. Princ. Tech. Implement.* (Eds.: M. A. Herman, W. Richter, H. Sitter), Springer, Berlin, Heidelberg, **2004**, pp. 389–421.
- [47] M. Y. B. Zulkifli, R. Lin, M. Chai, V. Chen, J. Hou, *J. Mater. Chem. A* **2022**, *10*, 14641.
- [48] K. Hirai, K. Sumida, M. Meilikhov, N. Louvain, M. Nakahama, H. Uehara, S. Kitagawa, S. Furukawa, *J. Mater. Chem. C* **2014**, *2*, 3336.
- [49] I. Hussain, S. Iqbal, C. Lamiel, A. Alfantazi, K. Zhang, *J. Mater. Chem. A* **2022**, *10*, 4475.
- [50] A. Labropoulos, C. Veziri, M. Kapsi, G. Pilatos, V. Likodimos, M. Tsapatsis, N K. Kanellopoulos, G E. Romanos, G N. Karanikolos, *Chem. Mater.* **2015**, *27*, 8198.
- [51] H. Bux, A. Feldhoff, J. Cravillon, M. Wiebcke, Y.-S. Li, J. Caro, *Chem. Mater.* **2011**, *23*, 2262.
- [52] Bo Liu, M. Tu, R A. Fischer, *Angew. Chem., Int. Ed.* **2013**, *52*, 3402.
- [53] K. Okada, M. Nakanishi, K. Ikigaki, Y. Tokudome, P. Falcaro, C J. Doonan, M. Takahashi, *Chem. Sci.* **2020**, *11*, 8005.
- [54] A C. Soegiarto, A. Comotti, M D. Ward, *J. Am. Chem. Soc.* **2010**, *132*, 14603.
- [55] Yu Chen, S. Guerin, H. Yuan, J. O'donnell, B. Xue, P.-A. Cazade, E. Ul Haq, L J. W. Shimon, S. Rencus-Lazar, S A. M. Tofail, Yi Cao, D. Thompson, R. Yang, E. Gazit, *J. Am. Chem. Soc.* **2022**, *144*, 3468.
- [56] L. Zhang, H. Li, Yu Yang, D. Yang, Y. Cui, G. Qian, *J. Mater. Chem. C* **2022**, *10*, 14915.
- [57] J. Wu, A F. Gross, S H. Tolbert, *J. Phys. Chem. B* **1999**, *103*, 2374.
- [58] T. Bein, *MRS Bull.* **2005**, *30*, 713.
- [59] G. Wu, J. Huang, Y. Zang, J. He, G. Xu, *J. Am. Chem. Soc.* **2017**, *139*, 1360.
- [60] T. Ohata, A. Nomoto, T. Watanabe, I. Hirosawa, T. Makita, J. Takeya, R. Makura, *ACS Appl. Mater. Interfaces* **2021**, *13*, 54570.
- [61] B. M. Venkatesan, R. Bashir, *Nat. Nanotechnol.* **2011**, *6*, 615.
- [62] J. Cho, Y. Ishida, *Adv. Mater.* **2017**, *29*, 1605974.
- [63] L.-L. Ma, C.-Yi Li, J.-T. Pan, Y.-E. Ji, C. Jiang, R. Zheng, Ze-Yu Wang, Yu Wang, B.-X. Li, Y.-Q. Lu, *Light Sci Appl* **2022**, *11*, 270.
- [64] T. Rodenas, I. Luz, G. Prieto, B. Seoane, H. Miro, A. Corma, F. Kapteijn, F X. Llabrés I Xamena, J. Gascon, *Nat. Mater.* **2014**, *14*, 48.
- [65] L. Padurariu, L. Curecheriu, C. Galassi, L. Mitoseriu, *Appl. Phys. Lett.* **2012**, *100*, 252905.
- [66] J. Fonseca, L. Meng, I. Imaz, D. MasPOCH, *Chem. Soc. Rev.* **2023**, *52*, 2528.
- [67] I E. Khalil, J. Fonseca, M R. Reithofer, T. Eder, J. M. Chin, *Coord. Chem. Rev.* **2023**, *481*, 215043.
- [68] S. Furukawa, J. Reboul, S. Diring, K. Sumida, S. Kitagawa, *Chem. Soc. Rev.* **2014**, *43*, 5700.
- [69] R-Qi Song, H. Cölfen, *Adv. Mater.* **2010**, *22*, 1301.
- [70] M. Jehannin, A. Rao, H. Cölfen, *J. Am. Chem. Soc.* **2019**, *141*, 10120.
- [71] L. Zhou, P. O'brien, *Small* **2008**, *4*, 1566.
- [72] E V. Sturm (Née Rosseeva), H. Cölfen, *Chem. Soc. Rev.* **2016**, *45*, 5821.
- [73] Z. Dou, J. Yu, H. Xu, Y. Cui, Yu Yang, G. Qian, *Thin Solid Films* **2013**, *544*, 296.
- [74] R. Ameloot, L. Stappers, J. Fransaer, L. Alaerts, B F. Sels, D E. De Vos, *Chem. Mater.* **2009**, *21*, 2580.
- [75] Y. Liu, Z. Ng, E A. Khan, H.-K. Jeong, C.-B. Ching, Z. Lai, *Microporous Mesoporous Mater.* **2009**, *118*, 296.
- [76] X. Liu, W. Fu, E. Bouwman, *Chem. Commun.* **2016**, *52*, 6926.
- [77] C. T. Lee, M. W. Shin, *Surf. Interfaces* **2021**, *22*, 100845.
- [78] Y.-S. Li, H. Bux, A. Feldhoff, G.-L. Li, W.-S. Yang, J. Caro, *Adv. Mater.* **2010**, *22*, 3322.
- [79] Q. Li, J. Gies, X.-J. Yu, Yu Gu, A. Terfort, M. Kind, *Chemistry* **2020**, *26*, 5185.
- [80] H K. Arslan, O. Shekhah, J. Wohlgemuth, M. Franzreb, R A. Fischer, C. Wöll, *Adv. Funct. Mater.* **2011**, *21*, 4228.
- [81] O. Shekhah, H. Wang, S. Kowarik, F. Schreiber, M. Paulus, M. Tolan, C. Sternemann, F. Evers, D. Zacher, R A. Fischer, C. Wöll, *J. Am. Chem. Soc.* **2007**, *129*, 15118.
- [82] K. Allahyarli, M R. Reithofer, F. Cheng, A J. Young, E. Kiss, T. T. Y. Tan, A. Prado-Roller, J. M. Chin, *J. Colloid Interface Sci.* **2022**, *610*, 1027.
- [83] C. Avci, I. Imaz, A. Carné-Sánchez, J. A. Pariente, N. Tasios, J. Pérez-Carvajal, M. I. Alonso, A. Blanco, M. Dijkstra, C. López, D. MasPOCH, *Nat. Chem.* **2018**, *10*, 78.
- [84] A. Clarke, C. Eberhardt, *Microscopy Techniques for Materials Science*, Woodhead Publishing, Cambridge, **2002**.
- [85] M. Ma, A. Gross, D. Zacher, A. Pinto, H. Noei, Y. Wang, R A. Fischer, N. Metzler-Nolte, *CrystEngComm* **2011**, *13*, 2828.
- [86] F. Cheng, A J. Young, J-S G. Bouillard, N T. Kemp, R. Guillet-Nicolas, C H. Hall, D. Roberts, A H. Jaafar, A M. Adawi, F. Kleitz, A. Imhof, M R. Reithofer, J. M. Chin, *J. Am. Chem. Soc.* **2019**, *141*, 12989.
- [87] M. Bäumer, H.-J. Freund, *Prog. Surf. Sci.* **1999**, *61*, 127.
- [88] P. Reiss, M. Protière, L. Li, *Small* **2009**, *5*, 154.
- [89] E. F. Rauch, M. Véron, *Mater. Charact.* **2014**, *98*, 1.
- [90] D. Viladot, M. Véron, M. Gemmi, F. Peiró, J. Portillo, S. Estradé, J. Mendoza, N. Llorca-Isern, S. Nicolopoulos, *J Microsc* **2013**, *252*, 23.
- [91] L. Liu, D. Zhang, Y. Zhu, Y. Han, *Commun Chem* **2020**, *3*, 1.
- [92] J. Ayache, L. Beaunier, J. Boumendil, G. Ehret, D. Laub, *Sample Preparation Handbook for Transmission Electron Microscopy*, Springer, New York, NY, **2010**.

- [93] D N. Johnstone, F C. N. Firth, C P. Grey, P A. Midgley, M J. Cliffe, S M. Collins, *J. Am. Chem. Soc.* **2020**, *142*, 13081.
- [94] Z. Huang, M. Ge, F. Carraro, C. Doonan, P. Falcaro, X. Zou, *Faraday Discuss.* **2021**, *225*, 118.
- [95] M. Ge, Y. Wang, F. Carraro, W. Liang, M. Roostaeinia, S. Siahrostami, D M. Proserpio, C. Doonan, P. Falcaro, H. Zheng, X. Zou, Z. Huang, *Angew. Chem., Int. Ed.* **2021**, *60*, 11391.
- [96] C. Wiktor, M. Meledina, S. Turner, O I. Lebedev, R A. Fischer, *J. Mater. Chem. A* **2017**, *5*, 14969.
- [97] X. Gong, K. Gnanasekaran, Z. Chen, L. Robison, M C. Wasson, K.C. Bentz, S M. Cohen, O K. Farha, N C. Gianneschi, *J. Am. Chem. Soc.* **2020**, *142*, 17224.
- [98] G. Cappuccio, M. L. Terranova, Thin Film Characterisation by Advanced X-Ray Diffraction Techniques: Frascati, October 2–5, 1996, S. I. S. Pubblicazioni, L N Di Frascati, **1996**.
- [99] G F. Harrington, J. Santiso, *J. Electroceramics* **2021**, *47*, 141.
- [100] Y. Waseda, E. Matsubara, K. Shinoda, *X-Ray Diffraction Crystallography*, Springer, Berlin, Heidelberg, **2011**.
- [101] B. D. Cullity, S. R. Stock, *Elements of X-Ray Diffraction*, Pearson Education, Harlow, **2014**.
- [102] H. P. Klug, L. E. Alexander, *X-Ray Diffraction Procedures for Polycrystalline and Amorphous Materials*, Wiley, New York, **1974**.
- [103] J. Epp, in *Mater. Charact. Using Nondestruct. Eval. NDE Methods* (Eds.: G. Hübschen, I. Altpeter, R. Tschuncky, H.-G. Herrmann), Woodhead Publishing, Cambridge, **2016**, pp. 81–124.
- [104] E. Zanchetta, L. Malfatti, R. Ricco, M J. Styles, F. Lisi, C J. Coglian, C J. Doonan, A J. Hill, G. Brusatin, P. Falcaro, *Chem. Mater.* **2015**, *27*, 690.
- [105] H. T. Kwon, H.-K. Jeong, *J. Am. Chem. Soc.* **2013**, *135*, 10763.
- [106] X. Zhao, C. Zhou, Y. Lvov, M. Liu, *Small* **2019**, *15*, 1900357.
- [107] Y. Chen, T. Liang, L. Chen, Y. Chen, Bo-Ru Yang, Y. Luo, G.-S. Liu, *Nanoscale Horiz.* **2022**, *7*, 1299.
- [108] C. Zhao, P. Zhang, J. Zhou, S. Qi, Y. Yamauchi, R. Shi, R. Fang, Y. Ishida, S. Wang, A P. Tomsia, M. Liu, L. Jiang, *Nature* **2020**, *580*, 210.
- [109] A. Schoedel, C. Scherb, T. Bein, *Angew. Chem., Int. Ed.* **2010**, *49*, 7225.
- [110] E. Biemmi, C. Scherb, T. Bein, *J. Am. Chem. Soc.* **2007**, *129*, 8054.
- [111] W.-J. Li, M. Tu, R. Cao, R.A. Fischer, *J. Mater. Chem. A* **2016**, *4*, 12356.
- [112] I. Stassen, M. Styles, G. Grenci, H.-V. Gorp, W. Vanderlinden, S. D. Feyter, P. Falcaro, D De Vos, P. Vereecken, R. Ameloot, *Nat. Mater.* **2015**, *15*, 304.
- [113] S. Rodríguez-Hermida, D E. Kravchenko, N. Wauteraerts, R. Ameloot, *Inorg. Chem.* **2022**, *61*, 17927.
- [114] C. Carbonell, I. Imaz, D. Maspoch, *J. Am. Chem. Soc.* **2011**, *133*, 2144.
- [115] N. Rangnekar, N. Mittal, B. Elyassi, J. Caro, M. Tsapatsis, *Chem. Soc. Rev.* **2015**, *44*, 7128.
- [116] Z. Wang, C. Wöll, *Adv. Mater. Technol.* **2019**, *4*, 1800413.
- [117] J.-L. Zhuang, A. Terfort, C. Wöll, *Coord. Chem. Rev.* **2016**, *307*, 391.
- [118] G. Bonilla, D. G. Vlachos, M. Tsapatsis, *Microporous Mesoporous Mater.* **2001**, *42*, 191.
- [119] A. Deng, X. Shen, Z. Wan, Y. Li, S. Pang, X. He, J. Caro, A. Huang, *Angew. Chem., Int. Ed.* **2021**, *60*, 25463.
- [120] A. Van der Drift, *Philips Res. Rep.* **1967**, *22*, 267.
- [121] H. T. Kwon, H.-K. Jeong, *Chem. Commun.* **2013**, *49*, 3854.
- [122] T T. Y. Tan, M R. Reithofer, E Y. Chen, A G. Menon, T. S. A Hor, J. Xu, J. M. Chin, *J. Am. Chem. Soc.* **2013**, *135*, 16272.
- [123] R. Ranjan, M. Tsapatsis, *Chem. Mater.* **2009**, *21*, 4920.
- [124] H. T. Kwon, H.-K. Jeong, A S. Lee, He S An, J. S. Lee, *J. Am. Chem. Soc.* **2015**, *137*, 12304.
- [125] Y. Liu, G. Zeng, Y. Pan, Z. Lai, *J. Membr. Sci.* **2011**, *379*, 46.
- [126] H. Li, J. Hou, T D. Bennett, J. Liu, Y. Zhang, *J. Mater. Chem. A* **2019**, *7*, 5811.
- [127] Y. Sun, D. Yan, Y. Wu, F.-Y. Shih, C. Zhang, H. Luo, S.-H. Lin, Yi Liu, *ACS Mater. Lett.* **2022**, *4*, 55.
- [128] Yu-Qi Wu, L.-H. Xie, Xi Qin, Yu-X Sun, Ya-Bo Xie, J.-R. Li, *Crystals* **2018**, *8*, 383.
- [129] Y. Sun, J. Yan, Y. Gao, T. Ji, S. Chen, C. Wang, P. Lu, Y. Li, Yi Liu, *Angew. Chem., Int. Ed.* **2023**, *62*, e202216697.
- [130] Z.-G. Gu, A. Pfriem, S. Hamsch, H. Breitwieser, J. Wohlgemuth, L. Heinke, H. Gliemann, C. Wöll, *Microporous Mesoporous Mater.* **2015**, *211*, 82.
- [131] O. Shekhah, H. Wang, M. Paradinas, C. Ocal, B. Schüpbach, A. Terfort, D. Zacher, R A. Fischer, C. Wöll, *Nat. Mater.* **2009**, *8*, 481.
- [132] L. Heinke, M. Tu, S. Wannapaiboon, R A. Fischer, C. Wöll, *Microporous Mesoporous Mater.* **2015**, *216*, 200.
- [133] M. Tsotsalas, A. Umemura, F. Kim, Y. Sakata, J. Reboul, S. Kitagawa, S. Furukawa, *J. Mater. Chem.* **2012**, *22*, 10159.
- [134] R. Makura, S. Motoyama, Y. Umemura, H. Yamanaka, O. Sakata, H. Kitagawa, *Nat. Mater.* **2010**, *9*, 565.
- [135] K. Otsubo, H. Kitagawa, *APL Mater.* **2014**, *2*, 124105.
- [136] R. Zheng, Z.-H. Fu, W.-H. Deng, Y. Wen, Ai-Q Wu, X.-L. Ye, G. Xu, *Angew. Chem., Int. Ed.* **2022**, *61*, e202212797.
- [137] B. H. Monjezi, S. Okur, R. Limbach, A. Chandresh, K. Sen, T. Hashem, M. Schwotzer, L. Wondraczek, C. Wöll, A. Knebel, *ACS Nano* **2023**, *17*, 6121.
- [138] V. Chernikova, O. Shekhah, M. Eddaoudi, *ACS Appl. Mater. Interfaces* **2016**, *8*, 20459.
- [139] G. Xu, T. Yamada, K. Otsubo, S. Sakaida, H. Kitagawa, *J. Am. Chem. Soc.* **2012**, *134*, 16524.
- [140] J.-L. Zhuang, M. Kind, C M. Grytz, F. Farr, M. Diefenbach, S. Tussupbayev, M C. Holthausen, A. Terfort, *J. Am. Chem. Soc.* **2015**, *137*, 8237.
- [141] K. Otsubo, T. Haraguchi, H. Kitagawa, *Coord. Chem. Rev.* **2017**, *346*, 123.
- [142] J. Liu, C. Wöll, *Chem. Soc. Rev.* **2017**, *46*, 5730.
- [143] A. Bétard, R A. Fischer, *Chem. Rev.* **2012**, *112*, 1055.
- [144] Z. Ji, R. Freund, C S. Diercks, P. Hirschle, O M. Yaghi, S. Wuttke, *Adv. Mater.* **2021**, *33*, 2103808.
- [145] F. Cheng, E S. Marshall, A J. Young, P J. Robinson, J-S G. Bouillard, A M. Adawi, N A. Vermeulen, O K. Farha, M R. Reithofer, J. M. Chin, *Chem. Eur. J.* **2017**, *23*, 15578.
- [146] G. Lu, C. Cui, W. Zhang, Y. Liu, F. Huo, *Chem Asian J* **2013**, *8*, 69.
- [147] J. Troyano, A. Carné-Sánchez, C. Avci, I. Imaz, D. Maspoch, *Chem. Soc. Rev.* **2019**, *48*, 5534.
- [148] M. Sindoro, N. Yanai, Ah-Y Jee, S. Granick, *Acc. Chem. Res.* **2014**, *47*, 459.
- [149] Xu Chen, Y. Zhuang, N. Rampal, R. Hewitt, G. Divitini, C A. O'keefe, X. Liu, D J. Whitaker, J W. Wills, R. Jugdaohsingh, J J. Powell, H. Yu, C P. Grey, O A. Scherman, D. Fairén-Jimenez, *J. Am. Chem. Soc.* **2021**, *143*, 13557.
- [150] E. Alonso-Redondo, M. Schmitt, Z. Urbach, C. M. Hui, R. Sainidou, P. Rembert, K. Matyjaszewski, M. R. Bockstaller, G. Fytas, *Nat. Commun.* **2015**, *6*, 8309.
- [151] E. P. K. Currie, W. Norde, M. A. Cohen Stuart, *Adv. Colloid Interface Sci.* **2003**, *100–102*, 205.
- [152] S. Ding, Y. Zhang, F. Lou, M. K. Aslam, Y. Sun, M. Li, J. Duan, Y. Li, S. Chen, *J. Mater. Chem. A* **2022**, *10*, 20813.
- [153] Y. S. Lee, In *Self-Assem. Nanotechnol*, John Wiley & Sons, Ltd, Hoboken, NJ, **2008**, pp. 1–19.
- [154] K. J. M. Bishop, C E. Wilmer, S. Soh, B A. Grzybowski, *Small Weinbergstr. Ger.* **2009**, *5*, 1600.
- [155] An-Q Xie, Q. Li, Y. Xi, L. Zhu, Su Chen, *Acc Mater Res* **2023**, *4*, 403.
- [156] M. Pang, A J. Cairns, Y. Liu, Y. Belmabkhout, H. C. Zeng, M. Eddaoudi, *J. Am. Chem. Soc.* **2012**, *134*, 13176.
- [157] N. Yanai, S. Granick, *Angew. Chem., Int. Ed.* **2012**, *51*, 5638.

- [158] D. Lyu, W. Xu, J E L. Payong, T. Zhang, Y. Wang, *Nat. Commun.* **2022**, *13*, 3980.
- [159] K L. Young, M R. Jones, J. Zhang, R J. Macfarlane, R. Esquivel-Sirvent, R J. Nap, J. Wu, G C. Schatz, B. Lee, C A. Mirkin, *Proc Natl Acad Sci U S A* **2012**, *109*, 2240.
- [160] J. Kim, X. Song, F. Ji, B. Luo, N F. Ice, Q. Liu, Q. Zhang, Q. Chen, *Nano Lett.* **2017**, *17*, 3270.
- [161] C. Avci, Y. Liu, J. A. Pariente, A. Blanco, C. Lopez, I. Imaz, D. Maspoch, *Small* **2019**, *15*, 1902520.
- [162] Y. Katayama, M. Kalaj, K S. Barcus, S M. Cohen, *J. Am. Chem. Soc.* **2019**, *141*, 20000.
- [163] J. Y. Kim, K. Barcus, S M. Cohen, *J. Am. Chem. Soc.* **2021**, *143*, 3703.
- [164] K. Barcus, Po-An Lin, Y. Zhou, G. Arya, S M. Cohen, *ACS Nano* **2022**, *16*, 18168.
- [165] S. Motoyama, R. Makiura, O. Sakata, H. Kitagawa, *J. Am. Chem. Soc.* **2011**, *133*, 5640.
- [166] P A. Kralchevsky, K. Nagayama, *Langmuir* **1994**, *10*, 23.
- [167] E P. Lewandowski, M. Cavallaro, L. Botto, J C. Bernate, V. Garbin, K J. Stebe, *Langmuir* **2010**, *26*, 15142.
- [168] P. Yang, F. Kim, *ChemPhysChem* **2002**, *3*, 503.
- [169] K D. Danov, P A. Kralchevsky, *Adv. Colloid Interface Sci.* **2010**, *154*, 91.
- [170] S. Yu, X. Wang, X. Jiao, C. Li, D. Chen, *J. Mater. Chem. C* **2021**, *9*, 5379.
- [171] M. Qiu, Z. Zhu, D. Wang, Z. Xu, W. Miao, L. Jiang, Ye Tian, *J. Am. Chem. Soc.* **2023**, *145*, 12275.
- [172] S. Wang, S S. Park, C T. Buru, H. Lin, P.-C. Chen, E W. Roth, O K. Farha, C A. Mirkin, *Nat. Commun.* **2020**, *11*, 2495.
- [173] R J. Macfarlane, B. Lee, M R. Jones, N. Harris, G C. Schatz, C A. Mirkin, *Science* **2011**, *334*, 204.
- [174] N J. Agard, J A. Prescher, C R. Bertozzi, *J. Am. Chem. Soc.* **2004**, *126*, 15046.
- [175] Z. Gong, T. Hueckel, Gi-Ra Yi, S. Sacanna, *Nature* **2017**, *550*, 234.
- [176] E. Bianchi, R. Blaak, C N. Likos, *Phys. Chem. Chem. Phys.* **2011**, *13*, 6397.
- [177] D. Lyu, W. Xu, Y. Wang, *Angew. Chem.* **2022**, *134*, e202115076.
- [178] S. Deville, *Adv. Eng. Mater.* **2008**, *10*, 155.
- [179] Y. Song, X. Song, X. Wang, J. Bai, F. Cheng, C. Lin, X. Wang, H. Zhang, J. Sun, T. Zhao, H. Nara, Y. Sugahara, X. Li, Y. Yamauchi, *J. Am. Chem. Soc.* **2022**, *144*, 17457.
- [180] R. Qin, *Sci. Rep.* **2017**, *7*, 8449.
- [181] J A. Beardslee, B. Sadtler, N S. Lewis, *ACS Nano* **2012**, *6*, 10303.
- [182] B M. I. Van Der Zande, G J. M. Koper, H N. W. Lekkerkerker, *J. Phys. Chem. B* **1999**, *103*, 5754.
- [183] S. Takashima, H. P. Schwan, *Biophys. J.* **1985**, *47*, 513.
- [184] R A. Vaia, J F. Maguire, *Chem. Mater.* **2007**, *19*, 2736.
- [185] R. Qin, *Adv. Mater. Lett.* **2019**, *10*, 899.
- [186] R. Ricco, L. Malfatti, M. Takahashi, A J. Hill, P. Falcaro, *J. Mater. Chem. A* **2013**, *1*, 13033.
- [187] P. Falcaro, F. Normandin, M. Takahashi, P. Scopece, H. Amenitsch, S. Costacurta, C M. Doherty, J S. Laird, M D. H. Lay, F. Lisi, A J. Hill, D. Buso, *Adv. Mater.* **2011**, *23*, 3901.
- [188] M. Van Essen, E. Montrée, M. Houben, Z. Borneman, K. Nijmeijer, *Membranes* **2020**, *10*, 155.
- [189] F. Kimura, T. Kimura, *CrystEngComm* **2018**, *20*, 861.
- [190] F. Kimura, S. Horii, I. Arimoto, D. Notsu, T. Doi, M. Wada, T. Kimura, *CrystEngComm* **2019**, *21*, 4221.
- [191] T. Kimura, C. Chang, F. Kimura, M. Maeyama, *J. Appl. Crystallogr.* **2009**, *42*, 535.
- [192] N. Yanai, M. Sindoro, J. Yan, S. Granick, *J. Am. Chem. Soc.* **2013**, *135*, 34.
- [193] S. Basuray, H.-C. Chang, *Phys Rev E* **2007**, *75*, 060501.
- [194] J. C. Maxwell, *A Treatise on Electricity and Magnetism*, Clarendon Press, Oxford, **1873**.
- [195] R. W. Sillars, *J. Inst. Electr. Eng.* **1937**, *80*, 378.
- [196] V. N. Shilov, A. V. Delgado, F. González-Caballero, J. Horno, J. J. López-García, C. Grosse, *J. Colloid Interface Sci.* **2000**, *232*, 141.
- [197] L. Onsager, *Ann. N. Y. Acad. Sci.* **1949**, *51*, 627.
- [198] P. Bolhuis, D. Frenkel, *J. Chem. Phys.* **1997**, *106*, 666.
- [199] J. Andreo, A. D. Balsa, M. Y. Tsang, A. Sinelshchikova, O. Zaremba, S. Wuttke, J. M. Chin, *Chem. Mater.* **2023**, *35*, 6943.
- [200] C. Mellot-Draznieks, C. Serre, S. Surblé, N. Audebrand, G. Férey, *J. Am. Chem. Soc.* **2005**, *127*, 16273.
- [201] J. Troyano, A. Carné-Sánchez, J. Pérez-Carvajal, L. León-Reina, I. Imaz, A. Cabeza, D. Maspoch, *Angew. Chem., Int. Ed.* **2018**, *57*, 15420.
- [202] J. Troyano, A. Carné-Sánchez, D. Maspoch, *Adv. Mater.* **2019**, *31*, 1808235.
- [203] Z. Hao, S. Song, B. Li, Q.-X. Jia, T. Zheng, Z. Zhang, *Sens. Actuators, B* **2022**, *358*, 131448.
- [204] C. M. Doherty, D. Buso, A J. Hill, S. Furukawa, S. Kitagawa, P. Falcaro, *Acc. Chem. Res.* **2014**, *47*, 396.
- [205] J. Reboul, S. Furukawa, N. Horike, M. Tsotsalas, K. Hirai, H. Uehara, M. Kondo, N. Louvain, O. Sakata, S. Kitagawa, *Nat. Mater.* **2012**, *11*, 717.
- [206] H. Yuan, J. Cui, N. Li, M. Li, X. Yu, W. Fan, A. Karmakar, J. Dong, S. J. Pennycook, H. Cai, D. Zhao, *ACS Appl. Mater. Interfaces* **2020**, *12*, 36715.
- [207] R. Riccò, O. Linder-Patton, K. Sumida, M J. Styles, K. Liang, H. Amenitsch, C J. Doonan, P. Falcaro, *Chem. Mater.* **2018**, *30*, 5630.
- [208] C. Li, Y. Gao, X. Xia, J. Zhu, X. Wang, Y. Fu, *Small* **2020**, *16*, 1907043.
- [209] K. Khaletskaya, S. Turner, M. Tu, S. Wannapaiboon, A. Schnemann, R. Meyer, A. Ludwig, G. Van Tendeloo, R A. Fischer, *Adv. Funct. Mater.* **2014**, *24*, 4804.
- [210] R. Bo, M. Taheri, B. Liu, R. Ricco, H. Chen, H. Amenitsch, Z. Fusco, T. Tsuzuki, G. Yu, R. Ameloot, P. Falcaro, A. Tricoli, *Adv. Sci.* **2020**, *7*, 2002368.
- [211] S. Zhou, Y. Wei, J. Hou, L.-X. Ding, H. Wang, *Chem. Mater.* **2017**, *29*, 7103.
- [212] Y. Li, Lu Lin, M. Tu, P. Nian, A J. Howarth, O K. Farha, J. Qiu, X. Zhang, *Nano Res.* **2018**, *11*, 1850.
- [213] I. Stassen, N. Campagnol, J. Fransaer, P. Vereecken, D. De Vos, R. Ameloot, *CrystEngComm* **2013**, *15*, 9308.
- [214] A. J. Cruz, I. Stassen, M. Krishtab, K. Marcoen, T. Stassin, S. Rodríguez-Hermida, J. Teyssandier, S. Pletinckx, R. Verbeke, V. Rubio-Giménez, S. Tataj, C. Martí-Gastaldo, J. Meerschaut, P M. Vereecken, S. De Feyter, T. Hauffman, R. Ameloot, *Chem. Mater.* **2019**, *31*, 9462.
- [215] M. Kräuter, A. J. Cruz, T. Stassin, S. Rodríguez-Hermida, R. Ameloot, R. Resel, A. M. Coelite, *Crystals* **2022**, *12*, 217.
- [216] T. Stassin, S. Rodríguez-Hermida, B. Schrode, A. J. Cruz, F. Carraro, D. Kravchenko, V. Creemers, I. Stassen, T. Hauffman, D. De Vos, P. Falcaro, R. Resel, R. Ameloot, *Chem. Commun.* **2019**, *55*, 10056.
- [217] H. R. Oswald, A. Reller, H. W. Schmalle, E. Dubler, *Acta Crystallogr. C* **1990**, *46*, 2279.
- [218] A. Tarzia, M. Takahashi, P. Falcaro, A W. Thornton, C J. Doonan, D M. Huang, *ACS Appl. Mater. Interfaces* **2018**, *10*, 40938.
- [219] Z. Wang, J. Liu, B. Lukose, Z. Gu, P G. Weidler, H. Gliemann, T. Heine, C. Wöll, *Nano Lett.* **2014**, *14*, 1526.
- [220] M. Linares-Moreau, L. A. Brandner, T. Kamencek, S. Klošek, F. Carraro, K. Okada, M. Takahashi, E. Zojer, C J. Doonan, P. Falcaro, *Adv. Mater. Interfaces* **2021**, *8*, 2101039.
- [221] B. Baumgartner, K. Ikigaki, K. Okada, M. Takahashi, *Chem. Sci.* **2021**, *12*, 9298.
- [222] K. Ikigaki, K. Okada, Y. Tokudome, T. Toyao, P. Falcaro, C J. Doonan, M. Takahashi, *Angew. Chem., Int. Ed.* **2019**, *58*, 6886.

- [223] S. Klokic, D. Naumenko, B. Marmiroli, F. Carraro, M. Linares-Moreau, S. D. Zilio, G. Birarda, R. Kargl, P. Falcaro, H. Amenitsch, *Chem. Sci.* **2022**, *13*, 11869.
- [224] N. D. Shepherd, D. M. D'alessandro, *Chem. Phys. Rev.* **2021**, *2*, 011301.
- [225] K. Griffiths, N. R. Halcovitch, J. M. Griffin, *Chem. Mater.* **2020**, *32*, 9925.
- [226] S. Gong, L. W. Yap, B. Zhu, W. Cheng, *Adv. Mater.* **2020**, *32*, 1902278.
- [227] Y. Kim, X. Zhao, *Chem. Rev.* **2022**, *122*, 5317.
- [228] Y. Diao, B. C.-K. Tee, G. Giri, J. Xu, D. H. Kim, H. A. Becerril, R. M. Stoltenberg, T. H. Lee, G. Xue, S. C. B. Mannsfeld, Z. Bao, *Nat. Mater.* **2013**, *12*, 665.
- [229] H. Gao, Y. Qiu, J. Feng, S. Li, H. Wang, Y. Zhao, X. Wei, X. Jiang, Y. Su, Y. Wu, L. Jiang, *Nat. Commun.* **2019**, *10*, 3912.
- [230] Y.-W. Chiang, J.-J. Chang, C.-Yi Chou, C.-S. Wu, En-Li Lin, E. L. Thomas, *Adv. Opt. Mater.* **2015**, *3*, 1517.
- [231] K. M. Herbert, H. E. Fowler, J. M. Mccracken, K. R. Schlafmann, J. A. Koch, T. J. White, *Nat. Rev. Mater.* **2022**, *7*, 23.
- [232] K. Fukuhara, S. Nagano, M. Hara, T. Seki, *Nat. Commun.* **2014**, *5*, 3320.
- [233] Y. Gao, M. C. Weidman, W. A. Tisdale, *Nano Lett.* **2017**, *17*, 3837.
- [234] J.-H. Ahn, H.-S. Kim, K. J. Lee, S. Jeon, S. J. Kang, Y. Sun, R. G. Nuzzo, J. A. Rogers, *Science* **2006**, *314*, 1754.
- [235] M. H. Huang, S. Mao, H. Feick, H. Yan, Y. Wu, H. Kind, E. Weber, R. Russo, P. Yang, *Science* **2001**, *292*, 1897.
- [236] N. Zhou, Y. Bekenstein, C. N. Eisler, D. Zhang, A. M. Schwartzberg, P. Yang, A. P. Alivisatos, J. A. Lewis, *Sci. Adv.* **2019**, *5*, eaav8141.
- [237] K. Huang, Bo Wang, S. Guo, K. Li, *Angew. Chem., Int. Ed.* **2018**, *57*, 13892.
- [238] C. Ahn, J. Park, D. Cho, G. Hyun, Y. Ham, K. Kim, S.-H. Nam, G. Bae, K. Lee, Y.-S. Shim, J. N. S. Ang, S. Jeon, *Funct. Compos. Struct.* **2019**, *1*, 032002.
- [239] O. Dalstein, E. Gkaniatsou, C. Sicard, O. Sel, H. Perrot, C. Serre, C. Boissière, M. Faustini, *Angew. Chem., Int. Ed.* **2017**, *56*, 14011.
- [240] P. Falcaro, D. Buso, A. J. Hill, C. M. Doherty, *Adv. Mater.* **2012**, *24*, 3153.
- [241] K. Okada, R. Ricco, Y. Tokudome, M. J. Styles, A. J. Hill, M. Takahashi, P. Falcaro, *Adv. Funct. Mater.* **2014**, *24*, 1969.
- [242] G. Lu, O. K. Farha, W. Zhang, F. Huo, J. T. Hupp, *Adv. Mater.* **2012**, *24*, 3970.
- [243] A. Razmjou, M. Asadnia, O. Ghaebi, H.-C. Yang, M. Ebrahimi Warkiani, J. Hou, V. Chen, *ACS Appl. Mater. Interfaces* **2017**, *9*, 38076.
- [244] J. Del Barrio, C. Sánchez-Somolinos, *Adv. Opt. Mater.* **2019**, *7*, 1900598.
- [245] M. M. Waldrop, *Pet. Process.* **2016**, *530*, 144.
- [246] M. Totzeck, W. Ulrich, A. Göhnermeier, W. Kaiser, *Nat. Photonics* **2007**, *1*, 629.
- [247] Z. Nie, E. Kumacheva, *Nat. Mater.* **2008**, *7*, 277.
- [248] T. Ito, S. Okazaki, *Nature* **2000**, *406*, 1027.
- [249] R. Kumar, N. Singh, C. K. Chang, L. Dong, T. K. S. Wong, *J Vac Sci Technol B Microelectron Nanometer Struct Process Meas Phenom* **2004**, *22*, 1052.
- [250] J. W. P. Hsu, *Mater. Today* **2005**, *8*, 42.
- [251] J. D. Ryckman, Y. Jiao, S. M. Weiss, *Sci. Rep.* **2013**, *3*, 1502.
- [252] M. Tu, B. Xia, D. E. Kravchenko, M. L. Tietze, A. J. Cruz, I. Stassen, T. Hauffman, J. Teyssandier, S. De Feyter, Z. Wang, R. A. Fischer, B. Marmiroli, H. Amenitsch, A. Torvisco, M. De J. Velásquez-Hernández, P. Falcaro, R. Arneloot, *Nat. Mater.* **2021**, *20*, 93.
- [253] T. Toyao, K. Liang, K. Okada, R. Ricco, M. J. Styles, Y. Tokudome, Yu Horiechi, A. J. Hill, M. Takahashi, M. Matsuoka, P. Falcaro, *Inorg. Chem. Front.* **2015**, *2*, 434.
- [254] R. Bo, M. Taheri, H. Chen, J. Bradford, N. Motta, S. Surve, T. Tran-Phu, P. Garg, T. Tsuzuki, P. Falcaro, A. Tricoli, *Adv. Funct. Mater.* **2022**, *32*, 2100351.
- [255] A. B. Shrira, A. Hussain, C. H. Cho, R. Perez-Castillejos, *BioTechniques* **2012**, *53*, 315.
- [256] N. Yanai, T. Uemura, M. Inoue, R. Matsuda, T. Fukushima, M. Tsujimoto, S. Isoda, S. Kitagawa, *J. Am. Chem. Soc.* **2012**, *134*, 4501.
- [257] X.-J. Yu, Y.-M. Xian, C. Wang, H.-L. Mao, M. Kind, T. Abu-Husein, Z. Chen, S.-B. Zhu, B. Ren, A. Terfort, J.-L. Zhuang, *J. Am. Chem. Soc.* **2019**, *141*, 18984.
- [258] H. Hu, S. Wang, X. Feng, M. Pauly, G. Decher, Y. Long, *Chem. Soc. Rev.* **2020**, *49*, 509.
- [259] K. Ikigaki, K. Okada, M. Takahashi, *ACS Appl. Nano Mater.* **2021**, *4*, 3467.
- [260] O. Shekhah, K. Hirai, H. Wang, H. Uehara, M. Kondo, S. Diring, D. Zacher, R. A. Fischer, O. Sakata, S. Kitagawa, S. Furukawa, C. Wöll, *Dalton Trans.* **2011**, *40*, 4954.
- [261] J. Tao, M.-S. Lee, M. L. Sushko, J. J. De Yoreo, J. Liu, Z. Zhang, D. Banerjee, S. Akkineni, M. E. Bowden, P. K. Thallapally, Y. Shin, M. A. Sinnwell, *Chem. Mater.* **2020**, *32*, 6666.
- [262] Y. Luo, S. Bag, O. Zaremba, A. Cierpka, J. Andreo, S. Wuttke, P. Friederich, M. Tsotsalas, *Angew. Chem., Int. Ed.* **2022**, *61*, e202200242.
- [263] P. I. Scheurle, A. Mähringer, A. Biewald, A. Hartschuh, T. Bein, D. D. Medina, *Chem. Mater.* **2021**, *33*, 5896.
- [264] E. Virmani, J. M. Rotter, A. Mähringer, T. Von Zons, A. Godt, T. Bein, S. Wuttke, D. D. Medina, *J. Am. Chem. Soc.* **2018**, *140*, 4812.
- [265] P. D. C. Dietzel, Y. Morita, R. Blom, H. Fjellvåg, *Angew. Chem., Int. Ed.* **2005**, *44*, 6354.
- [266] T. Karmencik, B. Schröde, R. Resel, R. Ricco, E. Zojer, *Adv. Theory Simul.* **2022**, *5*, 2200031.
- [267] L. Shao, F. Meng, J. Chen, Y. Fu, *J. Mater. Chem. A* **2023**, *11*, 5027.
- [268] L. A. Brandner, M. Linares-Moreau, G. Zhou, H. Amenitsch, S. Dal Zilio, Z. Huang, C. Doonan, P. Falcaro, *Chem. Sci.* **2023**, *14*, 12056.
- [269] S. Ni, L. Isa, H. Wolf, *Soft Matter* **2018**, *14*, 2978.
- [270] M. Chang, Z. Su, E. Egap, *Macromolecules* **2016**, *49*, 9449.
- [271] A. Takemoto, T. Araki, Y. Noda, T. Uemura, S. Yoshimoto, R. Abbel, C. Rentrop, J. Van Den Brand, T. Sekitani, *Nanotechnology* **2019**, *30*, 37LT03.
- [272] X. Zhang, L. J. Richter, D. M. Delongchamp, R. J. Kline, M. R. Hammond, I. McCulloch, M. Heeney, R. S. Ashraf, J. N. Smith, T. D. Anthopoulos, B. Schroeder, Y. H. Geerts, D. A. Fischer, M. F. Toney, *J. Am. Chem. Soc.* **2011**, *133*, 15073.
- [273] J.-Oh Kim, W.-T. Koo, H. Kim, C. Park, T. Lee, C. A. Hutomo, S. Q. Choi, D. S. Kim, Il-D Kim, S. Park, *Nat. Commun.* **2021**, *12*, 4294.
- [274] T. Lee, J.-Oh Kim, C. Park, H. Kim, M. Kim, H. Park, I. Kim, J. Ko, K. Pak, S. Q. Choi, Il-D Kim, S. Park, *Adv. Mater.* **2022**, *34*, 2107696.
- [275] A. Ghorbanpour, L. D. Huelsenbeck, D.-M. Smilgies, G. Giri, *CrysEngComm* **2018**, *20*, 294.
- [276] N. Liu, Q. Sun, Z. Yang, L. Shan, Z. Wang, H. Li, *Adv. Sci.* **2023**, *10*, 2207210.
- [277] S. Liu, J. B.-H. Tok, J. Locklin, Z. Bao, *Small* **2006**, *2*, 1448.
- [278] Q. Zhang, S. Gupta, T. Emrick, T. P. Russell, *J. Am. Chem. Soc.* **2006**, *128*, 3898.
- [279] G.-W. Hsieh, J. Wang, K. Ogata, J. Robertson, S. Hofmann, W. I. Milne, *J. Phys. Chem. C* **2012**, *116*, 7118.
- [280] J. Dong, N. Mohieddin Abukhdair, I. A. Goldthorpe, *Nanotechnology* **2015**, *26*, 485302.
- [281] J. W. Durham, Y. Zhu, *ACS Appl. Mater. Interfaces* **2013**, *5*, 256.
- [282] M. Liu, P. J. Weston, R. H. Hurt, *Nat. Commun.* **2021**, *12*, 507.
- [283] T. P. Vinod, J. M. Taylor, A. Konda, S. A. Morin, *Small* **2017**, *13*, 1603350.
- [284] X. Zhang, J. Jie, W. Deng, Q. Shang, J. Wang, H. Wang, X. Chen, X. Zhang, *Adv. Mater.* **2016**, *28*, 2475.
- [285] S. Wu, Y. Shang, A. Cao, *Nano Res.* **2020**, *13*, 1191.
- [286] D. Yang, D. Kim, S. H. Ko, A. P. Pisano, Z. Li, I. Park, *Adv. Mater.* **2015**, *27*, 1207.

- [287] S. Guthrie, L. Huelsenbeck, A. Salahi, W. Varhue, N. Smith, X. Yu, L U. Yoon, J J. Choi, N. Swami, G. Giri, *Nanoscale Adv.* **2019**, *1*, 2946.
- [288] O. Kwon, M. Kim, E. Choi, J. H. Bae, S. Yoo, J. C. Won, Y Ho Kim, Ju Ho Shin, J. S. Lee, D. W. Kim, *Sci. Adv.* **2022**, *8*, eabl6841.
- [289] W.-H. Li, K. Ding, H.-R. Tian, M.-S. Yao, B. Nath, W.-H. Deng, Y. Wang, G. Xu, *Adv. Funct. Mater.* **2017**, *27*, 1702067.
- [290] Y. Lv, Z. Xiong, H. Dong, C. Wei, Y. Yang, A. Ren, Z. Yao, Y. Li, S. Xiang, Z. Zhang, Y. S. Zhao, *Nano Lett.* **2020**, *20*, 2020.
- [291] N-D H. Gamage, K A. McDonald, A J. Matzger, *Angew. Chem., Int. Ed.* **2016**, *55*, 12099.
- [292] J G. Nguyen, S M. Cohen, *J. Am. Chem. Soc.* **2010**, *132*, 4560.
- [293] I. Abánades Lázaro, S. Haddad, S. Sacca, C. Orellana-Tavra, D. Fairén-Jiménez, R. S. Forgan, *Chem* **2017**, *2*, 561.
- [294] D. Bradshaw, A. Garai, J. Huo, *Chem. Soc. Rev.* **2012**, *41*, 2344.
- [295] G. Mínguez Espallargas, E. Coronado, *Chem. Soc. Rev.* **2018**, *47*, 533.
- [296] S. Schmitt, M. Silvestre, M. Tsotsalas, A.-L. Winkler, A. Shahnas, S. Grosjean, F. Laye, H. Gliemann, J. Lahann, S. Bräse, M. Franzreb, C. Wöll, *ACS Nano* **2015**, *9*, 4219.
- [297] G A. Leith, C R. Martin, J M. Mayers, P. Kittikhunnatharn, R W. Larsen, N B. Shustova, *Chem. Soc. Rev.* **2021**, *50*, 4382.
- [298] C. Schneider, D. Ukaj, R. Koerver, A. A Talin, G. Kieslich, S P. Pujari, H. Zuilhof, J. Janek, M D. Allendorf, R A. Fischer, *Chem. Sci.* **2018**, *9*, 7405.
- [299] B V. Harbuzaru, A. Corma, F. Rey, P. Atienzar, J L. Jordá, H. García, D. Ananias, L D. Carlos, J. Rocha, *Angew. Chem., Int. Ed.* **2008**, *47*, 1080.
- [300] C M. Doherty, E. Knystautas, D. Buso, L. Villanova, K. Konstas, A J. Hill, M. Takahashi, P. Falcaro, *J. Mater. Chem.* **2012**, *22*, 11470.
- [301] J. Donohue, S E. Zeltmann, K C. Bustillo, B. Savitzky, M. A. Jones, G F. Meyers, C. Ophus, A M. Minor, *iScience* **2022**, *25*, 103882.
- [302] B. Kuei, M P. Aplan, J H. Litofsky, E D. Gomez, *Mater Sci Eng R Rep* **2020**, *139*, 100516.



Mercedes Linares-Moreau obtained her Ph.D. in Physics from the National University of San Martín (Argentina) in 2018. During her Ph.D. she studied electrical transport in mesoporous oxides and metal-oxide nanocomposites, and specialized in Scanning Probe Microscopies. In 2018 she joined the Falcaro group in TU Graz as a postdoc, as part of the ERC “POPCRYSTAL” project from 2018 to 2021. Since 2021 she is senior scientist at the Institute of Physical and Theoretical Chemistry (TU Graz). Her research focuses on heteroepitaxial growth of oriented MOF films and patterns, and in-situ characterization of MOFs and MOF-biocomposites.



Lea A. Brandner received her M. Sc. in chemistry from the Graz University of Technology (TU Graz) in 2019, for which she investigated bio-inorganic model systems of enzymes at the University of New Mexico, USA, under the Austrian Marshall Plan Scholarship Program. Later that year, she joined the Falcaro group at TU Graz for her Ph. D. studies. Her research focuses on the conversion of ceramics to MOFs, post-synthetic modification of MOF thin films, as well as microfabrication of MOFs and MOF derivatives.



Miriam de J. Velásquez-Hernández received her Ph.D. degree from the Universidad Nacional Autónoma de México (UNAM), where she explored the synthesis of hydrogen-bonded organic frameworks (HOFs) using organo-bis(silanetriols) as molecular building blocks. Then, she joined the Falcaro group at Graz University of Technology (TU Graz, Austria) as a CONACyT postdoctoral fellow. Currently, she works as a university assistant at TU Graz, where her research endeavours involve the fabrication of oriented MOF films and patterns, as well as the synthesis of MOF-based biocomposites for drug delivery applications.



Javier Fonseca received his PhD degree in Chemical Engineering from Northeastern University (Boston, USA) in 2020 under the supervision of Prof. Sunho Choi. In 2022, he became a postdoctoral researcher at the University of Vienna in Prof. Chin's group and is currently working as a postdoctoral researcher in Prof. Maspoch's group at the Catalan Institute of Nanoscience and Nanotechnology (Barcelona, Spain). His research focuses on the design and preparation of MOF-based superstructures and MOF composites.



Youven Benseghir obtained his MSc degree from University Paris-Saclay, France in 2018. He then moved to LCPB – Collège de France and Institut Lavoisier de Versailles where he obtained his PhD in Chemistry under the supervision of Dr. Mellot-Draznieks and Prof. Mialane. He joined Prof. Chin group at University of Vienna as a postdoctoral researcher in 2023 where he is working on MOFs alignment and assemblies for energy applications.



Jia Min Chin obtained her Ph.D. in 2010 under the supervision of Professor Richard Schrock at MIT (U.S.A.). Subsequently, she headed the Laboratory of Advanced Porous Materials at IMRE (Singapore), and was the 2013 L'Oréal Singapore For Women in Science National Fellow. She joined the University of Vienna in 2019, where she is now an Associate Professor. She was awarded an ERC Consolidator Grant in 2020 to research E-field manipulation of MOF materials. She is especially interested in exploiting fluid-fluid or fluid-solid interfaces and physicochemical interactions for multi-length scale materials structuring to generate structures with emergent properties.



Daniel Maspoch is an ICREA Research Professor at the Institut Català de Nanociència i Nanotecnologia (ICN2). He received his B.S. degree at the Universitat de Girona and his PhD degree at the Universitat Autònoma de Barcelona & Institut de Ciència de Materials de Barcelona. He worked as a postdoctoral fellow at Northwestern University. His research interests include reticular materials (MOFs, COFs and MOPs) and delivery systems.



Christian Doonan is a Professor of Chemistry and South Australian Government Future Industry Making Fellow at the University of Adelaide. His research is focused on the development of porous materials for applications in biotechnology and sustainable chemistry.



Paolo Falcaro is a Professor in Bio-based Materials Technology at the Institute of Physical and Theoretical Chemistry at Graz University of Technology (Austria). He worked as a postdoctoral fellow and team leader at CSIRO (Australia). His research specializes in the study of porous materials and related composites. His primary interests lie in advancing porous materials for device fabrication and biotechnology.